Electrochemically-Mediated Membrane Separations for Carbon Dioxide Capture

By

Kristin Jenise Vicari

B.S. Chemical Engineering
Northwestern University, 2008

M.S. Chemical Engineering Practice
Massachusetts Institute of Technology, 2009

Submitted to the Department of Chemical Engineering
in Partial Fulfillment of the Requirements for the Degree of

Doctor of Philosophy

at the

MASSACHUSETTS INSTITUTE OF TECHNOLOGY

June 2016

Signature of Author.. Signature redacted
Department of Chemical Engineering
May 20, 2016

Certified by............................ Signature redacted
T. Alan Hatton
Ralph Landau Professor of Chemical Engineering
Thesis Supervisor

Accepted by...................................... Signature redacted
Richard D. Braatz
Edward R. Gilliland Professor of Chemical Engineering
Chairman, Committee for Graduate Students

Electrochemically-mediated membrane separations for carbon dioxide capture

By

Kristin Jenise Vicari

Submitted to the Department of Chemical Engineering
on May 20, 2016, in Partial Fulfillment of the
Requirements for the Degree of Doctor of Philosophy
in Chemical Engineering

ABSTRACT

This thesis describes and analyzes several new designs for carbon dioxide (CO_2) separations using quinones in electrochemical cells. The intended application is carbon capture and sequestration. A quinone-ferrocene electrolyte is proposed as a novel chemistry for electrochemical carbon capture. Quantitative analyses are presented for two designs, and experimental results are provided for the quinone-ferrocene system in two configurations.

The first design uses quinones for facilitated transport of CO_2 across a planar, supported liquid membrane. A mixture of quinone and dianion adduct is sandwiched between two porous electrodes. An analytical solution for the current-potential equation is derived and then used to quantify the expected performance of the system in terms of capacity and energy efficiency.

In the second design, the electrolyte flows between the two planar electrodes of the electrochemical cell. Quinone reacts at the porous cathode to absorb CO_2 from the gas phase. The dianion adduct reacts at the nonporous anode to desorb the CO_2, which produces supersaturated regions in the cell. The CO_2 evaporates and the electrolyte is recycled. A numerical model has been developed to solve for the spatial values of species concentrations, current, and ionic potential in the flowing electrolyte. A design analysis of this system highlights the quantitative impact of certain operating parameters and supports recommendations for future development.

The first demonstration of an electrolyte that uses a quinone-ferrocene redox couple for carbon capture in a flow cell is presented. The quinone and ferrocene chemistries are introduced, and experimental results highlight the ability to couple quinone reduction to ferrocene oxidation and ferrocenium reduction to dianion-adduct oxidation using graphite electrodes.

A bench-scale test cell has been designed and built to demonstrate electrochemical carbon capture in a cell with laminar flow of the electrolyte. The quinone-ferrocene couple is implemented in this flow design. Experimental results show the ability to continuously capture CO_2 from a gas stream (15% CO_2, 85% nitrogen (N_2)) using the quinone-ferrocene couple in this design. Finally, experimental results highlight the cycling of electrochemical absorption and desorption of carbon dioxide using the quinone-ferrocene chemistry in flow-through electrodes.

Thesis Supervisor: T. Alan Hatton
Title: Ralph Landau Professor of Chemical Engineering

Dedication

To those who have led by example:

My mother, Dr. Vicari, for her drive, work ethic, and unlimited support,

My father, Dr. Vicari, for his brilliance and toughness,

And my grandfather, Dr. Vicari, for being the first one.

Acknowledgements

Advisor: I'd first like to acknowledge my advisor, **T. Alan Hatton**. We first met when I was a master's student in the practice school, and he has been a wonderful teacher and colleague ever since. He allowed me to do a mini-project in his lab when I was unsure about the commitment of graduate school. That experiment was, in part, what motivated me to get a PhD and to join his lab. He also has the ability to put together a wonderful and interesting research group. I give Alan credit for the positive relationships that developed between me and my lab mates over the years. I am also grateful that Alan loves to travel so much, because it meant that I was allowed to come along on occasion. We had interesting and inspiring trips to Germany and Saudi Arabia. Lastly, I must credit Alan with patience and creativity. This project was in no way easy or smooth in its progression. The vast majority of the experiments failed, and Alan was always helpful in listening and providing helpful suggestions. He has a design-focused mind, and he is in large part responsible for the breadth of designs explored in this work.

Committee: My thesis committee is one of the parts of my graduate experience for which I am most grateful. I often wished for more committee meetings, because I often experienced the highest density of learning (in terms of "amount learned per unit time") during my committee meetings. All three committee members have the uncommon ability to provide constructive feedback that is as encouraging as it is functional and useful.

I did not expect **Bill Green** to be as invested and participate as energetically as he did. My experience of him began with his teaching 10.34, and I was pleasantly surprised to learn of his deep knowledge of experimental equipment and techniques in his precise recommendations. **Howard Herzog** was a wonderful grounding force to the group and to the work. His experiences in the implementation of carbon capture technology, and his strong expertise in the field of CCS worldwide, were invaluable contributions to this project.

Martin Bazant, to me, was an instrumental committee member, colleague, teacher, and mentor. In his classes, I learned about transport and electrochemical theory. It is rare to meet someone who is as positive, encouraging, and helpful, as he is intelligent. His willingness to dive in to experimental and modeling details did not go unnoticed, and it helped me learn and get past the roadblocks I was facing. He also opened up his time, his group meetings, and his group, to my inclusion and participation. He is, to me, a model academic and a personal mentor.

Funding: This work and my education was supported initially by the Chemical Engineering Practice School Fellowship. The next two years were funded by ARPA-E, a division of the Department of Energy. The remainder of the project was funded by Saudi Aramco.

Technical Acknowledgements: Raymond Smith, **Sven Schlumpberger**, and **Kameron Conforti** also provided significant help in the modeling of the flowing electrolyte. All three provided helpful discussions and insight. Sven and Kameron also helped me do some modeling in COMSOL. **Ray** must be given special acknowledgement: he sat with me for three, long days, as we took some Python code that one of his labmates (Will Braff) built to do the numerical modeling in the flowing electrolyte, and we rewrote it so that it would simulate my research design. I do not know Python, so I provided the equations, and Ray had to do all the coding himself. I believe Ray is a special person for sharing the patience and generosity and positivity that he has. Working with Ray was some of the most enjoyable time of my graduate school career. He is funny and kind and smart. I also learned a lot about the physics of electrochemical systems by being able to observe and probe Ray's intuition and understanding of his field.

Mike Stern was one of the best parts of my graduate school experience. We shared many experiences for the first three years of my PhD and the last three years of his. I benefited immensely from his knowledge of the chemistry and electrochemistry of quinones. He helped me get started in the lab. He also became a wonderful and significant friend and colleague. We sat next to each other and talked every morning during our time together. He was also an exceptionally fun travel buddy, despite his heinous sense of direction. Finally, he designed and built the flow battery device that I repurposed for some experiments in this thesis.

Josh Dittrich is an exceptional mechanical engineer and designer, so it's a good thing that he runs a company, Start Something, to do those things. All of the experimental work required custom built parts for the devices themselves, as well as the supporting equipment. Josh also helped me design and built many other prototypes that didn't make it in to this thesis, but they literally fill a drawer. A select list of his contributions to this work includes: the Teflon part for the flow system, the customized compression fittings for the flow-battery, all of the customized Teflon stoppers in the glass vials, and a planar membrane cell whose data were presented at the ACS conference in 2013. In addition to his technical contributions, he was also a wonderful friend and supporter during this time. He is one of those people that everybody likes, and his moral support was as valuable to me as his technical support. I expect many big things from him in the future. Also, he is a skilled Jenga player.

I must mention **Keith Chadwick**, who was a postdoc in the Meyerson group. He helped me with the equipment and technique to measure the solubility of quinones in the solvents. In addition, **John Draper** is the technical rep for Bruker (now a part of Agilent), and he was instrumental in helping me run and maintain the gas chromatograph used for my research and Mike Stern's research.

Burcu Gurkan, **Paul Brown**, and **Demetra Achiellos** were wonderful lab mates and collaborators for various parts of this project. Burcu, Demetra, and I became friends as well as colleagues. I enjoyed spending time learning from you all and having fun as well. Burcu and Paul contributed heavily to the inclusion of ionic liquids in this project.

Sahag Voskian is a newer addition to the Hatton group, but a very helpful collaborator. He has a wonderfully strange sense of humor, and he helped significantly with the experimental results that were presented in this thesis. He set up and calibrated the rotameter and CO_2 analyzer, and provided moral and technical support during that experimental work. I wish him well as he continues with this work.

Sarah Luppino and **Jose M Cordero Hernandez** in the MIT Chemistry Department provided valuable insights in the project of deprotonating hydroquinones with bases. They are both talented chemists who were generous enough to help a stranger (we were introduced by a mutual friend).

David Taylor, **Maha Haji**, and **Douglas Jonart**, of the Precision Engineering Research Group at MIT contributed most of the machining and engineering work that I needed to take an old, broken glove box and make it work again. I learned a lot about mechanical design and sealing systems from all three. David probably contributed the most time and effort in to the final design and water-jetting of the plastic cover and the rubber gasket. I am also grateful that they became wonderful and positive friends while doing me this immense favor.

Special colleagues: It cannot be understated how supportive and capable the administrative staff in the MIT Chemical Engineering Department are. In particular, **Beth Tuths**, the admin for the Hatton group, was a pillar of support of me and my graduate work. She always went above and beyond the requirements of her job to be a source of friendship, support, and sunlight. She also kept my sad cactus alive for the duration of my PhD. I always looked forward to interacting with **Joel Dashnaw,** and later **Sydney Greenley-Kois**, in the student office. Their enthusiasm for the department and their work was enjoyable and infectious. **Suzanne Easterly** is the Academic Administrator to end all admins. There is no one more capable and knowledgeable and warm than she is. I have been blessed to intact with her over the last six years, in situations ranging from a thesis defense to a TA assignment to the annual baking contest. She is a really special woman, and she has the ability to keep the department running while having a unique relationship with each person in it.

I was also blessed to get to know **Barbara Balkwill** and **Gwen Wilcox** because they are the admins for the Bazant and Green groups, respectively. They had the unenviable task of interacting me when I was most stressed. Their ability to be helpful and flexible while also providing a calming environment was very valuable to me.

Friends: It is difficult to put on paper how grateful I am for the new and existing friendships that buoyed me during my tenure in graduate school. The friendships I made here are every bit as valuable as the technical knowledge I gained. **Jen Lee** and **Maria Jose Nieves Remacha** became wonderful friends in good and bad times. **Kevin Fowler**, **Andy Silverman**, **Vivian Hsieh**, **Christy Petruczok**, **Rachel Howden**, and **Mike Stern** represent a wonderful subset of MIT Chemical Engineering alumni. Our most frequenty activity was watching trashy reality tv and laughing very hard. **Jie Chen**, **Su Kyung Su**, **Dan Pregibon**, and **Tim Erps**: you guys are responsible for the times I've laughed the hardest in my life and some of the best adventures. I believe you are all crazy and brilliant in the best possible way.

Douglas Jonart has been an exceptional engineer, friend, and hockey buddy since the day I met him. He seems to have an encyclopedic knowledge of everything he has ever encountered, and he is a very clear speaker and thinker. I enjoyed his friendship and companionship on the ice, during our nature walks, and while we each wrote our PhD thesis. Also, I must acknowledge his dog, Reese, for being my therapy dog when I needed her. He is the epitome of a swim buddy.

The MIT Women's Volleyball club is one of the things I will miss the most. I've enjoyed getting to know my teammates while playing volleyball at an exceptionally high level for the past five years. I must acknowledge specifically **Darcy Duke**, **Darcy Grinolds**, **Petra Lindovska**, **Becky Leifer**, and **Kayla Ngan**. I also consider myself and my teammates incredibly spoiled for having the coaches we have: **Tony Lee**, **Randi Li**, **Max Wolf**, and **Eesh Bhatt**. My coach, Tony, has become a particularly special person to me. I am not sure how to label it, but I believe he is at the intersection of friend, coach, mentor, and inspiration.

I'd also like to acknowledge my friend, **Darcy Grinolds**. I didn't know a person like her existed until I met her. She is exceptional along so many axes. I must also credit **Danielle North** with the uncanny ability to make me laugh literally every time we talk. She and **Mallory Wendt** were wonderfully supportive and the best parts of "home" that stayed with me throughout this experience.

I first met **Bob Fisher** when he was my Station Director in the Practice School. Since then, he has been a huge contributor to my learning and growth as a researcher, engineer, and academic. In the process, I have come to know him as a talented engineer, teacher, and mentor. I believe he is the kind of mentor that people tell you to seek out in self-help books, and I have been lucky to have him in my corner for years. I am so grateful.

My family: My family's belief in me was what kept me going through the years of experimental failure that led to this thesis. I believe that if there were a limit to the support you could get from your family, I would have founded it over these last few years. Therefore, I believe I have shown experimentally, that there is no limit to their love, support, encouragement, and strength. My parents are my inspiration – I don't know any other people with the combination of toughness, talent, and generosity that they have. I'm also lucky to have siblings like Kaitlin and Frankie, who are also my oldest and dearest friends. It has been wonderful to watch them grow and succeed in their fields as the three of us pursue such different things. I consider myself supremely blessed.

List of Figures

1 Introduction

1.1 Motivation for carbon capture

The study of climate change is a complex and global field. [1, 2] Research indicates that global surface temperatures continue to increase over time [1] and variation in radiative fluxes at the Earth's surface drive many ambient climate processes, such as global warming. [2] At the same time, there is net generation of carbon dioxide (CO_2) and other greenhouse gases on a global scale. [3, 4, 5] Burning fossil fuels generates CO_2 at a rate that is one to two orders of magnitude higher than other large scale sources of CO_2. [6, 7] The next largest emitters are cement production, refineries, and the iron and steel industries. [6] To reduce large-scale CO_2 emissions, there are significant efforts to shift the energy landscape toward low-carbon and zero-carbon sources. Still, as of 2013, 18% of the primary energy consumption in the United States comes from coal combustion, 36% from petroleum and other liquids, and 27% from natural gas. [8, 7, 9] Projections indicate these fossil fuel sources will continue to dominate the US energy supply for the next ten to twenty years. [8] Therefore, there is motivation to capture CO_2 for storage and/or conversion. Capturing the CO_2 from these large, stationary sources could help to stabilize emissions levels in the near term while energy supply and demand shift more slowly. Carbon capture and sequestration (CCS) at large point sources requires that the capture technology be energy efficient at scale because the energy source will likely be a fossil fuel in the near term. On-board capture for vehicles also requires energy efficient CCS technologies that are optimized for the added constraints of transportation.

Capturing CO_2 from coal combustion can occur either pre-combustion or post-combustion. The condition of the flue gas stream depends on the power source. In a typical post-combustion capture, the flue gas pressure is typically one atmosphere and its temperature is 35-75°C. [10] The partial pressure of CO_2 in this stream is 5-20 vol%, depending on process conditions. [10] In the case of oxy-fired combustion, the coal is burned in the presence of a concentrated oxygen stream instead of air. Most of the nitrogen is separated before combustion, so the outlet gas has a CO_2 concentration of 90 vol% after dehumidification. [11] Pre-combustion capture is carbon capture that occurs upstream of hydrogen combustion and downstream of coal gasification. [12] Gasification produces synthesis gas ("syngas"), which is a mixture of carbon monoxide (CO) and hydrogen gas (H_2), with some water and CO_2. [13] The gas is then "shifted" to produce a mixture of hydrogen and carbon dioxide. [13] As a result, the inlet stream to the carbon capture technology has a relatively high CO_2 partial pressure. For carbon capture, a higher CO_2 concentration implies a lower volume of gas to be treated and a lower thermodynamic energy requirement.

Post-combustion capture is advantageous because retrofit is generally possible without excessive changes to the existing energy source. In the process of carbon capture and sequestration, the separation stage is energy intensive and is the largest cost driver of the CCS process. [14, 15] Thus, there is motivation to search for more effective separation technologies.

1.2 Existing sorbent technologies

The state-of-the-art in carbon capture is a cyclic process of absorption and desorption. The flue gas is contacted with a sorbent that selectively binds CO_2. Once the sorbent is saturated, the process conditions are changed so that the sorbent releases the CO_2 and is regenerated for the next cycle. A schematic of this process is shown in Figure 1.1. The particulars of the process depend on the nature of the sorbent and the parameter that determines its affinity for CO_2. Sorbents in liquid form may bind CO_2 in a chemical reaction or physically dissolve it. Solid sorbents capture CO_2 when it physically or chemically adsorbs to the surface. [12] In most cases, either the temperature or the pressure determines the CO_2 affinity.

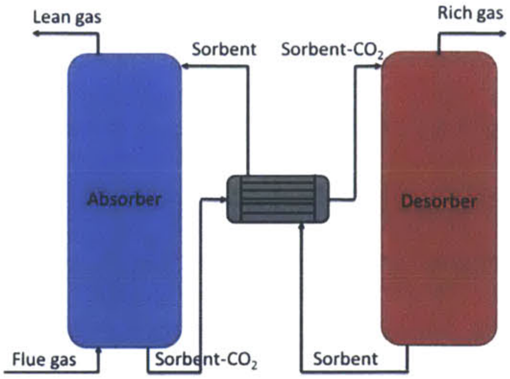

Figure 1.1 Schematic of a typical absorption-desorption cycle.

The benchmark technology for carbon capture is thermal-swing chemical absorption using aqueous amines or carbonates. [16, 12, 17] Aqueous monoethanolamine (MEA), first patented in 1930 [18], absorbs

CO_2 at approximately room temperature. The amine is regenerated by stripping with water vapor at 100-120°C. [16] A reversible chemical reaction between two moles of MEA and one mole of CO_2 favors the formation of a carbamate at low temperatures. [19] At high temperatures the carbamate dissociates to regenerate the MEA and desorb the CO_2. The capacity of the solution is determined by stoichiometry and the solubilities of the amine and the carbamate.

Several review papers articulate the key advantages and disadvantages of aqueous amine systems, and thermal, chemical absorbers in general. [12, 20, 21] Aqueous amines tend to have a high absorption efficiency and are favorable when the feed gas has a low CO_2 partial pressure. Plus, aqueous amines can release CO_2 under conditions that produce a gas with a relatively high CO_2 purity. Amine technology is also the most mature process for CO_2 separations. The sorbent capacity is a strong function of stoichiometry and solubility, and it is relatively insensitive to CO_2 partial pressure. However, MEA has a high heat of reaction (absorption), which means significant energy is required to regenerate it. [12, 20] In addition, the reaction stoichiometry and the corrosive nature of the solution limit its volumetric capacity for CO_2. Large amounts of water must be continuously heated and cooled, which is a significant parasitic energy loss. Amine scrubbers require low pressure steam for regeneration. Thus, the retrofit of an energy source must include reconfiguration of the utilities network.

Significant research in the field of amine scrubbers focuses on the chemistry of the amine itself. Other variations on amine processes involve process intensification [22]. Recent work in our lab has demonstrated a novel way to regenerate the sorbent by displacing the carbon dioxide with metal anions and then recovering the anions via electrochemical plating. [23, 24] Others are working to combine the advantages of amines and ionic liquids (ILs). [25] This continues to be a fertile area of research.

Proposed alternatives to aqueous amines include physical solvents, ionic liquids, and solid sorbents. Some inert liquid solvents preferentially absorb CO_2 from a mixture, and can be regenerated at elevated temperature or decreased pressure. Physical solvents are advantageous because the heat of absorption is lower than that of reactive absorption. [12] However, physical absorption is less effective when CO_2 must be captured at low partial pressures. The solvents must have low volatility to avoid contaminating the lean and rich gases with solvent vapor, and solvent recovery and recycle is costly. An interesting alternative is the use of room temperature ionic liquids (RTILs) as physical solvents for CO_2. [26] RTILs are advantageous because they are considered nonvolatile. Their key limitations are high viscosities and correspondingly low mass transfer rates. They may be physical sorbents or they may be functionalized with amine groups so that they operate via reactive absorption. [26, 25] Adsorbent materials are attractive options for avoiding the sensible heat sink of the aqueous solvent. [27] For example, calcium oxide (CaO) sorbents synthesized from limestone are microporous solids. Gaseous CO_2 reacts with the solid metal oxide to produce calcium carbonate, which can be thermally regenerated to the metal oxide. [28] In general, CO_2 capture and release using metal oxides requires much higher temperatures than the liquid-phase alternatives. Researchers in these fields continue to focus on optimizing the energy profiles and mass transfer properties of absorption and regeneration.

1.3 Electrochemical separations

Electrochemically-mediated separations are those in which the chemical separation is driven directly by electricity. For carbon capture, the systems may involve Faradaic reactions of CO_2 directly. Others employ a sorbent whose CO_2 binding affinity is controlled electrochemically. As isothermal systems, they do not require a heat cycle, so they are not limited by the Carnot efficiency. By being electrically-driven, these systems are essentially agnostic to the energy source; there is no need to reconfigure the utilities network of a power plant to provide heat or steam for CO_2 separation. In addition, a one-step, fuel cell- or membrane-type configuration would eliminate the need to circulate large volumes of liquid from an absorber to a desorber. In the efforts to retrofit existing coal-fired power plants with CCS technology, these can be significant advantages.

Carbonate pumps are a dominant technology in the field of electrochemical carbon capture. Molten carbonate fuel cells can function as CO_2 concentrators. [29, 30, 31, 32, 33] A galvanic molten carbonate fuel cell produces energy by oxidizing hydrogen fuel to produce water. The charge carrier is the carbonate ion (CO_3^{2-}) and the electrodes are separated by a molten electrolyte membrane. That electrochemical cell can capture CO_2 by feeding flue gas (N_2, CO_2, O_2, etc.) in at the anode and applying a potential. Under those conditions, the cell will selectively transport CO_2 and oxygen (O_2) as carbonate and bicarbonate ions. [29, 31, 32, 33] These "carbonate pumps" offer the advantages of energy efficient, coupled absorption-desorption. The electrolyte has a negligible vapor pressure and non-noble metal electrodes are functional at the high temperatures of the molten electrolyte. [29, 33] The main drawback is that the product is at best a mixture of CO_2 and O_2 in a 2:1 ratio. This also implies that when the feed ratio of O_2 to CO_2 is less than ½, the amount of O_2 will limit the amount of CO_2 that can be captured. More generally, carbonate has been studied frequently as a carbon capture vehicle.

Other electrochemical cells do not directly reduce nor oxidize carbon dioxide. Instead, the oxidation state of a sorbent is mediated electrochemically, and the sorbent binds CO_2 through a chemical reaction. For example, one can concentrate CO_2 by electrochemically producing hydroxide, which reacts with carbon dioxide to form bicarbonate ions. Landon and Kitchin capture carbon from a mixture containing oxygen by using electrocatalysts to combine oxygen and water to form hydroxide and using an anion exchange membrane as a separator. [34] The bicarbonate ions traverse the anion exchange membrane and are oxidized at the other electrode to desorb CO_2. They report a cell potential lower than the potential at which water splits, but the technology is limited because it necessarily captures carbon dioxide and oxygen together. Moreover, the reaction kinetics for capture via bicarbonate are slower than the kinetics via ethanolamines. [35]

In electrochemically-facilitated transport, the gradients are controlled via an external, electric circuit. Central to this concept is a "carrier" molecule that transports the desired solute. The carrier is a redox-active molecule whose affinity for CO_2 is dependent on its oxidation state. Ward et. al. developed electrochemically-mediated facilitated transport as a natural extension of previous work in (chemically) facilitated transport membranes. [36, 37, 38] Specifically, electrochemical control of the ferrous (Fe^{2+}) and ferric (Fe^{3+}) ion concentrations at two electrodes separated by a liquid membrane can drive the facilitated transport of nitric oxide (NO). [37] In fact, it is possible to transport NO in a desired direction irrespective of the presence and direction of an overall NO concentration gradient. [37, 38]

Subsequent work in electrochemically-mediated membrane separations (ECMS) processes for CO_2 capture has focused on development of the redox-active carrier molecule. The carrier must have a significant difference in *reversible* binding affinity for CO_2 in different oxidation states. The carrier must be chemically stable in both redox states, and the carrier-CO_2 complex must also be stable. The electric potentials of the redox states define a potential window. If the carrier requires electric potentials that are too positive or negative, then the system will be susceptible to parasitic side reactions that involve the solvent and other species in the gas phase (O_2, H_2O, etc.). For use in liquid systems, the carrier must have a negligible vapor pressure to avoid evaporative losses.

Organic and inorganic carriers have been studied for applications in electrochemically-mediated separation of CO_2 from a mixture. Dubois et al. first determined selection criteria after presenting electrochemical studies of carrier molecules. [39] The results indicate three criteria for the carriers: a CO_2 binding center, an ability to participate in reversible, Faradaic reactions, and electric proximity of those two functionalities. [39] One class of molecules, called quinones, satisfies these criteria. [39] Separately, inorganic, transition-metal complexes have been explored as water-soluble, air-stable carriers of the bicarbonate anion. [40, 41] Their application to carbon capture has been limited by their chemical instability. [40, 41, 42] Nickel complexes require negative potentials that would encourage competing reactions or solvent decomposition. [40] Copper (Cu) complexes can be oxidized and reduced at more reasonable potentials, but the Cu(I) product may disproportionate to Cu(0) or precipitate as a Cu(I) salt. [41] Moreover, both systems require two electrons per CO_2 captured. Since power is directly proportional to current, minimizing the ratio of current to CO_2 flux is important. To summarize, carbonate, bicarbonate, transition metal ions, and quinones make up the bulk of previously-researched electrochemical CO_2 carriers.

1.4 Carbon capture using quinones

A quinone molecule has a cyclic, fully-conjugated di-ketone structure. [43] It has two binding centers, the ketone oxygens, and is electrochemically-active via the aromatic ring. Quinones are ubiquitous in the field of electrochemistry, and they are known for the ability to undergo reversible electron transfer reactions. [44] They are also widely studied for their roles in electron transport for biological processes. [45] Literature since 1989 has provided evidence for *reversible*, reductive addition of CO_2 to a quinone. [39, 42, 46] In addition, CO_2 can be captured at a rate of one electron per CO_2 molecule.

The suitability of quinones or similar moieties as CO_2 carriers depends on the presence and identity of functional groups, and the solvent. [47, 48] The overall chemistry of the quinone determines its "potential window" and its susceptibility to unfavorable side reactions. [39, 47] The kinetics and mechanisms have been studied in the literature. [49] Many previous researchers have studied the electrochemical and chemical behavior of quinones in the presence of carbon dioxide, and others have also addressed the solvent and pH conditions. [46, 49, 47] Stern investigated the ability to capture CO_2 in aqueous solutions of benzoquinone, naphthaquinone sulfonic acid, and anthraquinone di-sulfonic acid via formation of bicarbonate ions, but none of those moieties was stable to both pH and oxygen. [50] Scovazzo et al. demonstrated the ability to concentrate CO_2 200-fold using a two-step electrochemical process. [51] The quinone was reduced in the presence of a feed gas (0.5vol% CO_2). Then, the quinone was oxidized, and the released gas was collected and analyzed. The quinone used in this experiment was prone to react with oxygen, thereby reducing its efficiency as a sorbent. [51] Other researchers used the redox reactions of hydroquinone in aqueous media to capture carbon dioxide in a "fuel cell-like" configuration by creating a pH gradient across a supported liquid membrane. [35] They were able to demonstrate carbon capture, but this chemistry requires a metal catalyst on one electrode, and the kinetics of bicarbonate reactions are slower than CO_2 reactions with ethanolamines. [35]

Simeon performed a systematic and comprehensive study of the redox potentials of functionalized quinones in organic solvent and their interactions with carbon dioxide. Figure 1.2 is a summary of his unpublished results. He examined the electrochemical oxidation and reduction of more than 15 quinonoid species in the presence and absence of carbon dioxide. The results in Figure 1.2 show the half-wave potentials of the first and second electron transfers of the quinones under nitrogen (red data) or carbon dioxide (blue data). The filled circles are placed at the half-wave potentials for the Faradaic reduction reactions. For each quinone, the red circle furthest to the right shows the half-wave potential of the first electron transfer, which converts the quinone to a semiquinone (a radical anion). The second red circle at more negative potentials represents the half-wave potential of the second electron transfer, which converts the semiquinone to a dianion. The blue circles show the same data measured in the presence of carbon dioxide.

Simeon separated the quinones into categories of strongly or weakly complexing species according to their interactions with carbon dioxide. For strongly complexing quinones, he reports only one half-wave potential in the presence of CO_2. He asserts that these species are reduced to a semiquinone intermediate that interacts with CO_2 in such a way that the second electron transfer occurs at the same or nearly the same electric potential as the first electron transfer.

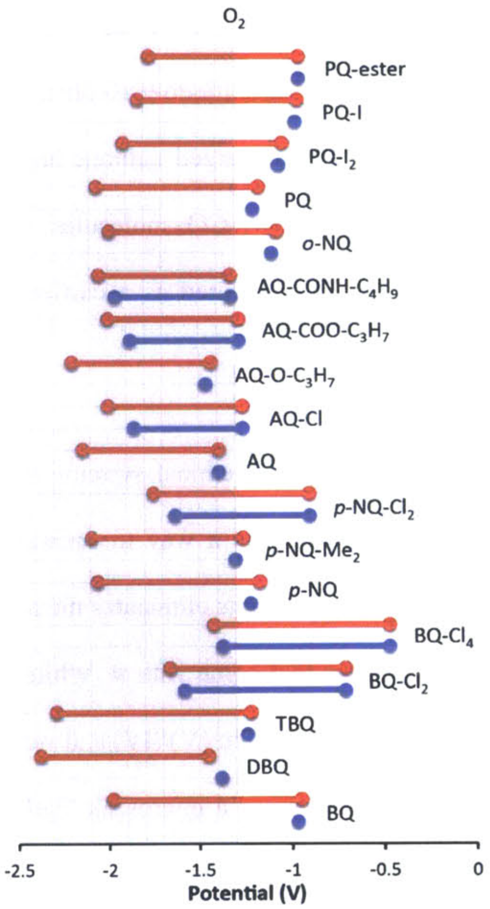

Figure 1.2 Tabulated cyclic voltammetric results for 20 mM of individual quinones in dry dimethylformamide with 0.1 M tetrabutylammonium hexafluorophosphate as supporting electrolyte. The potential is reported relative to a ferrocene internal reference. (Unpublished work by Dr. Fritz Simeon in the Hatton group at MIT).

Previous work highlighted that some quinones are susceptible to parasitic interactions with oxygen in both organic and aqueous media. [39, 51, 50] Specifically, it is believed that the redox reactions of those quinones occur at potentials more negative than the reduction potential of oxygen. Oxygen can be reduced to a superoxide radical, which is highly reactive. The results in Figure 1.2 highlight those quinones whose electrochemical reactions and binding of CO_2 occur at potentials more positive than the reduction potential of oxygen. In Figure 1.2, the reduction potential of oxygen is highlighted at -1.3 V (vs. ferrocene internal reference) by a dark grey box. Therefore, the following species are known to be strongly-complexing quinones that bind CO_2 at potentials more positive than oxygen reduction: p-benzoquinone (BQ), 2,7-di-

tert-butyl-p-benzoquinone (TBQ), p-napthoquinone (p-NQ), o-napthoquinone (o-NQ), phenanthraquinone (PQ), 2-iodo-9,10-phenanthraquinone (PQ-I), and 2,7-diiodo-9,10-phenanthraquinone (PQ-I_2).

With appropriate functional groups, the uncharged quinone has a negligible binding affinity for CO_2, while the reduced quinone dianion can bind two CO_2 molecules – one at each ketone oxygen. This electrochemically-controlled sorbent can be implemented as a carrier for electrochemically-facilitated transport of carbon dioxide.

1.5 Laminar flow electrochemical cells

Implementation of laminar flow in electrochemical systems can take different forms. Energy researchers are drawn to the use of laminar flow as a way to separate fuels and oxidants without a membrane. The use of laminar flow to separate reactants eliminates the need for a physical membrane and the ohmic losses and fouling and drying issues that come with it. Whitesides *et al.* used laminar flow in microchannels to couple the redox reactions of vanadium (V)/(IV) and vanadium (III)/(II) in a microfluidic system without a membrane. [52] Kenis *et al.* created a microscale fuel cell with catalytic layers on the sidewalls of the microchannel. In this fuel cell, dissolved oxygen at one electrode oxidizes the dissolved fuel at the other in an aqueous system. [53]

Laminar systems can be designed to incorporate a gas phase. Kenis *et al.* designed a fuel cell that uses molecular oxygen as an oxidant by integrating a gas diffusion electrode into a microfluidic laminar flow-based fuel cell. [54] Bazant et al. published in-depth analytical and numerical modeling with experimental results for a Hydrogen Bromine Laminar Flow Battery that uses hydrogen gas to reduce liquid bromine. [55, 56] The fuel utilization in early laminar flow cells was considered low, so subsequent work has focused on enhancing fuel utilization via flow-through porous electrodes and other cell architectures. [57]

Several recent publications have demonstrated implementation of quinones in flow batteries. Researchers at Harvard have couple a quinone/hydroquinone redox reaction with the bromine/bromide redox reaction in water in a configuration where the two reactant streams flow past planar but porous carbon electrodes separated by a Nafion membrane. [58] They report the advantages of using organic reactants, the opportunity for chemical optimization of the quinone, and the advantages of flow batteries over traditional designs, but they use a membrane in their design. [58] In a separate publication, researchers screened a series of quinones computationally to optimize their aqueous redox potentials for implementation in a flow battery. [59] Aside from the chemistry, a numerical model was developed to describe transport phenomena and highlight the dominant resistances in the cell design. [60] A subsequent publication built upon the initial results by showing the possibilities and advantages of changing the chemistry to a coupling of 2,6-dihydroxyanthraquinone (2,6-DHAQ) and the ferrocyanide/ferricyanide reaction in basic media. [61]

The literature on laminar flow systems and flow electrochemical systems focuses on applications in batteries and fuel cells, and focuses on microfluidic-scale systems. A search on laminar flow electrochemical cells revealed very few publications that did not focus on fuel cell applications and conditions (namely, galvanic operation). A review on membraneless laminar flow fuel cells focused on developments in microchannel design, including static mixers and "air-breathing" (porous, gas-phase) electrodes, and suggested applications as sensors and "Lab on Chip" devices. [62] Girault *et al.* demonstrates the use of laminar flow electrochemical cells to induce a Faradaic reaction driven by electrolytes of different concentrations. [63] Moon *et al.* tested the feasibility of using immobilized horseradish peroxidase (HRP) and electrochemically-generated hydrogen peroxide to catalyze the oxidation of phenol. [64] Yager *et al.* used controlled laminar flow of reactants in a microchannel to study the HRP enzyme and the electrochemical nature of its biocatalytic signal enhancement. [65]

1.6 Study objectives and organization

In this thesis, three new designs for electrochemically-mediated carbon capture using quinone sorbents are presented and analyzed. In addition, a quinone-ferrocene system is proposed as a novel redox couple for electrochemical carbon capture. Numerical simulations and analyses are presented for two designs that implement the coupled absorption and desorption of CO_2 via electrically-coupled oxidation and reduction of quinone. Experimental results are provided for the quinone-ferrocene system in two configurations.

Chapter 2 contains results for a system in which a redox coupling of a quinone and the corresponding dianion adduct drives facilitated transport of carbon dioxide across a planar, supported liquid membrane. The governing equations and boundary conditions are solved analytically to produce an expression for the current-potential (I-V) curve. This analytical solution is used to quantify the expected performance of the system in terms of capacity and energy efficiency. The chapter ends with a description of the advantages and significant design challenges for this configuration.

Chapter 3 begins with the introduction of a design for an electrochemical cell in which quinones flow between two planar electrodes. At the porous cathode, a Faradaic reaction produces a charged quinone that absorbs CO_2 from the adjacent gas phase. This quinone-CO_2 complex is referred to as the dianion adduct. This electrochemical reduction event is coupled to electrochemical oxidation of the dianion adduct at the anode. The oxidation reaction releases CO_2 and produces a region with high local CO_2 concentrations. The CO_2 desorbed at the anode is captured using two flash tanks in series, and the electrolyte is recycled to the cell entrance. The governing equations and boundary conditions for a numerical model of the electrochemical cell are described and justified. The numerical simulation solves for the spatial values of species concentrations, current, and ionic potential in the flowing electrolyte. The model is combined with equations describing the other unit operations to perform a design analysis of the complete system. The design analysis explores the operating landscape by varying certain parameters individually and measuring the impact on the overall performance of the system. The results of the design analysis are summarized and provide justification of the suggestions for future work.

In Chapter 4, the idea of coupling the reversible electrochemistry of the quinone-dianion to the reversible electrochemistry of the ferrocene-ferrocenium couple is introduced. A discussion of the background knowledge of the ferrocene-ferrocenium chemistry provides information to justify the selection of this moiety. Then, experimental evidence for coupling quinone reduction to ferrocene oxidation highlights the viability of using this chemistry in the designs proposed in earlier chapters. The experimental results also prove that the reactions proceed quickly using simple, graphite electrodes. The last set of experimental results in this chapter demonstrate that the electrochemical reactions can be reversed by reducing ferrocenium and oxidizing the dianion adduct with the same graphite electrodes. The experimental results also prove that the electrochemical reactions can be "cycled" several times without issues.

Chapter 5 begins with the proposal of a flow design for carbon capture using the quinone-ferrocene couple. The electrochemical cell has the same design as the quinone-dianion laminar flow system in Chapter 3, but the reaction at the anode is the electrochemical oxidation of ferrocene. The design and construction of a bench-scale test cell follows. The test cell includes "off-the-shelf" graphite gas diffusion electrodes with a custom-built Teflon channel for the laminar flow of the electrolyte between these electrodes. The latter half of the chapter includes results from experiments in which a mixture of phenanthrenequinone and ferrocene flow through the test cell and the quinone is reduced at the porous cathode to capture CO_2 from a mixture of 15% CO_2, 85% nitrogen (N_2). Key design challenges are highlighted and suggestions for future demonstrations are included.

Chapter 6 contains experimental results demonstrating the ability to cycle electrochemical absorption and desorption of carbon dioxide using a quinone sorbent in a system that employs porous, flow-through electrodes. These results demonstrate the concept of reversible absorption and desorption via the electrochemical coupling of quinone and ferrocene electron-transfer reactions.

Finally, the major conclusions from this work are summarized in Chapter 7. The latter half of the chapter is a discussion of opportunities for future work.

2 Electrochemically-facilitated transport of CO_2 across a planar, supported liquid membrane

2.1 Motivation and description of electrochemical cell design

The planar membrane cell is a separation system designed to unite the advantages of electrochemical energy conversion, membrane systems, and quinones as CO_2-selective, redox-active carriers. The cell employs a modular, "membrane sandwich structure". There are graphite "gas diffusion" electrodes to conduct electrons to porous, wetted electrodes. The descriptor "gas diffusion" means the graphite plates have flow channels that conduct the flow of gas in a region that is adjacent and parallel to thin, wetted, electrode "mats". A quinone solution wets the electrodes and makes up the supported liquid membrane. Cells may be run in parallel to scale the system, and/or in series to function as staged separations.

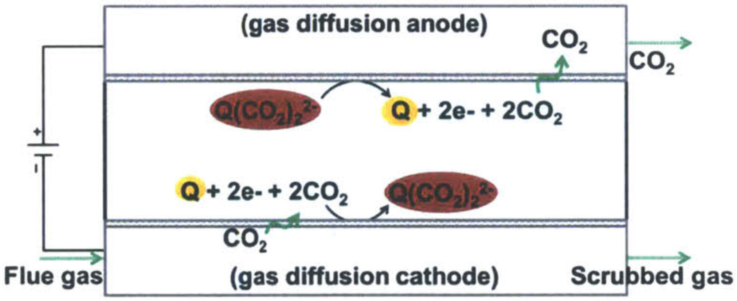

Figure 2.1 The conceptual design of a planar electrochemical cell for carbon capture.

Figure 2.1 has expanded dimensions to illustrate the paths of the quinone and CO_2. The actual supported liquid membrane, which is the light blue rectangle in the middle of Figure 2.1, should be as thin as possible. The CO_2 in the flue gas dissolves in to the solution that wets the cathode. This step is shown in the lower left corner of Figure 2.1. At the cathode, a quinone (orange) is electrically reduced and the resulting quinone dianion binds two molecules of CO_2. This quinone-CO_2 complex is called a dianion adduct, and highlighted in red in Figure 2.1. A thin polymer separator contains the electrolyte solution in its pores. The separator itself is an electric insulator. The dianion adduct moves from the negatively-charged cathode across the membrane to the positively-charged anode. At the gas diffusion anode, the quinone dianion is electrically oxidized and the CO_2 desorbs from its bound state. The relatively high concentration of CO_2 in solution drives it to vaporize in to the adjacent, CO_2-rich gas stream. This step is shown in the upper right corner of Figure 2.1. In response to an electric potential gradient, the electrons move through the external circuit from the anode to the cathode.

For the purpose of this work, the overall reaction scheme for electrochemically-mediated membrane separations (ECMS) is condensed to a set of two reactions. One is a Faradaic (electron-transfer) reaction with a standard potential of E^0. The other reaction is a homogeneous, chemical reaction with an equilibrium constant of K_B.

$$Q + 2e^- \overset{E^0}{\rightleftharpoons} Q^{2-} \tag{1}$$

$$Q^{2-} + 2CO_2 \overset{K_B}{\rightleftharpoons} Q(CO_2)_2^{2-} \tag{2}$$

The system is "electrochemically-mediated" because the electrical potential of the electrode relative to E^0 determines the equilibrium concentrations of quinone (Q) and dianion (Q^{2-}) adjacent to that electrode. The resultant concentrations of the quinone and dianion shifts the bulk reaction equilibrium and the concentrations of bound CO_2 (in the dianion adduct, $Q(CO_2)_2^{2-}$) and "free" CO_2.

The ECMS cell achieves separation through the enhanced transport of CO_2 across the membrane. A potential applied across the electrodes drives absorption and desorption of CO_2 at the cathode and anode, respectively. The spatial separation of sorbents with high affinity for CO_2 (at the cathode) and low affinity for CO_2 (at the anode) drives the directional transport of CO_2 across the membrane.

Other species in the flue gas can and will dissolve into the electrolyte and diffuse across the membrane. The permeability of the membrane to these species is governed by their diffusivities, solubilities, and partial pressures in the gas streams. However, the permeability of the membrane to CO_2 is dependent on the electric potential and the quinone concentration in addition to the CO_2 diffusivity, solubility, and concentration. For this reason, the membrane is selectively permeable to CO_2 and can be used to separate CO_2 from the flue gas.

2.2 An analytical model to describe current and potential through the cell

Preliminary analysis shows the potential for ECMS to be an energy-efficient and selective method for carbon capture. In this section, an analytical solution to the conservation equations for quinone and dianion in the cell is linked to the current and potential required to drive the cell and the rate of CO_2 capture that occurs. This analytical solution allows for the prediction of the performance and behavior of the system based on the design of the cell and the physical parameters of the electrolyte. These results are also valuable because they facilitate fast, easy parameter screening without experiments or the computational expense of a full numerical model.

2.2.1 Assumptions and governing equations for planar membrane cell

Analytical solution of the governing equations is possible for a system of this geometry under the following, assumed conditions:

- Mixtures behave as dilute, ideal solutions.
- The dimensions of the membrane and electrodes are such that the system is effectively one-dimensional.
- The electrodes are very thin, and the Faradaic reactions are heterogeneous. The electrodes are treated as vanishingly-thin planar reaction interfaces. The chemical reaction involving the dianion and CO_2 is also considered heterogeneous.
- The reactions are assumed fast, so that kinetic overpotentials are neglected and the electrochemical and chemical reactions equilibrate rapidly.
- At the boundaries, the dissolved CO_2 is assumed to equilibrate quickly with the CO_2 in the adjacent gas phase. CO_2 is treated as sparingly soluble, and its concentration follows Henry's law behavior.
- Physical properties of the electrolyte are constant.
- There is an excess of supporting electrolyte.
- Local electroneutrality is assumed; double layer effects are neglected.

The electrochemical power (P) required to capture carbon via ECMS is the product of the cell potential (V) and the current (I) through the cell. The derivation in this chapter produces analytical expressions for the current, the potential, and the rate of CO_2 capture.

$$P = \dot{W}_{EC} = I \cdot V \tag{3}$$

In the simplest case, there are six field variables: five concentrations (neutral quinone, dianion adduct, unbound carbon dioxide, and an inert cation and anion) and the electric potential in the electrolyte (a.k.a. the ionic potential). The two inert ions make up the supporting electrolyte. The term "supporting electrolyte" describes ions that do not participate in Faradaic reactions. The governing equation for each of the five species concentrations is the same for all five species. The vector N_k is the molar flux vector for species k. The governing equations are statements of mass conservation for a system at steady-state.

$$\nabla \cdot \vec{N}_k = 0 \tag{4}$$

In a system modeled as locally electroneutral, the expression for local electroneutrality replaces Poisson's equation as the sixth governing equation. The parameter z_k is the charge of species k.

$$\sum_k z_k C_k = 0 \tag{5}$$

To summarize, there are six unknowns: five concentrations and one potential. There are also six equations: five fluxes that are constant and the local electroneutrality equation.

2.2.2 Current, potential, migration, and supporting electrolyte

The current density (i) in an electrolyte is proportional to the sum of each ion's flux (N_k) and its charge (z_k). The Nernst-Planck equation (Equation(7)) defines the flux vector as the sum of convection, diffusion (in response to concentration gradients) and migration (in response to potential gradients) terms.

$$\vec{i} = F \sum_k z_k \vec{N}_k \tag{6}$$

$$\vec{N}_k = C_k \vec{v} - D_k \left[\vec{\nabla} C_k + z_k C_k \frac{F}{RT} \vec{\nabla} \phi \right] \tag{7}$$

The planar membrane cell consists of a supported liquid membrane whose fluid is stagnant, so there is no convective flux. The derivation presented in this section will show that for this particular system, the following conclusions and simplifications apply:

- Flux of dianion adduct due to migration is negligible.

- The current is carried by the flux of the charged electroactive species, which is only the dianion adduct.
- The gradient in electric potential across the electrolyte takes the form of an "Ohm's Law" relationship.

Mathematically, the physical impact of a high relative concentration of supporting electrolyte can be justified through a perturbation analysis. This analysis was first presented by Levich. [66] Chu presented a variation of this analysis in his doctoral thesis. [67] The derivation presented here is a variation of Chu's method of analysis but applied to this specific system.

There are three ions present in the cell: the dianion adduct ($Q(CO_2)_2^{2-}$), an inert cation, and an inert anion. In this case, the inert cation that balances the charge of the dianion adduct is the same as that which pairs with the inert anion. That condition is not mandatory, but convenient. The following notation is used from this point forward: the dianion adduct is labelled "Q2", the inert cation is labelled "p", and the inert anion is labelled "n". It is also convenient to switch to dimensionless variables, which are delineated with a tilde. The dimensionless ionic potential ($\tilde{\phi}$) is scaled to the thermal voltage, *RT/F*, and the dimensionless concentrations ($\tilde{C}_k$) are scaled to their average, bulk concentrations, $\overline{C}_k$.

$$\tilde{\phi} = \frac{F\phi}{RT} \qquad \tilde{C}_{Q2} = \frac{C_{Q2}}{\overline{C}_{Q2}} \qquad \tilde{C}_p = \frac{C_p}{\overline{C}_p} \qquad \tilde{C}_n = \frac{C_n}{\overline{C}_n} \tag{8}$$

Recall that the membrane is a dilute ideal solution, and there is an excess of supporting electrolyte. Therefore, one can describe the concentration of dianion adduct as being of order epsilon, a small parameter, and much smaller than the concentrations of the other ions. The concentrations of the other ions are of order one.

$$\begin{aligned} \tilde{C}_{Q2} &= O(\varepsilon) \quad \varepsilon << 1 \\ \tilde{C}_p &= O(1) \\ \tilde{C}_n &= O(1) \end{aligned} \tag{9}$$

At the boundaries, the fluxes of "p" and "n" are necessarily zero, because they do not participate in Faradaic reactions and they cannot enter nor exit the system.

The first step is to write the asymptotic series expansion in the small parameter epsilon for the concentrations and (dimensionless) electric potential.

$$\begin{aligned} \tilde{C}_{Q2} &= \varepsilon\tilde{C}_{Q2}^{(1)} + \varepsilon^2\tilde{C}_{Q2}^{(2)} + \ldots \\ \tilde{C}_p &= \tilde{C}_p^{(0)} + \varepsilon\tilde{C}_p^{(1)} + \varepsilon^2\tilde{C}_p^{(2)} + \ldots \\ \tilde{C}_n &= \tilde{C}_n^{(0)} + \varepsilon\tilde{C}_n^{(1)} + \varepsilon^2\tilde{C}_n^{(2)} + \ldots \\ \tilde{\phi} &= \tilde{\phi}^{(0)} + \varepsilon\tilde{\phi}^{(1)} + \varepsilon^2\tilde{\phi}^{(2)} + \ldots \end{aligned} \tag{10}$$

The method of regular perturbation analysis involves substitution of these series expansions in to the governing equations, and solving the resulting equations by grouping terms according to order of magnitude. [68] The leading order equations are:

$$\nabla\cdot\left[-D_p\vec{\nabla}\tilde{C}_p^{(0)} + -D_p z_p \tilde{C}_p^{(0)}\vec{\nabla}\tilde{\phi}^{(0)}\right] = 0 \tag{11}$$

$$\nabla\cdot\left[-D_n\vec{\nabla}\tilde{C}_n^{(0)} + -D_n z_n \tilde{C}_n^{(0)}\vec{\nabla}\tilde{\phi}^{(0)}\right] = 0 \tag{12}$$

$$z_p\tilde{C}_p^{(0)} + z_n\tilde{C}_n^{(0)} = 0 \tag{13}$$

The first two equations, combined with the no-flux boundary conditions for the inert ions, imply that the fluxes of those two ions must be constant and zero everywhere. The electroneutrality condition imposes an algebraic relationship between the concentrations of the two ions. Together, the three equations and two boundary conditions simplify to a system of two equations and two unknowns.

$$\frac{d\tilde{C}_p^{(0)}}{dy} + z_p\tilde{C}_p^{(0)}\frac{d\tilde{\phi}^{(0)}}{dy} = 0 \tag{14}$$

$$\frac{z_p}{z_n}\frac{d\tilde{C}_p^{(0)}}{dy} + z_p\tilde{C}_p^{(0)}\frac{d\tilde{\phi}^{(0)}}{dy} = 0 \tag{15}$$

The solution to this system is that the derivatives of the first-order concentration and the first-order potential are both zero. Therefore, at the leading order, the concentrations of the anion and cation are constant, and equal to their bulk values. Similarly, the leading order solution for the potential is a constant.

$$\tilde{C}_p^{(0)} = 1 \tag{16}$$

$$\tilde{C}_n^{(0)} = 1 = -\frac{z_p}{z_n}\frac{\overline{C}_p}{\overline{C}_n} \tag{17}$$

$$\tilde{\phi}^{(0)} = \frac{F\overline{\phi}^{(0)}}{RT} \tag{18}$$

The superscript "0" indicates the leading order value of that variable. The bar across the top of a term indicates an average value. The solution at leading order is constant concentrations and potentials because there is neither a convective nor diffusive transport of a charged species, and the net fluxes of charged species are zero, so the migration flux is zero and the potential, constant.

Given the solutions to the leading order equations, it is now possible to write down the O(ε) equations.

$$\nabla\cdot\left[-D_{Q2}\vec{\nabla}\tilde{C}_{Q2}^{(1)}\right]=0 \tag{19}$$

$$\nabla\cdot\left[-D_p\vec{\nabla}\tilde{C}_p^{(1)}+-D_pz_p\tilde{C}_p^{(0)}\vec{\nabla}\tilde{\phi}^{(1)}\right]=0 \tag{20}$$

$$\nabla\cdot\left[-D_n\vec{\nabla}\tilde{C}_n^{(1)}+-D_nz_n\tilde{C}_n^{(0)}\vec{\nabla}\tilde{\phi}^{(1)}\right]=0 \tag{21}$$

$$z_p\tilde{C}_p^{(1)}+z_n\tilde{C}_n^{(1)}+z_{Q2}\tilde{C}_{Q2}^{(1)}=0 \tag{22}$$

Equation (19) is the first conclusion from this analysis: the electromigration of dianion adduct is negligible to an approximation of order ε. The migration term in the O(ε) equation for dianion flux is zero because the gradient of the O(1) potential is zero (Equation (18)).

The current density is the sum of the flux of each ion multiplied by its charge (Equation (6)). The fluxes of the inert ions must be constant to satisfy the O(ε) governing equations (Equations (20) and (21)). The inert ions have zero flux boundary conditions, so the fluxes must be constant, and zero, everywhere. Therefore, the current is carried by the dianion adduct.

$$\vec{i}=F\left[z_p\vec{N}_p+z_n\vec{N}_n+z_{Q2}\vec{N}_{Q2}\right]=F\left(z_{Q2}\vec{N}_{Q2}\right) \tag{23}$$

Moreover, there is no contribution of migration at order (ε) to the dianion flux, so there is no migration contribution to current. In a one-dimensional system at steady state with an excess of inert ions, the diffusion of the dianion adduct is the entirety of the current (Equation (24)).

$$i_y=Fz_{Q2}\left(-D_{Q2}\frac{dC_{Q2}^{(1)}}{dy}\right) \tag{24}$$

Although the migration of dianion adduct is negligible, the potential gradient across the electrolyte is not zero. Instead, it is proportional to the current. This concept is best illustrated by examining the sum of ion fluxes in a slightly different format (Equation (25)).

$$\sum_k \frac{z_k}{D_k}\vec{N}_k = \frac{z_p}{D_p}\vec{N}_p + \frac{z_n}{D_n}\vec{N}_n + \frac{z_{Q2}}{D_{Q2}}\vec{N}_{Q2} \tag{25}$$

The fluxes of the inert cation and anion are zero. Therefore, the first conclusion from Equation (25) is that the sum of fluxes is equal to the dianion term. More specifically, the sum of the fluxes is proportional to the concentration gradient of the dianion.

$$\sum_k \frac{z_k}{D_k}\vec{N}_k = \frac{z_{Q2}}{D_{Q2}}\vec{N}_{Q2} = -z_{Q2}\frac{dC_{Q2}^{(1)}}{dy} \tag{26}$$

Expansion of the flux terms in Equation (25) produces another expression containing the sums of concentration and potential gradients.

$$\sum_k \frac{z_k}{D_k}\vec{N}_k = -\vec{\nabla}\left(\sum_k z_k C_k^{(1)}\right) + -\left(z_n^2\overline{C}_n + z_p^2\overline{C}_p\right)\vec{\nabla}\tilde{\phi}^{(1)} \tag{27}$$

Local electroneutrality ensures that the sum of each ion's concentration multiplied by its charge is zero, and the gradient of this sum is zero. Therefore, Equation (25) leads to a second conclusion: the sum of fluxes is proportional to the potential gradient.

Combining Equations (26) and (27) reveals the proportionality of the gradient in electric potential to the gradient in dianion concentration.

$$\sum_k \frac{z_k}{D_k}\vec{N}_k = -\left(z_n^2\overline{C}_n + z_p^2\overline{C}_p\right)\frac{d\tilde{\phi}^{(1)}}{dy} = -z_{Q2}\frac{dC_{Q2}^{(1)}}{dy} \tag{28}$$

In Equation (28), the potential gradient is proportional to the concentration gradient of dianion adduct because the dianion adduct is the only species that is both charged and electroactive. In Equation (24), the current is proportional to the concentration gradient of dianion adduct. Together, Equations (24) and (28) link the current to the potential in the electrolyte in the form of Ohm's Law.

$$\frac{d\tilde{\phi}^{(1)}}{dy} = i_y \frac{-1}{FD_{Q2}\left(z_n^2\overline{C}_n + z_p^2\overline{C}_p\right)} = \frac{-i_y}{\sigma} \tag{29}$$

To an approximation, the potential gradient in the electrolyte is linearly proportional to the current. The proportionality constant, σ, represents the bulk conductivity of the electrolyte. Notice that the bulk concentrations of supporting electrolyte determine the conductivity. The dianion concentration is so much smaller than the supporting electrolyte concentrations that it does not affect conductivity at the leading order.

To summarize, an excess of supporting electrolyte in a stagnant liquid membrane at steady state leads to the following physical and mathematical conclusions:

- Electromigration of the dianion adduct is negligible.
- The flux of the dianion adduct is constant and equal to its diffusive flux.
- The current is carried by the charged, electroactive species. In this system, there is only one: the dianion adduct. The current is carried by the diffusive flux of the dianion adduct.
- The electric potential gradient across the electrolyte is linearly proportional to the current. The gradient is constant across the electrolyte because the current is constant across the electrolyte (to an approximation of order ε).

Note that there is no electromigration of the dianion adduct at the same time that the potential gradient is linked to the flux of the dianion adduct. This result is because the presence of the electroactive species is only a small perturbation to the background concentration. The first order concentrations and potentials are constant. Chu says that the physical reason for this ambiguous relationship is that local electroneutrality combined with a gradient in the electroactive species forces a concentration gradient for the inert species. [67] Because the net fluxes of the inert ions must be constant and zero, an electric potential gradient must be nonzero to balance the nonzero concentration gradients. The reader is encouraged to consult Chu's thesis for more details on this work in classical electrochemical analysis. The conclusions listed above, embedded in Equations (24) and (29), are important for the rest of the derivation.

2.2.3 Potential gradients across electrode interfaces and the electrolyte membrane

The most general description of the potential gradient across an electrode interface recognizes the combined effects of thermodynamic, kinetic, and double layer effects. In this analysis, the electrode and chemical reactions are assumed to be so fast that the reactions are at equilibrium. The practical result of this assumption is that the potential drop across the electrode surface is equal to the equilibrium value and related to the local concentrations according to the Nernst equation. In addition, the concentrations of quinone and dianion adduct are assumed equal to their equilibrium values at the boundaries. Their concentration profiles are derived in the next section.

A derivation of the electric potential profile in the system begins with two definitions, Equations (30) and (31). The total potential drop across the electrode interface, $\Delta\phi$, is equal to the potential of the electrode ($\phi_{electrode}$) less the ionic potential in the adjacent electrolyte ($\phi_{electrolyte}$). The term $\Delta\phi^{eq}_{electrode}$ is the same potential difference at equilibrium.

$$\Delta\phi = \phi_{electrode} - \phi_{electrolyte} \tag{30}$$

$$\Delta\phi^{eq}_{electrode} = \phi^{eq}_{electrode} - \phi^{eq}_{electrolyte} \tag{31}$$

The equilibrium potential difference is the equilibrium half-cell potential for the di-reduction of a quinone, and it takes the form of the Nernst Equation (Equation (32)).

$$\Delta\phi^{eq}_{electrode} = E^0 - \frac{RT}{2F} ln\left[\frac{a_{Q^{2-}}}{a_Q}\right] \tag{32}$$

The terms describing equilibrium at the reference state are lumped in to the reference potential (E^0). R is the universal gas constant, T is the temperature, F is the Faraday constant, Q denotes the neutral quinone, and Q^{2-} denotes the dianion quinone. For an ideal, dilute solution, the activity coefficients are unity and the activities (a_Q,$a_{Q^{2-}}$) are equal to the concentrations of those species.

In a system where kinetic overpotentials are negligible, the actual potential difference is equal to the equilibrium value, so the right sides of Equations (30) and (31) are equal to each other. The combination of this equality and Equation (32) links the potential difference across an electrode interface to the concentrations adjacent to the electrode.

$$\phi_{cathode} - \phi(y=0) = E^0 - \frac{RT}{2F} ln\left[\frac{C_{Q^{2-}}(y=0)}{C_Q(y=0)}\right] \tag{33}$$

$$\phi_{anode} - \phi(y=h) = E^0 - \frac{RT}{2F} ln\left[\frac{C_{Q^{2-}}(y=h)}{C_Q(y=h)}\right] \tag{34}$$

Equations (33) and (34) describe the electrode potential drops across the cathode and the anode interfaces, respectively. The cathode is located at y = 0 and the anode is at y = h, where h is the membrane thickness.

The value of the ionic potential in the electrolyte is governed by Equation (29), and its values at the boundaries of the electrolyte appear in Equations (33) and (34). The derivation in Section 2.2.2 showed that the current is constant, so integration of the governing equation produces Equation (35).

$$\tilde{\phi}(y=h)-\tilde{\phi}(y=0)=-\frac{i_y}{\sigma}h \tag{35}$$

Combining Equations (33), (34), and (35) produces a single expression for describing potential changes in the circuit in a way that is analogous to Kirchoff's loop rule.

$$\phi_{cathode}-\phi_{anode}=\frac{i_y}{\sigma}h\frac{RT}{F}+\frac{RT}{2F}ln\left[\frac{C_Q(y=0)}{C_{Q^{2-}}(y=0)}\frac{C_{Q^{2-}}(y=h)}{C_Q(y=h)}\right] \tag{36}$$

The potential difference between the cathode and anode is a parameter called the "cell potential", V.

$$V\equiv\phi_c-\phi_a \tag{37}$$

The dianion quinone species reacts with CO_2 to produce a dianion adduct ($Q(CO_2)_2^{2-}$). To address that reaction, one can link the cell potential to the CO_2 partial pressure (p_{CO2}) by making three assumptions:

- The bulk, chemical reaction (Equation (2)) equilibrates quickly.
- The CO_2 in the gas phase equilibrates quickly with the dissolved CO_2 in the adjacent electrolyte.
- The concentration of CO_2 at the gas-liquid interface (C_{CO2}) is proportional to the adjacent partial pressure and the Henry's Law constant (H_{CO2}), as shown in Equation (38).

$$C_{CO_2}=\frac{p_{CO_2}}{H_{CO_2}(T)} \tag{38}$$

The equilibrium constant ($K_{b,eq}$) for the bulk chemical reaction is a function of the concentration of dianion quinone, dianion adduct, and dissolved CO_2. The partial pressure and Henry's law constant are substituted for the CO_2 concentration term in the equilibrium expression. Therefore, the equilibrium constant is related to the CO_2 partial pressure in the gas phase (Equation (39)).

$$K_{b,eq}=\frac{C_{Q(CO_2)_2^{2-}}}{C_{Q^{2-}}}\left(\frac{H_{CO_2}}{p_{CO_2}}\right)^2 \tag{39}$$

Substituting the equilibrium expression (Equation (39)) for the dianion concentrations in Equation (36) produces an expression of cell potential in terms of quinone concentrations and CO_2 partial pressures at the boundaries.

$$V = \frac{i_y}{\sigma} h \frac{RT}{F} + \frac{RT}{2F} ln \left[\frac{C_Q(y=0)}{C_Q(y=h)} \frac{C_{Q(CO_2)_2^{2-}}(y=h)}{C_{Q(CO_2)_2^{2-}}(y=0)} \frac{p^2(y=0)}{p^2(y=h)} \right] \tag{40}$$

The open-circuit potential (*OCV*) is the equilibrium potential when no current flows and there are no gradients within the cell. This is the minimum work to achieve the stated separation. Without gradients, the concentrations at the electrodes are equal to each other and the cell voltage simplifies to a function of the CO_2 partial pressures and the temperature.

$$OCV = V(i_y = 0) = \frac{RT}{2F} ln \left[\frac{p^2(y=0)}{p^2(y=h)} \right] \tag{41}$$

At this point, the current is carried by the diffusive flux of the dianion adduct, and the potential gradient is linearly proportional to this current. The potential drops across the electrode interfaces are equal to the equilibrium values according to the Nernst equation. The bulk chemical reaction that determines the relative amounts of absorbed and "free" CO_2 is also in equilibrium. These descriptions of potential drops and reaction equilibria are united in a single equation that links the cell potential to the current through the membrane, the concentrations of quinone and dianion at either interface, and the partial pressures of CO_2 in the gases adjacent to either electrode.

2.2.4 Quinone concentration profiles and current

Since the cell potential is a model input, Equation (40) has five unknowns: four concentrations and the current. The next step in the analysis is to connect the concentrations and gradients of neutral and dianion quinone to the current through the cell so that Equation (40) simplifies to a function of cell potential, current, and operating parameters. The quinone and dianion species have the same governing equation (Equation (4)), and at the boundaries, their concentrations are equal to the equilibrium ones. To simplify the derivation, the following symbols represent the concentrations at the anode ("*a*") and cathode ("*c*").

$$C_Q(y=0)=C_Q^c \qquad C_Q(y=h)=C_Q^a$$
$$C_{Q(CO_2)_2^{2-}}(y=0)=C^c_{Q(CO_2)_2^{2-}} \qquad C_{Q(CO_2)_2^{2-}}(y=h)=C^c_{Q(CO_2)_2^{2-}} \tag{42}$$

At this point, it is convenient to non-dimensionalize the concentration, spatial, and potential terms.

$$\Omega=\frac{C_{Q(CO_2)_2^{2-}}}{C^0_{Q(CO_2)_2^{2-}}} \qquad \Upsilon=\frac{C_Q}{C_Q^0} \qquad \tilde{y}=\frac{y}{h} \qquad \tilde{V}=\frac{FV}{RT} \tag{43}$$

The governing equations for the neutral quinone and dianion adduct in the membrane can be simplified to expressions of constant concentration gradients.

$$0=\frac{d^2\Omega}{\partial\tilde{y}^2} \qquad 0=\frac{d^2\Upsilon}{\partial\tilde{y}^2} \tag{44}$$

The assumption of fast electrochemical equilibrium at both the electrode interfaces leads to Dirichlet boundary conditions at both electrodes. The boundary conditions are listed below.

$$\Omega(\tilde{y}=0)=\Omega^c \qquad \Upsilon(\tilde{y}=0)=\Upsilon^c$$
$$\Omega(\tilde{y}=1)=\Omega^a \qquad \Upsilon(\tilde{y}=1)=\Upsilon^a \tag{45}$$

Integrating both differential equations in Equation (44) and applying the boundary conditions produces a set of two linear concentration profiles.

$$\Omega=\Omega^c+\tilde{y}\left(\Omega^a-\Omega^c\right) \tag{46}$$

$$\Upsilon=\Upsilon^c+\tilde{y}\left(\Upsilon^a-\Upsilon^c\right) \tag{47}$$

The current through the cell is proportional to the flux of the dianion adduct, which is proportional to the concentration gradient. The gradient and current are both constant, irrespective of position.

$$i_y=-Fz_{Q2}D_{Q2}\frac{dC_{Q(CO_2)_2^{2-}}}{dy}=\frac{-F(-2)D_{Q(CO_2)_2^{2-}}C^0_{Q(CO_2)_2^{2-}}}{h}\left(\Omega^a-\Omega^c\right) \tag{48}$$

Note that the diffusivity is not specifically the diffusivity of the dianion by itself. Rather, the assumption of local electroneutrality in the membrane implies that one can describe the diffusivity of the dianion as the geometric mean of its diffusivity and the diffusivity of the cation [68].

Physically, the net amounts of quinone and dianion adduct must remain constant because neither species can cross the boundaries. Also, all reactions are imposed at the boundaries as heterogeneous reactions. This integral constraint allows, mathematically, for conversion of the slopes and concentration profiles to functions of known physical parameters. The integral constraint is shown below in dimensional and dimensionless forms.

$$\frac{1}{h}\int_{y=0}^{y=h} C_{Q(CO_2)_2^{2-}}dy = C^0_{Q(CO_2)_2^{2-}} \qquad \int_0^1 \Omega d\tilde{y} = 1 \tag{49}$$

$$\frac{1}{h}\int_{y=0}^{y=h} C_Q dy = C^0_Q \qquad \int_0^1 \Upsilon d\tilde{y} = 1 \tag{50}$$

Substitution of the concentration profiles in to their respective integrals, followed by integration, produces algebraic equations relating the concentrations at the anode and cathode to each other and to the average, bulk concentration (which corresponds to a dimensionless value of 1). As a result, the average of the two boundary concentrations must equal the bulk average concentration.

$$\frac{\Omega^a + \Omega^c}{2} = 1 \tag{51}$$

$$\frac{\Upsilon^a + \Upsilon^c}{2} = 1 \tag{52}$$

Substitution of Equation (51) in to the expression for current (Equation (48) eliminates one of the boundary concentration terms.

$$i_y = \frac{4FD_{Q(CO_2)_2^{2-}}C^0_{Q(CO_2)_2^{2-}}}{h}\left(\Omega^a - 1\right) \tag{53}$$

The limiting current is the current at which the concentration of the electroactive species goes to zero. In this case, it is the current at which the concentration of dianion adduct at the anode approaches zero.

$$i_{\text{lim}} = \frac{4FD_{Q(CO_2)_2^{2-}}C^0_{Q(CO_2)_2^{2-}}}{h}\left(0 - 1\right) = -\frac{4FD_{Q(CO_2)_2^{2-}}C^0_{Q(CO_2)_2^{2-}}}{h} \tag{54}$$

Having established the expression for limiting current, one can defined a dimensionless current density with the limiting current as its scale.

$$\tilde{i} = \frac{i_y}{i_{\text{lim}}} = \frac{Ai_y}{I_{\text{lim}}} = \frac{I}{I_{\text{lim}}} = \tilde{I} \tag{55}$$

At this point it is convenient to continue the derivation using the expression for dimensionless current density, which combines the equations for current and limiting current.

$$\tilde{i} = 1 - \Omega^a \tag{56}$$

An equation relating the concentration of dianion adduct at the anode to the dimensionless current density is useful because it can be substituted in to the expression for the cell potential (Equation (40)). It is more useful to relate the potential to current than to concentration. Similarly, Equations (56) and (51) can be combined to describe the concentration of dianion adduct at the cathode in terms of current.

$$\Omega^c = 1+\tilde{i} \tag{57}$$

Using these expressions, it is possible to transform the expression for cell potential (Equation (40)) to one that is a function of the current density, the neutral quinone concentrations at the boundaries, and physical parameters. The updated expression for dimensionless cell potential is shown below.

$$\tilde{V} = \tilde{i}\frac{i_{\lim} h}{\sigma} + \frac{1}{2} ln\left[\frac{\Upsilon^c}{\Upsilon^a}\frac{1-\tilde{i}}{1+\tilde{i}}\frac{p^2(y=0)}{p^2(y=h)}\right] \tag{58}$$

The last step is to link the dimensionless quinone concentrations to the current. The same integral constraint that applies to the dianion adduct also applies to the neutral quinone. Moreover, conservation of mass at the interfaces requires that the flux of the neutral quinone be equal and opposite to the dianion adduct flux at both electrodes. The fluxes are constant, so this constraint produces the following equation.

$$-D_Q \frac{C_Q^0}{h}\frac{d\Upsilon}{d\tilde{y}} = D_{Q(CO_2)_2^{2-}} \frac{C^0_{Q(CO_2)_2^{2-}}}{h}\frac{d\Omega}{d\tilde{y}} \tag{59}$$

The concentration gradients are related to the concentrations at both the boundaries via the derivatives of the concentration profiles (Equations (46) and (47)). Both the dianion adduct boundary concentrations can be replaced with expressions involving the dimensionless current density (Equations (56) and (57)). One of the neutral quinone boundary concentrations can be eliminated using Equation (52). The outcome of this algebra is a relationship between the dimensionless quinone concentration at the cathode, the dimensionless current density, and physical parameters.

$$1-\Upsilon^c = \tilde{i}\frac{D_{Q(CO_2)_2^{2-}}}{D_Q}\frac{C^0_{Q(CO_2)_2^{2-}}}{C_Q^0} = \tilde{i}R_D R_C \tag{60}$$

The terms R_D and R_C are dimensionless ratios of the diffusivity and average concentrations.

$$R_D = \frac{D_{Q(CO_2)_2^{2-}}}{D_Q} \qquad R_c = \frac{C^0_{Q(CO_2)_2^{2-}}}{C^0_Q} \tag{61}$$

Using a similar procedure, it is possible to produce an expression relating the dimensionless concentration of neutral quinone at the anode to the dimensionless current density. The expressions for both boundary concentrations are summarized below.

$$\begin{aligned} \Upsilon^c &= 1 - R_D R_C \tilde{i} \\ \Upsilon^a &= 1 + R_D R_C \tilde{i} \end{aligned} \tag{62}$$

The purpose of this derivation is to express the (dimensionless) concentrations of neutral quinone and dianion adduct in terms of the (dimensionless) current density, so that those terms can be eliminated from the expression for the cell potential.

2.2.5 Analytical relationship between current and voltage

Now it is possible to express the concentrations of the quinone species at the electrodes as functions of the current. The term $\tilde{i}$ refers to the actual current density (i) normalized to the limiting current based on the dianion adduct. The expression for limiting current is derived in Section 2.2.4. Substitution of the expressions in Equation (62) in to Equation (58) produces an analytical expression relating the current and voltage through this system.

$$\tilde{V} = \frac{\tilde{i}}{\tilde{\sigma}} + \frac{1}{2} ln\left[\left(\frac{1 - R_D R_C \tilde{i}}{1 + R_D R_C \tilde{i}}\right)\left(\frac{1 - \tilde{i}}{1 + \tilde{i}}\right)\left(\frac{p_c^{\,2}}{p_a^{\,2}}\right)\right] \tag{63}$$

This is the analytical relationship between current and potential under the assumptions and conditions of this model. Note the Ohm's Law expression for the potential drop across the electrolyte has been non-dimensionalized. The dimensionless conductivity can be described as the conductivity from the supporting electrolyte divided by the conductivity from the electroactive species, the dianion adduct. The expression for dimensionless conductivity is derived from the relationship between the conductivity and the limiting current.

$$\tilde{\sigma} \equiv \frac{\sigma}{i_{\lim} h} = -\frac{z_n^2 \bar{C}_n + z_p^2 \bar{C}_p}{4 C^0_{Q(CO_2)_2^{2-}}} \tag{64}$$

This expression for dimensionless conductivity embodies the physical ramifications of an excess of supporting electrolyte. By applying the definitions of the dimensional conductivity (Equation (29)) and the limiting current (Equation (54)), one can simplify the dimensionless conductivity to a ratio of the ionic strength from the inert ions to the ionic strength of the electroactive species. In the perturbation analysis, the dianion concentration was approximately ε, where $\varepsilon \ll 1$, while the inert ion concentrations were approximately one. Therefore, the scale of the dimensionless conductivity is $1 / \varepsilon$. Physically, an excess of supporting electrolyte produces a large ionic conductivity and therefore small ohmic losses across the membrane.

2.3 Results and discussion

The analytical expression for cell voltage as a function of current, Equation (63), can be interpreted as the potential required to separate CO_2 from the flue gas (at the cathode) to the enriched gas (at the anode) at a given flux (current). It embodies the relationship between energy efficiency and CO_2 flux. In this case, energy efficiency is defined as the open circuit voltage divided by the actual voltage. Figure 2.2(a) is the cell potential as a function of normalized current, which is calculated from assumed values for R_D and R_C. Figure 2.2(b) highlights energy efficiency (*OCV* over actual cell potential, *V*) as a function of normalized current.

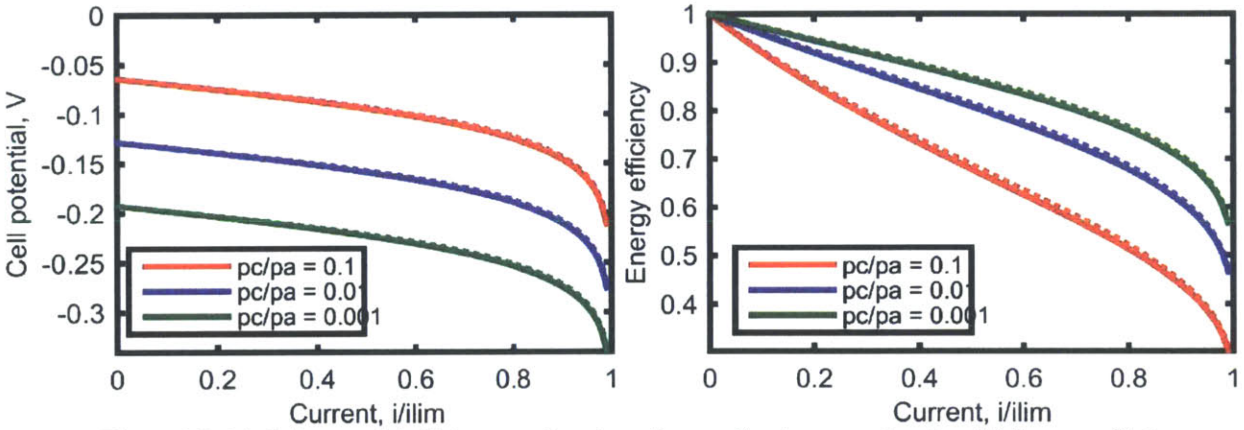

Figure 2.2 (a) Cell potential, Volts, as a function of normalized current density. (b) Energy efficiency as a function of normalized current density. R_D*R_C is assumed to be unity, and T = 50°C.

Figure 2.2(a) is a plot of cell potential (V) as a function of dimensionless current (i/i_{lim}) for three pressure ratios and three values of the electrolyte conductivity. All of the data in Figure 2.2 are results for a system at 50°C when the product "$R_D R_C$" is assumed to be unity. The solid line represents "infinite" conductivity (negligible Ohmic resistance), the dashed line is for a dimensionless conductivity of 10, and the dot-dashed line is for a dimensionless conductivity of 100. All three lines overlap strongly, which means that as long as there is an excess of inert ions (10:1 ratio or larger), the electrolyte conductivity does not affect the cell potential nor the energy efficiency dramatically.

Figure 2.2(a) shows that as the current approaches the limiting current, the marginal increase in cell potential increases. The energy demand increases sharply when the current approaches the limiting current, and it diverges at a normalized current of one. At the limiting current, the potential diverges because of a phenomenon called "concentration polarization". The limiting current is defined as the current (flux) at which one or more electroactive species is depleted. When the current is near the limiting value, higher applied potentials cannot increase the current because the concentration at the surface is nearly zero. The term "$R_D R_C$" determines which species is rate-limiting. The term "R_D" is the ratio of the diffusivities of the dianion adduct to the diffusivity of the neutral quinone. If R_D is greater than unity, then the dianion adduct diffuses faster than the neutral quinone. R_D is determined by the chemistry of the system. R_C, the concentration ratio, is a parameter that can be set within the bounds of the solubility limits for the dianion adduct and the neutral quinone. If the product "$R_D R_C$" is greater than unity, then the neutral quinone depletes faster than the dianion adduct because it has a lower permeability; the converse is true when that product is less than unity. Ideally, it should be as close to unity as possible, meaning that the two species deplete at the same rate.

Figure 2.2(b) shows the energy efficiency for operation at different dimensionless currents and different pressure ratios. Here, energy efficiency is defined as the actual work (voltage) divided by the thermodynamic minimum, the open circuit potential. The energy efficiency decreases steadily with increasing current. Near the limiting current, the energy efficiency drops exponentially because the cell potential required to achieve the limit in concentration gradients is large. The system is more energy efficient at all currents when the pressure ratio is more extreme ($p_c/p_a = 0.001$ versus 0.01 or 0.1). At high pressure ratios, the minimum work is much higher to perform that separation, so the increase in work caused by operation at increasing current is a smaller fraction of the whole energy cost. According to this metric, this system of carbon capture is more attractive for capture from increasingly dilute sources.

In general, the performance of a large scale system for carbon capture is decided according to the metrics of energy cost and capital cost. The capital cost is a function of the size of the system, and the size is inversely proportional to the current density. A higher current density achieves a higher CO_2 flux across the membrane and therefore requires lower membrane area. By extension, the relationship between current and potential for an electrochemical system of carbon capture represents the relationship between capital cost (membrane area, system size) and energy cost. A lower operating current density means a lower energy penalty for CO_2 capture. At the same time, operating at a lower current density also increases the total area needed to achieve a separation at scale. Therefore, the current-potential (*I-V*) relationship determines the inherent tradeoffs that affect attempts to minimize both energy and capital costs.

The physical separation of the gas phases in an ECMS cell creates a gradient in CO_2 partial pressures that opposes the facilitated transport and drives "back-diffusion" of CO_2 across the membrane. One can define the transport efficiency (θ) as the net CO_2 flux across the cell divided by the flux of charge. Equation (65) is an expression of current efficiency as a function of partial pressures, current, and membrane permeability.

$$\theta = 1 - \frac{1}{4}\frac{D_{CO_2}}{D_{Q(CO_2)_2^{2-}}}\frac{p_a/H}{C^0_{Q(CO_2)_2^{2-}}}\left(1 - \frac{p_c}{p_a}\right)\left(\frac{1}{\tilde{i}}\right) \tag{65}$$

The current efficiency increases with increasing current and increasing quinone diffusivity and concentration. The solubility limit of dianion adduct in the solvent at the operating temperature sets the upper bound for the average concentration of that species. Similarly, the solubility and desired concentration ratio (R_C) value set the upper bound for the average concentration of neutral quinone. The solubility limit of supporting electrolyte in the solvent, and the desire for an excess of supporting electrolyte, also affects the bounds of the possible average concentration values. Current efficiency decreases with increasing CO_2 permeability and decreasing pressure ratio. The pressure ratio is the ratio of the cathodic pressure (lean gas) and the anodic pressure (enriched gas). The term H is the Henry's law constant for CO_2 in the solvent. The parameters used for this analysis are summarized in

Table 1. Note that all of the parameters used apply for a system in dimethyl sulfoxide (DMSO) solvent.

For design of the planar membrane cell for carbon capture, the supported liquid membrane should be as thin as possible. The current density is inversely proportional to membrane thickness, so thinner membranes produce higher currents, holding all other parameters constant. Also, the current efficiency is unaffected by membrane thickness, because a thinner membrane increases the "forward" facilitated transport of CO_2 via quinone to the same degree that it increases the "backward" diffusion of CO_2. Therefore, the optimal membrane thickness is the smallest value possible. The risk of short-circuiting via conduction through the membrane itself is a practical constraint to the membrane thickness that depends on the conductivity of the polymer separator itself. While not a direct constraint to the membrane, the risk of "blowing" the electrolyte out of the support is a practical concern. Therefore, designers should minimize gradients in total pressure across the membrane.

The power density can be calculated directly from the equation for cell potential (Equation (63)) and the limiting current density (Equation (54)). The rate of CO_2 capture is the product of the current and the current efficiency (θ). Another way to examine these data is to consider the energy penalty per kg CO_2 captured and to observe its changes as a function of CO_2 flux. Figure 2.3 contains plots of the power density, in W/m^2, and the energy cost per unit CO_2 (kJ/kg) as functions of CO_2 mass flux (kg/m^2/hr).

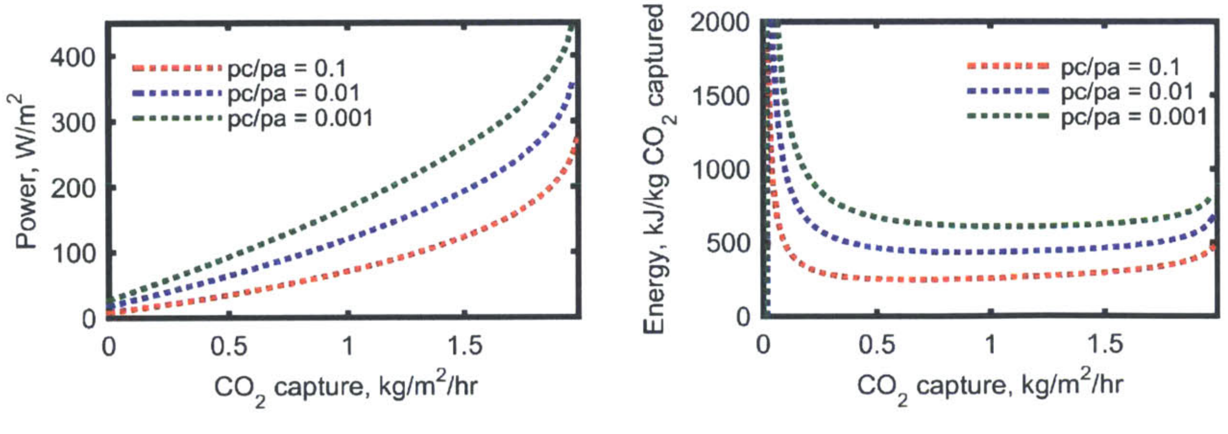

Figure 2.3 (left) Power density, W/m^2, as a function of CO_2 flux (kg/m^2/hr). (right) Energy penalty, kJ/kg CO_2, as a function of CO_2 flux (kg/m^2/hr).

The power curves in Figure 2.3 mimic the current-voltage plots in Figure 2.2. The power increases linearly with CO_2 flux until the point of divergence at limiting current. The energy cost per kg CO_2 is exponentially high at low CO_2 capture rates because the *net* CO_2 flux approaches zero. This phenomenon is mostly an artifact of the way the model it set up. At low current, the rate of CO_2 capture approaches the rate of back-diffusion in the model and the net transport of CO_2 approaches zero. When the electric power is divided by a very small CO_2 capture rate, the resulting value is very high. However, in reality, these numbers are irrelevant because at low currents, the partial pressure of CO_2 in the enriched gas would probably not reach the 1 bar value anyway, so the back diffusion would be less than that predicted by the model. The energy penalty is comparatively invariant with CO_2 capture at moderate fluxes, compared with the values near the high and low ends. The relatively small changes in energy per kg CO_2 in the ranges of 0.5 to 1.5 kg/m^2/hr suggest that optimal cell operation should be near the upper end of that range. At a rate of 1.5 kg/m^2/hr, the energy cost per kg CO_2 is near the minimum value for the system, and being at the high end of the range for which energy cost is minimal will help to minimize the membrane area and capital cost.

Table 1 Table of physical parameters for membrane analysis

Parameter	Symbol	value
Solvent		DMSO
Diffusivity of CO_2 in solvent [69]	D_{CO_2}	5 x 10^{-9} m^2/s
Diffusivity of dianion adduct*	$D_{Q(CO_2)_2^{2-}}$	7 x 10^{-10} m^2/s
Henry’s law constant (40°C, combined with density data) [70, 71]	H	17.5 bar-L/mol
Bulk concentration of dianion quinone	$C^0_{Q(CO_2)_2^{2-}}$	1 M
Partial pressure of CO_2 at the cathode (flue gas, lean gas)	p_c	0.001 to 0.1 bar
Partial pressure of CO_2 at the anode (rich gas)	p_a	1 bar
Membrane thickness	h	200 μm
Temperature	T	50°C
Dimensionless conductivity (assumed)	$\tilde{\sigma}$	10 (unless otherwise specified)

2.4 Conclusions and suggestions for future work

This chapter is an analysis of a novel implementation of the quinone as a vehicle for facilitated transport across a supported liquid membrane. The cell design is inspired by the design of the classic hydrogen fuel cell, except that the polymer electrolyte membrane of the fuel cell is replaced with a supported liquid membrane. The supported liquid membrane consists of a thin, porous, polymer separator wetted with an electrolyte composed of neutral quinone, dianion adduct, and supporting electrolyte dissolved in dimethyl sulfoxide. The first part of this chapter is a description of the governing equations and boundary conditions needed to solve for the concentration and potential profiles in the system. What follows the model set up is a derivation showing that an excess of supporting electrolyte relative to the electroactive species creates an environment in which the following statements are approximately true:

- Electromigration of the dianion adduct is negligible.
- The flux of the dianion adduct is constant and equal to its diffusive flux.

- The current is carried by the diffusive flux of the dianion adduct.

The electrochemical and chemical reactions involved in the mechanism for the redox-responsive absorption of CO_2 were condensed to a system of two reaction equations: one Faradaic reaction and one bulk, chemical reaction. Solution of the mass transfer equations, integration of the potential gradient, and application of the equilibrium expressions produce an analytical equation that couples the cell potential to the current through the membrane.

The analytical model allows for calculation of voltage, current, power, efficiency, and carbon capture rate for a given set of operating parameters and physical properties. The results show that the impact of ohmic resistance across the electrolyte is negligible relative to the overall voltage. In addition, the cell is more energy efficient for carbon capture from more dilute gas streams. A derived expression for current efficiency shows the set of physical and operating parameters that affect the amount of current required to capture a given amount of CO_2. The results show that the physical chemistry should be optimized for maximum quinone permeability, and relatively low CO_2 permeability. The best case scenario is an electrolyte that is soluble enough that there is no resistance associated with CO_2 dissolution in to the electrolyte, but is otherwise relatively impermeable to CO_2 and other gases. Finally, the membrane should be as thin as possible, because the facilitated transport is inversely proportional to membrane thickness, while the current efficiency is unaffected by that parameter.

The equations for cell potential and current are sufficient for calculating the electric power, energy efficiency, and carbon capture rates for the system at various operating conditions. The electric power and net energy cost per unit CO_2 are plotted as functions of CO_2 flux for a typical set of membrane physical parameters. The energy penalty for carbon capture is surprisingly invariant with CO_2 flux when the flux is in the range of 0.5 to 1.5 kg/m^2/hr. For optimal performance, the cell should run near the upper limit of this range because the membrane area can be as low as possible at high fluxes without excessive increases in energy costs.

2.5 Solvent loss

The solvent for this kind of membrane must be a polar, aprotic organic solvent that will not break down in the range of the redox potentials of the quinone. The neutral quinone, the dianion adduct, and the supporting electrolyte should be highly soluble and mobile in the solvent. In addition, it must be non-volatile and it must have a low viscosity (to minimize mass transfer resistance). As a result of these design criteria and preliminary electrochemical experiments, propylene carbonate (PC) and dimethyl sulfoxide (DMSO) have been selected as solvents for ECMS.

Even though PC and DMSO are ten times less volatile than water, preliminary results indicate that an ECMS cell would bleed solvent at an unacceptably high rate.

At a temperature of 50°C, a cell designed to capture 100,000 kg/hr CO_2 would lose solvent at a rate of 370 kg/hr for PC and 7900 kg/hr for DMSO. Assuming the gas flow channels are similar to those used for fuel cells, one can expect flue gas residence times on the order of seconds. Collaborators at Siemens showed that a residence time of 0.3 seconds is enough to reach equilibrium concentrations of solvent (propylene carbonate) in the flue gas [unpublished results]. At this rate, the cell would lose at least 0.01 kg solvent per kg of CO_2 captured. Aside from the environmental impact of leaching solvent, solvent loss also threatens the functionality of the cell. Any part of the electrode that is not wetted is not participating in the facilitated transport process. Even a ten percent reduction in solvent may be enough to shut down the cell completely.

Efforts to continuously replace the solvent in this system might introduce significant cost and complexity. Ionic liquids are nonvolatile and could function as both solvent and supporting electrolyte. However, the ionic liquid must be designed carefully because ionic liquids are often highly viscous. Recall that the limiting current is directly proportional to the diffusion coefficients of the neutral quinone and the dianion adduct. A tenfold increase in solvent viscosity (by switching to ionic liquids) imposes a tenfold decrease in the limiting current density of the system by reducing the diffusivity. However, researchers in the field are producing ionic liquids that can be optimized for electrochemical applications.

The issue of solvent loss led to interest in electrochemical capture of CO_2 with alternative designs that could address the solvent loss. A design with a flowing electrolyte was attractive for two reasons: (1) in laminar flow, the system would be mass transfer limited within a thin boundary instead of the entire membrane thickness, and (2) any solvent that evaporated could be more easily replenished in the recycle stream. Research in to demonstration and optimization in the planar membrane configuration was abandoned in favor of more novel designs (Chapter 3) and an alternative redox couple (Chapters 4,5,6).

3 Design analysis of powered CO_2 capture in a flowing electrolyte

3.1 Motivation and description

The switch from a stagnant, planar supported liquid membrane to a flowing electrolyte membrane is advantageous for several reasons:

- A flow system is diffusion-limited only within a thin boundary layer instead of across the entire membrane thickness.
- A recirculating electrolyte allows for easy replenishment/replacement of solvent, which is important for an electrolyte that may evaporate (even slightly) under normal operating conditions.
- A flowing electrolyte is not susceptible to the risk that solvent evaporation would disrupt the electric circuit.
- A flow system has better mass transfer than a stagnant film, but under the right conditions, laminar flow of the electrolyte prevents reactant crossover, which would effectively "short" the circuit and reduce the current efficiency.

In this section, a numerical model is developed for a carbon capture device designed with laminar flow of an electrolyte between two planar electrodes. One electrode is porous, and is the site of CO_2 absorption. The other electrode is nonporous. Desorption of CO_2 happens in a separate flash tank. There are several operating parameters, including cell voltage and the CO_2 concentration in the recirculating electrolyte. Quantification of the energy requirements and carbon capture rate requires the ability to quantify the current, potential, and CO_2 flux in the electrochemical cell. Therefore, a numerical model is articulated and developed to inform the design analysis by providing those data as functions of operating parameters. The design analysis produces estimates for the energy requirement of CO_2 capture using these configurations, and it highlights those operating parameters that are most important for future design and execution.

Experimental investigation was achieved for a subset of the ideas presented here. Section 4 highlights experimental results that validate the concept of coupling the quinone/dianion adduct electrochemical reaction to the ferrocene/ferrocenium electrochemical reaction. Chapter 5 contains experimental results for the quinone-ferrocene system in a flow configuration in which the electrolyte recirculates between two planar electrodes. Chapter 6 contains experimental results for the quinone-ferrocene chemistry in a device where the electrolyte flows through two large porous electrodes.

The figure below shows a simplified schematic of a design that has a porous cathode.

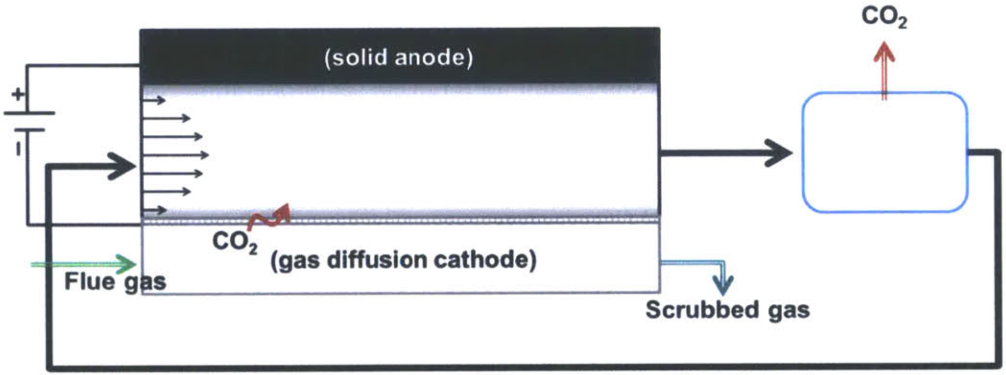

Figure 3.1 Simplified schematic of the laminar flow electrolyte cell configuration.

There is a porous, planar cathode at the lower interface (parallel to the flow direction), and the black box at the top is the solid anode. The thick black arrow shows the path of the flowing electrolyte, which flows continuously through the active zone (the space between the two electrodes) and gets recirculated continuously. CO_2 enters the gas diffusion cathode as part of the flue gas (green arrow) and the scrubbed gas exits at the other end (teal arrow). CO_2 is absorbed at the porous cathode (shown as a red arrow), and it desorbs at the downstream flash tank (the red arrow coming out of the blue box).

There is electrochemical reduction of the quinone at the cathode, and the dianion absorbs CO_2 from the adjacent gas phase (flue gas). Upon oxidation, the dianion adduct desorbs the CO_2. Oxidation can happen electrochemically at the anode or chemically, with a chemical oxidant. After oxidation, CO_2 is desorbed across a free surface, and the electrolyte is regenerated and recycled to the cell entrance.

In this system, the dianion adduct never travels directly from the cathode to the anode in a single pass. Rather, there are bulk, steady-state concentrations of CO_2, dianion adduct, and neutral quinone in the middle of the flowing electrolyte. Each species moves from the bulk, across the diffusion boundary layers, to the electrode surfaces. The system should be designed to maximize mass transfer, current efficiency (in terms of CO_2 captured per electron), and energy efficiency.

The remainder of this chapter begins with development of a numerical model and a design analysis for the flow configuration. A description of the system in which the quinone/dianion is coupled to the same chemical reaction at the anode is meant to orient the reader to the chemical activity that occurs at the electrodes. Then, the coordinate system, the governing equations, and the boundary conditions of the model are described. The results from numerical simulation for a typical set of operating conditions are presented and discussed. The rest of the chapter is an exploration of the effects of several parameters on the cell performance, namely the energy input and CO_2 capture.

3.2 The design of the electrochemical cell

This electrochemical cell operates with the same chemistry as the supported liquid membrane (Chapter 2). An electrolyte composed of quinone, dianion adduct (and the cation to balance the charge), and supporting electrolyte circulates continuously between two planar electrodes. One electrode is solid, the other is porous. Figure 3.2 is a diagram of the electrochemical cell and the reactions that happen at each electrode.

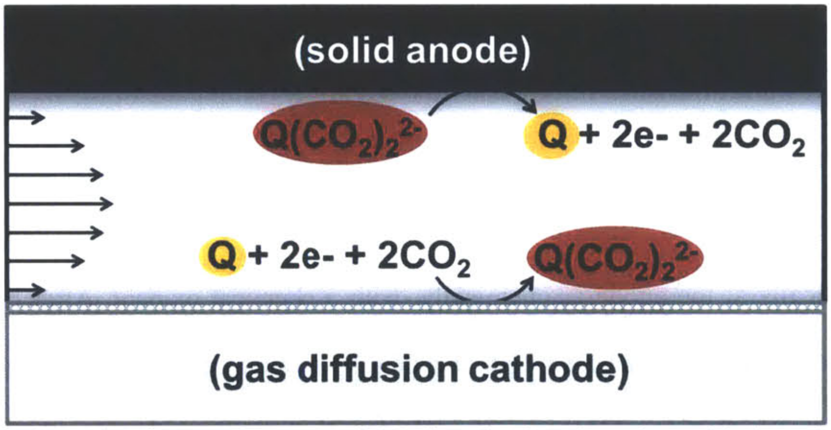

Figure 3.2 Schematic of powered capture of CO_2 in a flowing electrolyte with the quinone-dianion adduct ($Q\text{-}Q(CO_2)_2^{2-}$) couple. Quinone is reduced at the cathode, and absorbs CO_2 from the adjacent gas. Dianion adduct is oxidized at the anode to desorb CO_2.

Since the electrochemical reactions are coupled to each other, the minimum, open circuit voltage is only dependent on the relative amounts of CO_2 in the electrolyte and in the gas phase at the cathode boundary. Typically, the open circuit potential of a cell is the difference in the standard potentials of the reactions at each electrode. In this case, those reactions are identical. If the CO_2 partial pressures at both electrodes were equal to each other everywhere, then the open circuit potential of the cell would be zero. The fact that they are (usually) different is the only reason the open circuit potential is nonzero. Even so, the fact that there is no net reaction in the electrochemical cell should minimize the thermodynamic potential component of the energy input.

The oxidation of the dianion adduct occurs at a solid anode, which means the desorbed CO_2 remains physically in the electrolyte. This material is swept out of the system by advection. If the rate of oxidation is high enough, it is possible to desorb so much CO_2 as to create regions in which the electrolyte is supersaturated. When the total pressure of the electrochemical cell is at atmospheric pressure, then the excess CO_2 will evaporate out of the electrolyte when it encounters a free surface. This concept is advantageous, because the more CO_2 that can be captured this way, the less energy is required to vacuum off the remaining CO_2 to regenerate the electrolyte.

Figure 3.3 is a process flow diagram for the quinone-dianion chemistry in laminar flow between two electrodes with the additional equipment to complete the system. The electrolyte, containing quinone, dianion, dissolved CO_2, and supporting electrolyte, enters the electrochemical cell, and absorbs CO_2 at the porous cathode. As it exits the cell, the electrolyte is split to create two streams: one that is supersaturated in CO_2, and one that is not. The electrolyte that is supersaturated released the extra CO_2 in a flash tank. The electrolyte that exits this equipment is saturated in CO_2, and it recombines with the rest of the fluid before moving to another flash tank. A throttle (not shown) is required upstream to regulate the pressure and prevent the vacuum pump from sucking the electrolyte out of the cell and out of the other flash tank. The vacuum pump removes the remaining CO_2, and pumps the electrolyte back up to pressure and back to the cell inlet.

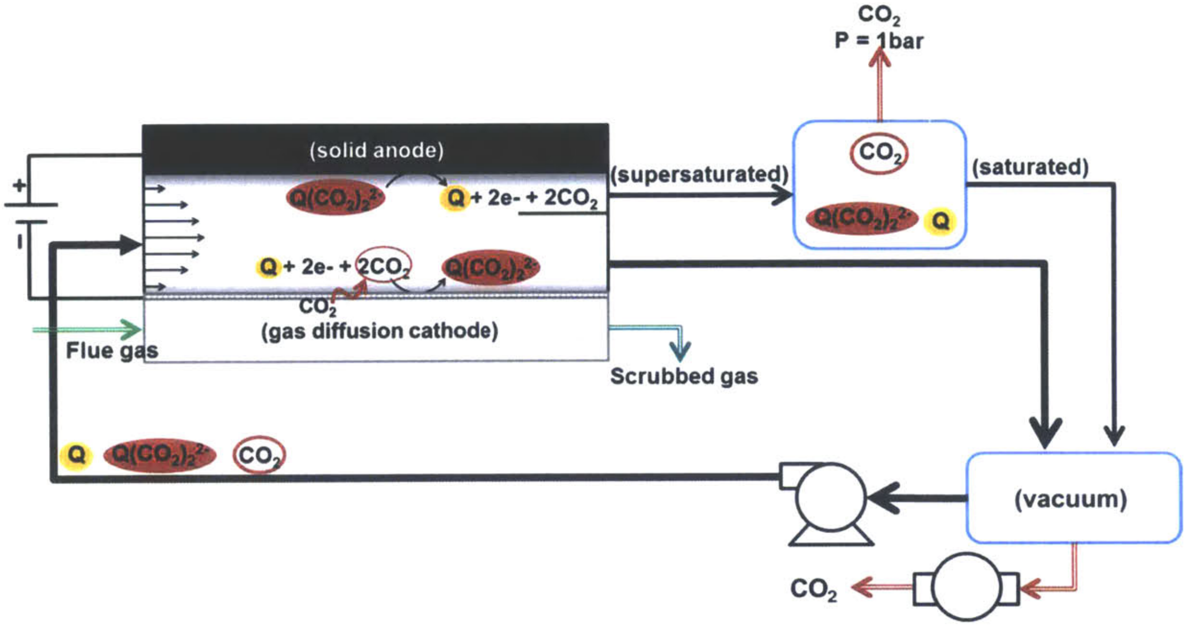

Figure 3.3 Process flow diagram for quinone-dianion chemistry in laminar flow between two planar electrodes. The electrolyte is split at the outlet, so that supersaturated CO_2 is collected at a flash tank, and a vacuum tank collects the remaining CO_2.

The concepts of supersaturated CO_2 and minimal open circuit potentials are two important advantages of this design.

3.2.1 Assumptions, coordinate system, and governing equations

The following assumptions are included in the numerical simulation of the electrochemical cell:

- Chemical solutions can be considered ideal and dilute.
- The dimensions of the membrane and electrodes are such that one can model the transport as two-dimensional.
- The electrodes are treated as thin, which implies the electrochemical reactions are approximately heterogeneous.
- The kinetics of electrochemical and chemical reactions are so fast that it is assumed the species are in equilibrium at the electrodes.
- At the boundaries, the dissolved CO_2 is assumed to equilibrate quickly with the CO_2 in the adjacent gas phase. The concentration of dissolved CO_2 is assumed to follow Henry's law behavior. [72]

- The physical properties of the electrolyte remain constant under the operating conditions.
- Local electroneutrality is assumed. Double layer effects are neglected.
- The diffusivity of the dianion adduct is the ambipolar diffusivity for the dianion adduct and the inert cations that balance the charge.

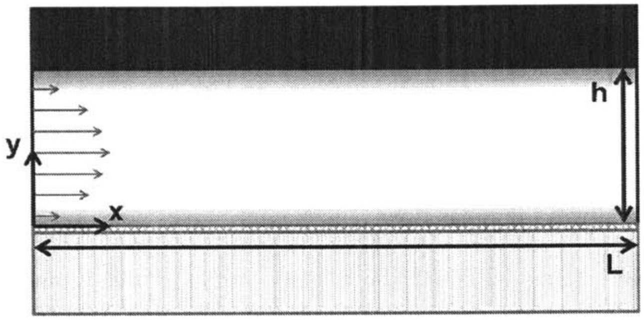

Figure 3.4 Coordinate system and dimensions for flowing electrolyte membrane. The origin is in the lower left corner of the channel.

The modeling in this section employs the coordinate system shown in Figure 3.4. Note that the origin is in the lower left corner of the channel where the electrolyte flows. The cathode is modeled as a vanishingly thin planar interface at y = 0. The anode is modeled as a thin planar interface at y = h.

There are six field variables in the model. Five of them are species concentrations, and the sixth is the ionic potential. The five species are neutral quinone, dianion adduct, unbound CO_2, inert anion, and inert cation.

The governing equations for species concentrations all take the same form for a system at steady state (Equation (66)). The vector $\vec{N}_k$ is the molar flux vector for species *k*.

$$\vec{\nabla} \cdot \vec{N}_k = 0 \tag{66}$$

The molar flux is calculated using the Nernst-Planck equation (Equation (67)).

$$\vec{N}_k = C_k \vec{v} - D_k \left[\vec{\nabla} C_k + z_k C_k \frac{F}{RT} \vec{\nabla} \phi \right] \tag{67}$$

The governing equation for the electric potential is the equation for conservation of current.

$$\vec{\nabla} \cdot \vec{i} = 0 \tag{68}$$

The electric current is carried by dissolved ions, so the current density is the sum of ionic fluxes multiplied by their charges and the Faraday constant (Equation (6)).

In a system modeled as locally electroneutral, the expression for that condition replaces Poisson's equation as the sixth governing equation. The term z_k is the charge of species k.

$$\sum_k z_k C_k = 0 \tag{69}$$

In a dilute solution in which the movement of species does not affect the flow, the velocity profile is decoupled from the mass conservation equations. The flow of the electrolyte is assumed fully-developed everywhere, and the flow is always laminar flow. The Navier-Stokes equation is solved analytically, and the velocity profile is treated as a model input. The velocity profile for this geometry is shown below. The derivation of the velocity profile from the Navier-Stokes equation for this specific geometry is presented in an appendix, Chapter 0.

$$v_x(y) = 6U\left[\frac{y}{h} - \left(\frac{y}{h}\right)^2\right] \tag{70}$$

The velocity (v_x) is a function of the average velocity (U) and the distance from the electrode wall (y). The average velocity is a function of the pressure drop down the length of the channel, the channel height (h), and the fluid viscosity (μ).

$$U = \frac{h^2}{12\mu}\left(\rho g_x - \frac{1}{L}\frac{\partial P}{\partial \tilde{x}}\right) \tag{71}$$

In this work, the governing equations are solved numerically in two dimensions using a finite volumes method. The spatial field (the flow channel) is discretized into a grid of n_x by n_y boxes. For each one of the $n_x n_y$ boxes, the discretized volumetric conservation equation for each species and for the current is solved. Equation (72) is the species conservation for species k in the i^{th} box. The tilde indicates a dimensionless term.

$$0 = \frac{\Delta \tilde{c}_{k,i}}{\Delta \tilde{t}} + \frac{\tilde{N}_{k,\tilde{y},i+1} - \tilde{N}_{k,\tilde{y},i}}{\Delta \tilde{y}} + \frac{\tilde{N}_{k,\tilde{x},i+1} - \tilde{N}_{k,\tilde{x},i}}{\Delta \tilde{x}} \tag{72}$$

The "N" term is the dimensionless flux of species k across the face of the i^{th} box in the y- or x-direction (denoted by the subscript). The boundary conditions determine the fluxes across the yz- and xzplanes at the boundaries. In the numerical model, the equations are integrated until the value of the time derivative is zero. All results presented in this work are for systems at steady-state.

3.2.2 Boundary conditions

For clarity and brevity, each species is denoted by a subscript. The dianion adduct is "*Q2*", the neutral quinone is "*Q*", the dissolved carbon dioxide is "*CO_2*", the inert anion is "*N*", and the inert cation is "*P*". The current is "*J*". The coordinates are non-dimensionalized by dividing by the channel height and length.

$$\tilde{y}=\frac{y}{h} \qquad \tilde{x}=\frac{x}{L} \tag{73}$$

3.2.2.1 *Inlet and outlet boundary conditions*

The electrolyte at the inlet to the channel is a well-mixed fluid. The concentrations are equal to the bulk values for all species at the inlet. The x-direction flux for the current is simply the sum of the x-direction fluxes of the charged species, multiplied by their charges.

$$C_{Q2}\left(\tilde{x}=0,\tilde{y}\right)=C_{Q2}^{0} \tag{74}$$

$$C_{Q}\left(\tilde{x}=0,\tilde{y}\right)=C_{Q}^{0} \tag{75}$$

$$C_{CO_2}\left(\tilde{x}=0,\tilde{y}\right)={}^{\lambda}\!/_{H} \tag{76}$$

$$C_{N}\left(\tilde{x}=0,\tilde{y}\right)=C_{N}^{0} \tag{77}$$

$$C_{P}\left(\tilde{x}=0,\tilde{y}\right)=-{}^{z_N}\!/_{z_P}\,C_{N}^{0}+{}^{2}\!/_{z_P}\,C_{Q2}^{0} \tag{78}$$

$$J\left(\tilde{x}=0,\tilde{y}\right)=\sum_{k} z_k N_k\left(\tilde{x}=0,\tilde{y}\right) \tag{79}$$

At the outlet, the flux of each species is set to its convective flux. The diffusive flux is set to zero. The outlet boundary condition for the current is the same as the inlet condition.

$$N_k\left(\tilde{x}=1,\tilde{y}\right)=C_k\left(\tilde{x}=1,\tilde{y}\right)v_x\left(\tilde{y}\right) \tag{80}$$

$$J\left(\tilde{x}=1,\tilde{y}\right)=\sum_{k} z_k N_k\left(\tilde{x}=1,\tilde{y}\right) \tag{81}$$

3.2.2.2 *Cathode boundary conditions imposed at y = 0*

The cathode is the bottom wall of the channel. At the cathode, the neutral quinone is reduced to form dianion adduct. Conservation of mass at the cathode interface implies that the flux of neutral quinone must be equal and opposite to the flux of dianion quinone. The inert ions do not participate in Faradaic reactions at either electrode, so their fluxes are zero at both electrodes.

$$N_{Q,\tilde{y}}\left(\tilde{x},\tilde{y}=0\right)=-N_{Q2,\tilde{y}}\left(\tilde{x},\tilde{y}=0\right) \tag{82}$$

$$N_{N,\tilde{y}}\left(\tilde{x},\tilde{y}=0\right)=0 \qquad N_{P,\tilde{y}}\left(\tilde{x},\tilde{y}=0\right)=0 \tag{83}$$

The cathode is porous, and exposed to the flue gas flowing through a graphite, gas-diffusion electrode. Pressure changes in the flue gas are neglected, and that implies a constant partial pressure of carbon dioxide in the flue gas. Mass transfer resistance in the gas phase is assumed negligible. Therefore the partial pressure of carbon dioxide at the cathode interface is constant and equal to the partial pressure in the flue gas. Dissolution kinetics are assumed fast, so the concentration of carbon dioxide at the cathode interface is equal to the local partial pressure divided by the Henry's law constant. Mass conservation at the interface requires that the net flux of carbon dioxide in to the electrolyte at the cathode boundary is the sum of the flux from the gas phase and the flux from absorption by the dianion adduct.

$$N_{\mathrm{CO}_2,\tilde{y}}\left(\tilde{x},\tilde{y}=0\right)=-\frac{D_{\mathrm{CO}_2}}{\Delta y}\left(C_{\mathrm{CO}_2}\left(y=0^{+}\right)-C^{*}_{P_c}\right)-2N_{Q2,\tilde{y}}\left(\tilde{x},\tilde{y}=0\right) \tag{84}$$

The flux of carbon dioxide is proportional to twice the flux of dianion adduct because the dianion absorbs two molecules of carbon dioxide per molecule of quinone. The term "C^{*}_{pc}" is a ghost point that is not exactly equal to the carbon dioxide concentration at the interface. In this method of finite volumes, a concentration is imposed at the interface by creating a "ghost point" (denoted by an asterisk). The ghost point is the concentration of carbon dioxide in an imaginary finite volumes box at the same x-position, but on the other side of the interface. The concentration at the cathode interface is the average of the ghost point and the nearest point in the channel, which is indicated by "$y = 0^{+}$". The average of these two concentrations is equal to the boundary concentration; that is, the average is equal to the partial pressure in the flue gas divided by the Henry's law constant for the electrolyte.

The boundary conditions for the dianion and ionic potential are coupled to each other and to local concentrations through a system of equations that describe the electron flux across the cathode interface. The potential drop across the interface ($\Delta\varphi_c$) is defined as the potential of the cathode (φ_c) minus the ionic potential in the electrolyte at the boundary ($\varphi(y=0)$). This potential drop determines the ionic potential at the boundary.

$$\Delta\phi_c = \phi_c - \phi(\tilde{y} = 0) \tag{85}$$

This potential drop is a function of the equilibrium potential difference and the activation overpotential. The equilibrium potential difference ($\Delta\varphi_c^{eq}$) is a function of the standard potential ($\Delta\varphi^0$) and the local concentrations according to the Nernst equation.

$$\Delta\phi_c^{eq} = \Delta\phi_c^0 + \frac{RT}{n_c F}\ln\left[\frac{\tilde{C}_Q(y=0)\tilde{C}_{CO_2}^2(y=0)}{\tilde{C}_{Q2}(y=0)}\right] \tag{86}$$

The activation overpotential (η_c) is equal to the electrode potential drop minus the equilibrium potential drop.

$$\eta_c = \Delta\phi_c - \Delta\phi_c^{eq} \tag{87}$$

The magnitude of the dianion adduct flux at the cathode is equal to the reaction rate. The reaction rate is coupled to the location concentrations, the exchange current density, and the activation overpotential through the Butler-Volmer expression (Equation (88)).

$$N_{Q2}(\tilde{y} = 0) = -j_c^0 (C_{Q2})^{\alpha} (C_Q C_{CO_2}^2)^{1-\alpha}\left[e^{n(1-\alpha)\eta_c} - e^{-n\alpha\eta_c}\right] \tag{88}$$

Combined, Equations (85) through (88) are a system of equations that determine the dianion flux and the ionic potentials at the cathode explicitly. Note that the cell potential is equal to the potential of the anode minus the potential of the cathode, and the cell potential is an operating parameter. In practice, the cathode is chosen as the grounded electrode, so its electric potential is always zero. The anode potential is set to the cell potential. Electric resistances external to the cell are neglected.

For this analysis, the reaction kinetics are assumed fast relative to the transport resistances. For the numerical simulations, the exchange current density is set to be a value that is high enough for kinetic overpotentials to be minimal.

3.2.2.3 Anode boundary conditions imposed at y = h

The anode is the top wall of the channel. At the anode, the dianion adduct is oxidized and the carbon dioxide is desorbed. Neutral quinone and carbon dioxide are "produced" at the anode. Conservation of mass at the anode interface implies that the flux of neutral quinone must be equal and opposite to the flux of dianion quinone. The inert ions do not participate in Faradaic reactions, so their fluxes are zero.

$$N_{Q,\tilde{y}}\left(\tilde{y}=1\right)=-N_{Q2,\tilde{y}}\left(\tilde{y}=1\right) \tag{89}$$

$$N_{N,\tilde{y}}\left(\tilde{y}=1\right)=0 \qquad N_{P,\tilde{y}}\left(\tilde{y}=1\right)=0 \tag{90}$$

The anode is a solid, nonporous electrode. Mass conservation at the interface requires that the net flux of carbon dioxide must be proportional to twice the flux of dianion adduct.

$$N_{\mathrm{CO}_2,\tilde{y}}\left(\tilde{y}=1\right)=-2N_{Q2,\tilde{y}}\left(\tilde{y}=1\right) \tag{91}$$

The boundary conditions for the dianion adduct and the ionic potential are coupled to each other and to local concentrations through a system of equations analogous to those presented in Section 3.2.2.2. This system of equations includes an equation for the potential drop across the interface ($\Delta\varphi_a$), the equilibrium potential drop ($\Delta\varphi_a^{eq}$), and the activation overpotential (η_a).

$$\Delta\phi_a=\phi_a-\phi\left(\tilde{y}=1\right) \tag{92}$$

$$\Delta\phi_a^{eq}=\Delta\phi_a^0+\frac{RT}{n_aF}\ln\left[\frac{\tilde{C}_Q\left(y=1\right)\tilde{C}_{CO_2}^2\left(y=1\right)}{\tilde{C}_{Q2}\left(y=1\right)}\right] \tag{93}$$

$$\eta_a=\Delta\phi_a-\Delta\phi_a^{eq} \tag{94}$$

The magnitude of the dianion quinone flux at the anode is equal to the Faradaic reaction rate, which is described by the Butler-Volmer equation.

$$N_{Q2}\left(\tilde{y}=1\right)=j_a^0\left(C_{Q2}\right)^{\alpha}\left(C_QC_{CO_2}^2\right)^{1-\alpha}\left[e^{n(1-\alpha)\eta_a}-e^{-n\alpha\eta_a}\right] \tag{95}$$

As mentioned in Section 3.2.2.2, the cathode is chosen as the grounded electrode, so its electric potential is always zero. The anode potential is set to the cell potential. Electric resistances external to the cell are neglected. All reaction kinetics are assumed fast relative to the transport resistances, so the exchange current density is set to be a value that is high enough for kinetic overpotentials to be minimal.

3.2.3 Results and discussion

The numerical simulation of the system solves the equations described in Sections 3.2.1 and 3.2.2, and it is written in Python. The code uses “NumPy” and “DAE Tools”. NumPy is an extension that allows for computation using large, multidimensional arrays and useful mathematical functions [73]. DAE Tools is a software package that was used for solving simultaneously the system of nonlinear differential equations [74]. For this work, the simulations were performed under conditions of constant cell potential, and the solutions to the governing equations produce a quantitative current as a result. Mathematically, it is equally valid to integrate the equations under conditions of constant current to produce a quantitative cell potential.

The numerical simulation solves for the ionic potential and the species concentrations in the two-dimensional space of the flow channel. Also, the simulation produces a set of values for current, potential, and carbon dioxide flux. These numbers are important in the context of the larger system for carbon capture, which includes two flash tanks and two pumps. For this system, the two key performance metrics are energy cost per unit carbon dioxide, and carbon capture rate per unit depth. After discussion of a specific set of results from the numerical model, certain design parameters are evaluated for their impact on these performance metrics.

3.2.3.1 Analysis of concentration and flux profiles for a single set of parameters

Table 2 contains the simulation parameters and their nominal values for numerical modeling of the quinone-dianion system.

Table 2 Simulation parameters and values for quinone-dianion system

Name	Symbol	Value
(Time stamp 154216)		
Length	L	0.05 m
Height	h	0.01 m
Boxes, x-direction	n_x	35
Boxes, y-direction	n_y	35
Diffusivity, neutral quinone	D_Q	7×10^{-10} m^2/s [75]
Diffusivity, dianion quinone	D_{Q2-}	7×10^{-10} m^2/s
Diffusivity, inert cation	D_P	1×10^{-9} m^2/s (estimated)
Diffusivity, inert anion	D_N	1×10^{-9} m^2/s (estimated)
Diffusivity, CO_2 in DMSO	D_{CO2}	5×10^{-9} m^2/s [69]
Diffusivity, CO_2 in gas phase	$D_{CO2,g}$	$1.69\ 10^{-5}$ m^2/s [68]
Cell voltage	V	0.25 Volts
Average fluid velocity	U = Uavg	7E-4 m/s
Concentration, quinone, bulk	$C_Q{}^0$	0.1 M
Concentration, dianion, bulk	$C_{Q2}{}^0$	0.1 M
Concentration, inert anion, bulk	$C_N{}^0$	0.2 M
Concentration, inert cation, bulk	$C_P{}^0$	0.4 M
CO2 saturation electrolyte	λ	0.2 bar
Total pressure	P	1 bar
Partial pressure CO_2 in flue gas	p_c	0.15 bar
Henry's law constant, CO_2 in DMSO, 20°C	H	17.54 bar/M [76, 77, 78, 79, 80]
Standard potential, cathode reaction	$\Delta\varphi_c{}^0$	0
Standard potential, anode reaction	$\Delta\varphi_a{}^0$	0
Exchange current density, cathode	$j_c{}^0$	1×10^8 A/m^2
Exchange current density, anode	$j_a{}^0$	1×10^8 A/m^2
Alpha, Butler-Volmer, cathode	α_c	0.5
Alpha, Butler-Volmer, anode	α_a	0.5
Charge, inert cation	z_P	+1
Charge, inert anion	z_N	-1
Temperature	T, Tref	298 K (25°C)
	Dref	DQ
	Cref	1 M
	Nref	1000*cref*Dref/Lref
	Lref	Ly
	Jref	E*Navo/Nref
	Currref	Jref*Lref

The numerical simulation solves for the ionic potential and the species concentrations in the space of the flow channel under the conditions listed in Table 2. For clarity, the concentration maps are presented as dimensionless concentrations. The quinone and dianion adduct concentrations are scaled to their bulk, inlet concentrations (C^0). The CO_2 concentration is scaled to its solubility limit in the electrolyte. This means that the system is supersaturated when the dimensionless CO_2 concentration (Λ) is greater than one.

$$\Omega = \frac{C_{Q(CO_2)_2^{2-}}}{C^0_{Q(CO_2)_2^{2-}}} \qquad \Upsilon = \frac{C_Q}{C_Q^0} \qquad \Lambda = \frac{C_{CO_2}}{C_{CO_2}^0} \qquad (96)$$

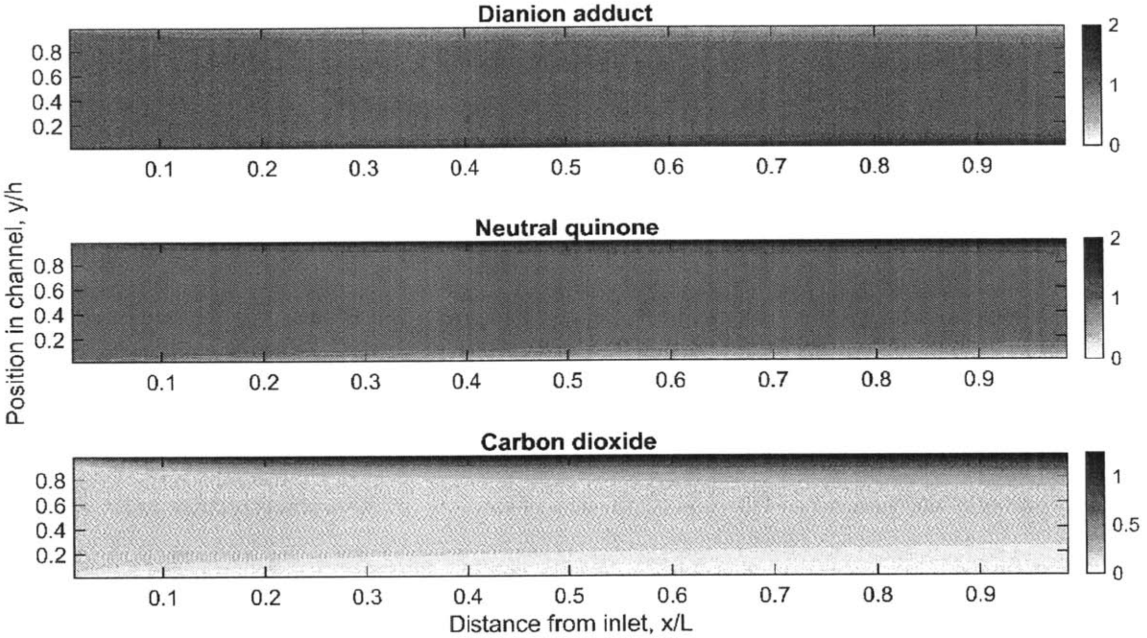

Figure 3.5 Dimensionless concentration at every position in the flow channel. The dianion adduct and neutral quinone concentrations are scaled to their bulk, inlet concentrations. The CO_2 concentration is scaled to the solubility limit. The operation parameters that produce these results are listed in Table 2.

Figure 3.5 contains the two-dimensional, dimensionless concentration profiles for dianion adduct, neutral quinone, and carbon dioxide. The color bars are set so that higher concentrations appear darker, and lower concentrations are lighter. The aspect ratios of the figures match the aspect ratio of the system itself. As expected, the gradients in concentration are confined to thin boundary layers near the electrode. The carbon dioxide boundary layer is thicker than either quinone layer because the diffusion coefficient for dissolved CO_2 is higher than that of either quinone.

There is enrichment of the dianion adduct in the boundary layer near the cathode (bottom), and depletion at the anode. The opposite is true for the neutral quinone. For these specific simulation parameters, the concentrations of dianion and neutral quinone approach zero (white) near the anode and cathode, respectively. The system is nearing limiting current when the concentration of a reactive species nears zero at the surface. Because the reactions are the same at both electrodes, the quinone approaches a dimensionless concentration of two in the enrichment layer at the same time it approaches zero as it depletes.

Note that in the plot for carbon dioxide, the dimensionless concentration is greater than unity near the anode. Recall that the CO_2 concentration is scaled to its solubility limit, rather than its bulk concentration. The local concentration of CO_2 in the electrolyte is higher than its solubility limit anywhere the dimensionless concentration is greater than one. One should expect bubble formation anywhere that the concentration is higher than the solubility limit. The nucleation and growth of bubbles depends on the degree of supersaturation, and the viscosity of the fluid. In Figure 3.5, it is clear that the rate of oxidation and desorption is fast enough to supersaturate the electrolyte under these conditions.

The carbon dioxide flux in the electrolyte at the cathode surface is the net flux that balances the rate of absorption by the quinone and the rate of physical absorption (or desorption) relative to the adjacent gas phase. Diffusion in the gas phase is assumed to be significantly faster than diffusion in the liquid phase. This assumption is justified by the fact that the diffusion coefficient is estimated to be at least three orders of magnitude higher in the gas phase (Table 2, [68, 69]). Physically, this implies that it is never possible to deplete the carbon dioxide at the electrolyte surface faster than it can be replaced from the gas phase. Therefore, the flux at the cathode is determined by two parallel processes: absorption by the dianion, and physical dissolution. The partial pressure of the CO_2 dissolved in the electrolyte (λ) relative to the partial pressure in the gas phase (p_c) determines the rate and direction of physical absorption/desorption. In this particular simulation, the partial pressure of CO_2 in the electrolyte is 0.2 bar, while the flue gas has 0.15 bar partial pressure. Since the electrolyte has a greater CO_2 partial pressure, there is some diffusive flux of carbon dioxide toward the gas phase. As long as the rate of absorption by the quinone is greater than the rate of diffusion, then the system will achieve net absorption of carbon dioxide.

Chemical absorption of carbon dioxide via quinone occurs at the cathode surface. The rate of chemical absorption by the quinone relative to the rate of physical absorption (or desorption) by the electrolyte determines the net flux of carbon dioxide of the electrochemical cell. Figure 3.6 shows the *net* molar flux of carbon dioxide and the net molar flux of electrons (the current) at the cathode surface as functions of position along the channel.

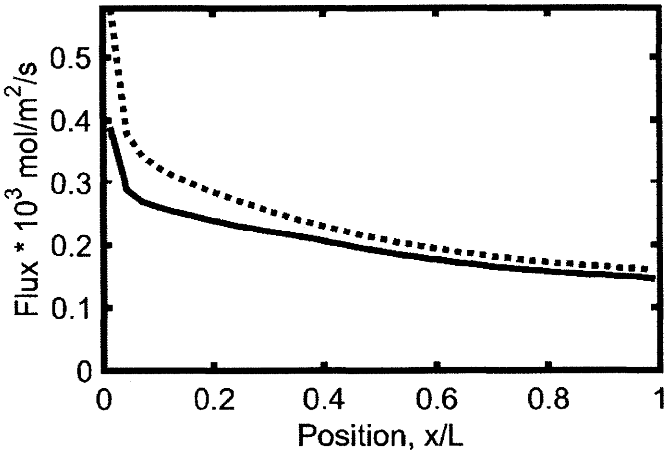

Figure 3.6 Net flux of carbon dioxide (solid line) and electrons (dashed line) as functions of position along the cathode. The operating conditions are those listed in Table 2. The ordinate has units of Flux x 10^3 mole/m^2/s.

The net flux of carbon dioxide is the solid line in Figure 3.6. The fact that the flux is positive along the entire channel length means that the rate of absorption by quinone is significantly higher than the rate of physical desorption from the electrolyte for this set of operating conditions (Table 2).

The concept of current efficiency refers to the amount of carbon dioxide captured relative to the amount of electrons transferred to perform that capture. The distance between the lines in Figure 3.6 indicates the degree of current efficiency. Physically, the difference occurs because there is some flux of carbon dioxide based on physical solubility and local concentrations. The closer the two lines are to each other, the more efficient the system. The best possible scenario is one in which the rate of electron transfer to carbon capture is 1:1. It is also possible to operate under conditions where the ratio is less than 1:1 (meaning less than 1 mol electrons per 1 mol CO_2 captured). In practice, the design must balance current efficiency and energy efficiency. If the energy cost of operating at a better current efficiency is too high, the energy efficiency will suffer.

The electron flux at the electrode is equal to the current at that position. Figure 3.7 is a plot of the current density as a function of position along the electrode.

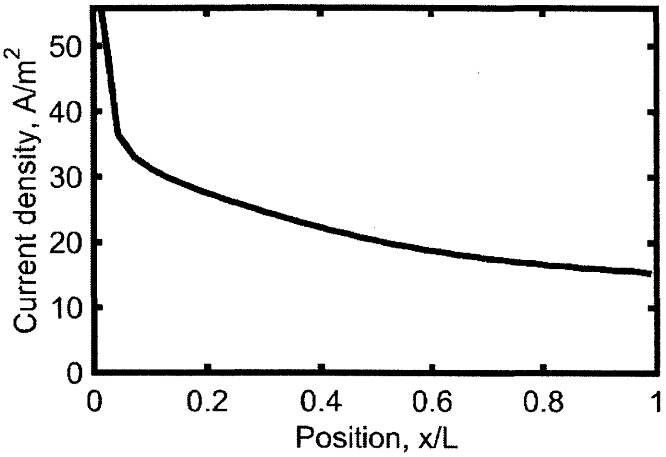

Figure 3.7 Current density, A/m^2, as a function of position along the cathode.

The shape of the curve in Figure 3.7 is typical of systems that involve laminar flow past a flat, reactive boundary, and it mirrors the shape of the boundary layers shown in Figure 3.5. The flux is highest near the entrance because the boundary layers are thinnest there. Moving in to the cell, the boundary layer thickness increases according to the square root of position. This functional form is important to cell design. Making the cell longer in the flow direction will increase the total current. At the same time, the marginal increase is less than one because the boundary layer continues to get thicker and the flux continues to drop as the cell gets longer.

3.2.3.2 Analysis of stream break

The results in Section 0 show that it is possible to achieve a region that is supersaturated in carbon dioxide. One can isolate this region for downstream treatment by splitting the electrolyte fluid stream at the channel outlet (see process flow diagram in Figure 3.3). Some carbon dioxide is collected at the first flash tank at 1 bar total pressure. The rest is collected at the second flash tank using a vacuum pump to provide an evaporative driving force. Optimal position of the stream break is the one that maximizes the relative amount of carbon dioxide captured at the first flash tank. Figure 3.8 shows the amount of CO_2 captured in the first flash tank, as a percent of total CO_2 captured, as a function of the position of the stream break.

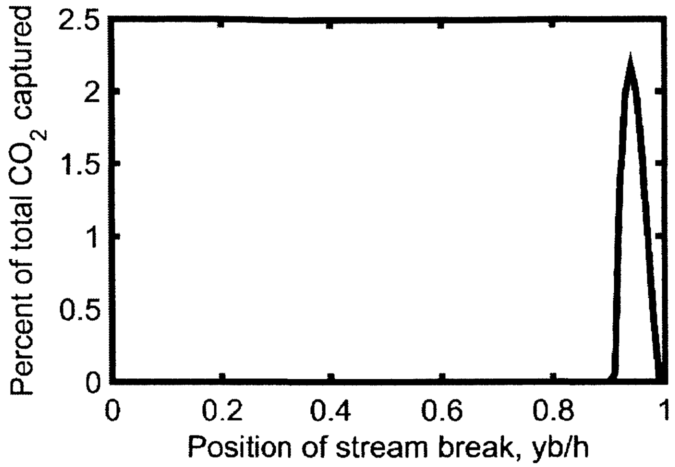

Figure 3.8 Percent of all CO_2 captured that is captured at the flash tank at 1 bar total pressure. The x-axis is the position of the stream break relative to the channel height (zero is the cathode, 1 is the anode).

The percentage of carbon captured at the first flash tank peaks at a position near the anode surface. To the right of this peak, the relative amount drops because some supersaturated fluid is "wasted" when it mixes with the sub-saturated fluid and goes to the vacuum flash. To the left of this peak, the relative amount drops because some sub-saturated fluid mixes with the supersaturated fluid so that some excess carbon dioxide dissolves in the fluid rather than evaporating in the first flash tank. The percentage of CO_2 is highest at the height at which the electrolyte is exactly saturated. Figure 3.9 shows the dimensionless CO_2 concentration as a function of position at the channel outlet.

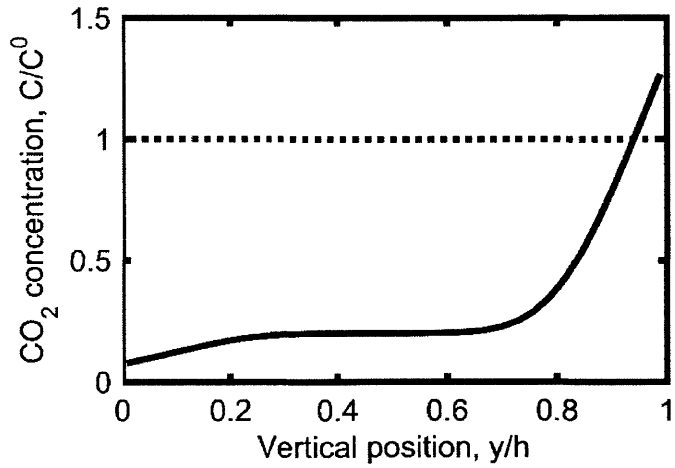

Figure 3.9 Dimensionless concentration profile for carbon dioxide leaving the channel. The concentration is scaled to C^0, the solubility limit for these conditions. The dashed line is placed at a value of one to show the location of CO_2 concentrations equal to one.

Taken together, Figure 3.8 and Figure 3.9 prove that the optimal position for the stream break is the height at which the electrolyte is exactly saturated. For the rest of this analysis, the stream break is always placed at this position.

3.2.3.3 Calculating total energy of capture

There are three major components in the calculation of total energy required to capture carbon dioxide in the quinone-dianion system:

(1) The electric work (power)

(2) The shaft work of the pump that re-compresses the electrolyte after the vacuum flash tank

(3) The shaft work of the vacuum pump that evacuates the vacuum flash tank and compresses the carbon dioxide that evaporates.

The electric power, $\dot{W}_{elec}$, is simply the product of the current (I) and the cell voltage (V). The current is reported as Amps per unit channel depth, and the power is reported as power per unit channel depth.

$$\dot{W}_{elec} = IV \tag{97}$$

One of the pumps re-compresses the electrolyte from the total pressure of the vacuum flash (λ) to the total pressure of the channel (1 bar, atmospheric). The electrolyte is assumed incompressible under these conditions. Therefore, the fluid density is constant and independent of pressure. Any temperature changes in the pumped fluid are assumed to be negligible. It is also assumed the fluid properties are insensitive to temperature and pressure changes. The shaft work is calculated by calculating the isentropic work of pumping, $\dot{W}_{s,pumping}^{isentropic}$, and then correcting for the pump efficiency.

$$\dot{W}_{s,pumping}^{isentropic} = \dot{V}\Delta P = \left(Uh\right)\left(P - \lambda\right) \tag{98}$$

The term $\dot{V}$ is the volumetric flow rate of the fluid, and ΔP is the discharge pressure (P, 1 bar absolute) minus the suction pressure (λ, bar). The actual shaft work, $\dot{W}_{s,pumping}$, is equal to the rate of isentropic work divided by the efficiency of the pump (η). For this analysis, the liquid pump efficiency is assumed to be 0.75.

$$\dot{W}_{s,pumping} = \frac{\dot{W}_{s,pumping}^{isentropic}}{\eta} \tag{99}$$

The second pump calculation is for the vacuum pump to evacuate the flash tank down to its operating pressure of lamda (λ, bar). The pump compresses the carbon dioxide that evaporates to a total pressure of 1 bar.

The shaft work for the vacuum pump is based on the isentropic work of compressing an ideal gas, $\dot{W}_{s,vacuum}^{isentropic,IG}$, and corrected by the pump efficiency (η_{vac}). The equation below is the calculation of work required to perform isentropic compression of an ideal gas.

$$\dot{W}_{s,vacuum}^{isentropic,IG} = \dot{n}\frac{\gamma RT}{\gamma - 1}\left[\left(\frac{P}{\lambda}\right)^{\frac{\gamma-1}{\gamma}} - 1\right] \tag{100}$$

$$\gamma = \frac{C_P}{C_V} \tag{101}$$

The term $\dot{n}$ is the molar flowrate of gas through the vacuum pump, R is the universal gas constant, and T is the temperature (K). The term γ is the ratio of the constant pressure heat capacity (C_P) to the constant volume heat capacity (C_V) (Equation (101)). The value of γ for CO_2 and other simple polyatomic gases is approximately 1.3 [81].

Isentropic efficiencies for vacuum pumps (η_{vac}) are approximately 0.4 to 0.55 when the suction pressure is in the range of 40 torr (0.053 bar) to 150 torr (0.2 bar) [82]. For this work, the calculations were performed for several values in this range. In general, the pump efficiency did not affect the design concepts, even though it certainly affected the quantitative value. For brevity, only the results for the most efficient vacuum pump (value of 0.55) are reported in most cases.

3.2.3.4 Design analysis of stream break, cell potential, saturation, and channel height

The current, cell potential, and rate of absorption are determined using the numerical model. The rate of power and shaft work for the two pumps is calculated using the equations in Section 3.2.3.3. Together, these results describe the performance of the quinone-dianion system with a given set of operating parameters. What follows is an exploration of a subset of those parameters and their impact on the energy cost of capture.

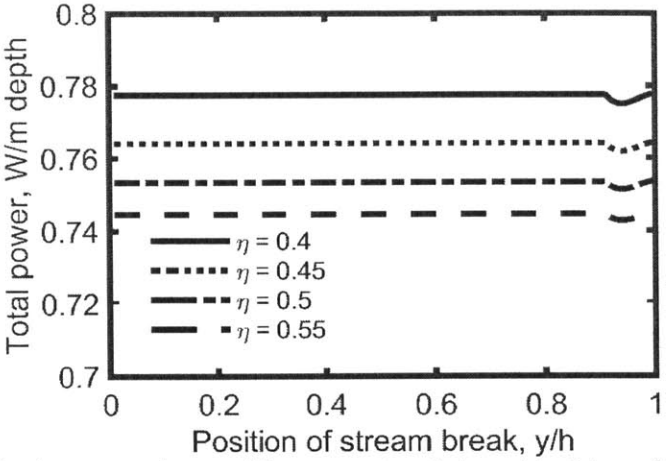

Figure 3.10 Total power requirement (Watts per meter of channel depth) as a function of the position of the stream break (relative to the total channel height) for four different vacuum pump efficiencies.

Figure 3.10 shows the total power consumption of the system as a function of the position of the stream break. Each line represents a different value of the vacuum pump efficiency. The results show the impact of the stream break position and the vacuum pump efficiency relative to the total power consumption. For all four efficiencies tested, the effect of the stream break optimization is small but significant. The position of the stream break determines the relative amounts of carbon dioxide that are collected at the first flash tank (negligible energy cost by itself) and the vacuum pump. Equation (100) shows that the shaft work of the vacuum pump is proportional to the amount of carbon dioxide pumped, which changes with the position of the stream break. The change in the molar flow rate of CO_2 to the vacuum pump is relatively small compared to the total value, which is also small.

The efficiency of the vacuum pump is expected to be in the range of 0.4 to 0.55. The total power is approximately 0.745 W/m for the most efficient pump and 0.775 W/m for the least efficient vacuum pump. Therefore, the difference in power requirement is estimated to be approximately 4% of the total energy requirement.

Regarding design parameters, the results so far show the impact of channel length, stream split position, and vacuum pump efficiency on the overall performance of the cell. The impact of the cell potential (V) is interesting and not obvious. The "I-V" curve for this system is similar to that of any other diffusion-limited cell, and has the same shape as the planar membrane curve (Figure 2.2). At low values, the current increases linearly with potential. When the potential is high enough that current is near the limiting current, the marginal increase in current as a function of potential approaches zero. Holding everything else constant, CO_2 capture increases with increasing current. The energy cost also increases with increasing current and potential. Figure 3.11 shows the total energy cost per mole of carbon dioxide as a function of the cell potential.

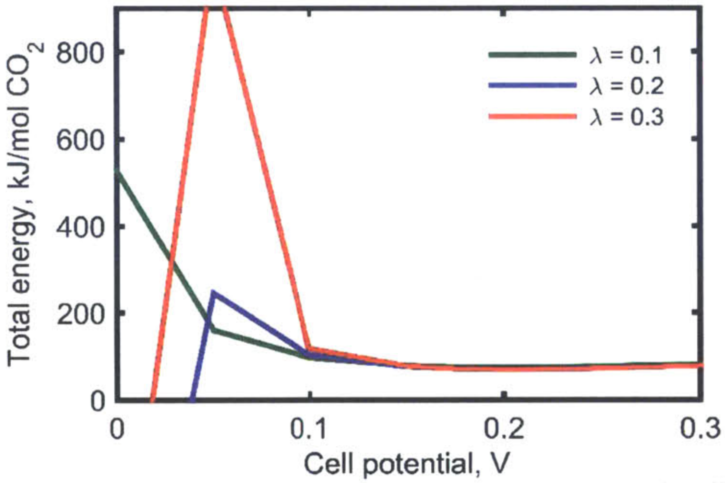

Figure 3.11 Total energy requirement, kJ/mol CO_2 captured, as a function of applied cell potential for an inlet CO_2 partial pressure (λ) ranging from 0.1 to 0.3 bar.

The relationship between energy and cell potential (Figure 3.11) has some interesting features. First, the energy cost spikes at low potentials. At low voltage, the current is very low, which means the rate of CO_2 absorption by the quinone is also low. At the same time, the rate of physical absorption (or desorption) is unaffected by cell potential. As a result, at low potential (and current), the net rate of carbon capture via chemical absorption approaches zero, which means the energy per unit CO_2 increases exponentially. When the CO_2 in the electrolyte is high enough (red curve, λ=0.3 bar CO_2 partial pressure), the rate of physical desorption is so high that if one were to operate at low current, the net rate of carbon capture would be negative.

Moving along the x-axis in the direction of increasing potential, there is a clear drop in the energy cost of capture from a cell potential of 0.5 V to 1.5 V. This region is consistent with the region in which the current increases as a roughly linear function of potential. Figure 3.12 contains the same data as the previous figure. To show more clearly the behavior at higher potentials and lower total energy, the y-axis only includes values between 0 and 150 kJ/mol CO_2.

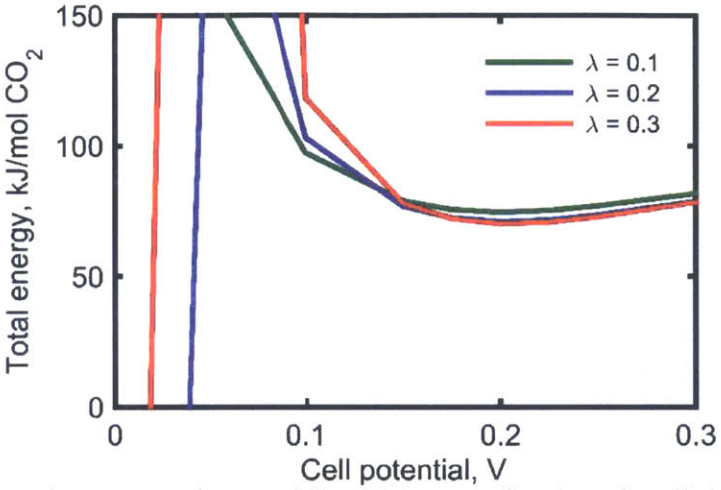

Figure 3.12 Total energy requirement, kJ/mol CO_2, as a function of applied cell potential for an inlet saturation pressure (λ) ranging from 0.1 to 0.3 bar. The ordinate is limited to the range of 0-150 kJ/mol CO_2.

Closer examination of Figure 3.12 reveals that the local minimum value of total energy cost occurs at a cell potential of approximately 0.2 V. The location of the minimum cell potential corresponds to the location of the inflection point in the *I-V* curve. At potentials higher than 0.2 V, the marginal increase in energy is greater than the marginal increase in current, so the overall energy efficiency goes down.

Table 3 shows that the minimum energy values occur at approximately the same cell potential, regardless of the inlet saturation. The fact that the minimum value occurs at the same cell potential, regardless of CO_2 partial pressure, is explained by the fact that the current at a given potential is unaffected by CO_2 concentration (unless that concentration is very close to zero). Note that the partial pressure of carbon dioxide in the cathode is 0.15 bar for all of these simulations. This means that the cell potential that minimizes the energy cost per mol CO_2 is unaffected by the current efficiency within the range of 0.1 to 0.3 bar.

Table 3 Select values from data describing total energy requirement as a function of cell potential (from Figure 3.12).

Inlet saturation, λ, bar	0.1	0.2	0.3
Cell potential, V	0.2	0.2	0.2
Carbon capture rate, moles/m/s	1.03×10^{-5}	9.37×10^{-6}	8.41×10^{-6}
Total power requirement, W/m	0.768	0.665	0.590
Current, A/m	-1.05	-1.06	-1.07
Electric power (IV), W/m	0.209	0.212	0.214
Shaft work, liquid pump, W/m	0.420	0.373	0.327
Shaft work, vacuum pump, W/m	0.139	0.0801	0.0496

It is interesting to note that for liquid partial pressures in the range of 0.1 to 0.3 bar, the *total* energy requirement decreases as a result of increasing CO_2 concentration. This result is counterintuitive because the net CO_2 flux decreases in response to increasing CO_2 concentration and therefore the current efficiency decreases with increasing CO_2 concentration.

Table 3 includes the rate of carbon capture, the current, and the values for individual energy inputs at a cell potential of 0.2V and CO_2 partial pressures of 0.1, 0.2, and 0.3 bar. The reason the *total* energy decreases as the inlet concentration increases is because the largest contributor to the energy is the energy to re-pressurize the electrolyte after the vacuum flash tank. This energy term is directly proportional to the total pressure of the vacuum flash tank, which is equal to the CO_2 partial pressure in the electrolyte. The decrease in the pump work is greater than the decrease in the rate of carbon capture, and the other energy inputs are relatively unchanged. Together, the system operates more energy efficiently at higher inlet concentrations, within this range.

Figure 3.13 shows the total and individual energy requirements as functions of cell potential, holding all other parameters constant. The concentration of carbon dioxide in the electrolyte is in equilibrium with a partial pressure of 0.2 bar ($\lambda = 0.2$ bar). At all cell potentials, the largest contributor to the total energy is the energy required to power the liquid recompression. As the cell potential increases, the electric energy cost per mol CO_2 increases and the liquid pump value decreases. The volume of fluid moving through the liquid pump is mostly unaffected by the current. Increasing current increases the region of supersaturation, which increases the volume of the supersaturated stream relative to the volume that goes from the cell to the vacuum flash tank. However, the magnitude of that effect is relatively small to the total liquid volume, so changes in it don't affect the shaft work required to pump the liquid very much. Instead, the energy cost per mol CO_2 of the liquid pump drops dramatically because the rate of carbon capture increases dramatically in this range, so the pumping energy is being divided by a larger and larger denominator.

The results in Figure 3.13 provide another explanation for increasing energy efficiency as a function of increasing cell potential. The electric energy per mol CO_2 (dashed line) increases with increasing cell potential. If this were the only energy requirement of the system, then optimal operation would require minimizing the cell potential. However, the shaft work to pump the liquid is another, and larger, energy requirement of the system. The energy cost of pressurizing the liquid decreases with increasing cell potential because the rate of carbon capture is increasing. Therefore, the dominant contribution of the liquid pump drives the overall energy efficiency downward.

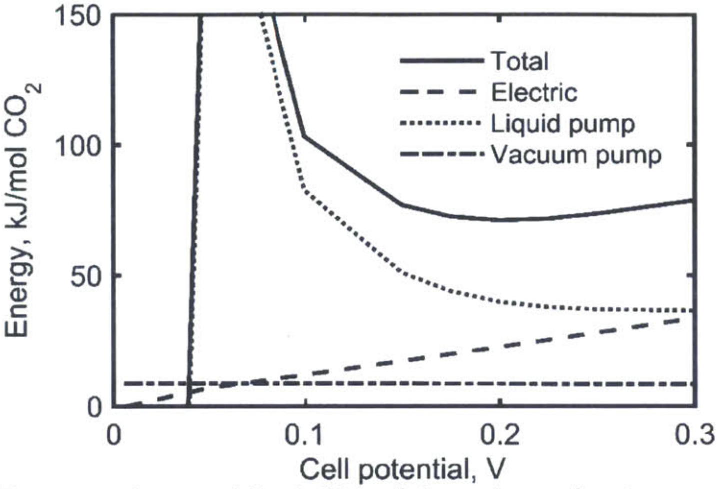

Figure 3.13 Energy requirement, kJ/mol CO_2, of the major equipment components of the system. All operating conditions are listed in Table 2, except the applied potential varies from 0 to 0.3 V, and the adiabatic efficiency for the vacuum pump is assumed to be 0.55. The inlet saturation is 0.2 bar.

While energy efficiency is an important performance metric, the rate of carbon capture per unit depth determines the size of the equipment in the system. Therefore, the carbon flux serves as a proxy for capital cost. It is important to balance energy efficiency with flux in order to optimize the overall cost of carbon capture. Figure 3.14 shows the rate of carbon capture, in kilograms per hour per meter depth, as a function of cell potential and CO_2 partial pressure in the liquid (λ).

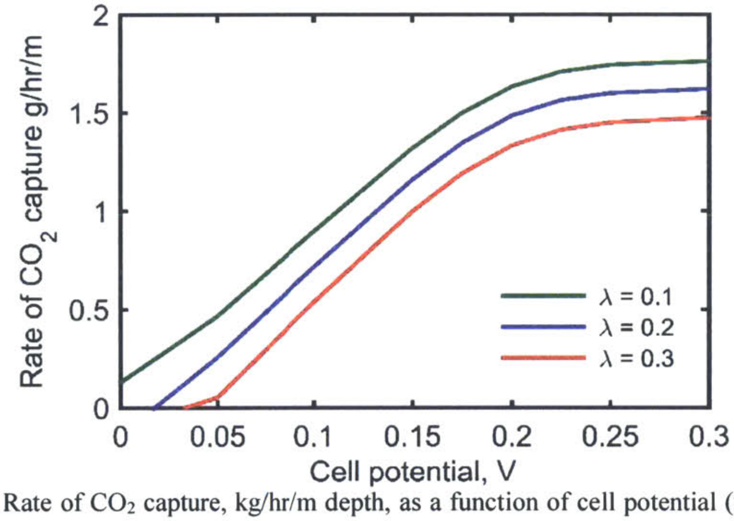

Figure 3.14 Rate of CO_2 capture, kg/hr/m depth, as a function of cell potential (x-axis) and inlet saturation (line color).

The rate of carbon capture is a strong function of cell potential because it is a strong function of current. The inflection point at approximately 0.2 V is in alignment with the results for energy efficiency as a function of cell potential. The quantities in

Table 3 show that the change in the rate of carbon capture at fixed potential is linear with respect to changes in the inlet CO_2 partial pressure. When the inlet saturation increases by 0.1 bar, the rate of carbon capture decreases by 1×10^{-6} mol/m/s. In terms of optimization, this model is useful because it allows for quantifying the relative changes in energy cost and capital costs as functions of inlet saturation and cell potential, among other parameters.

Changing the height of the channel changes the energy and mass transfer profiles of the system. Since mass transfer is confined to a thin boundary layer near the electrode, the bulk of the fluid in the electrolyte does not participate in carbon capture. At the same time, the ohmic losses are proportional to concentration and distance. In the bulk of the fluid, the concentrations are constant. Therefore, within a certain range, decreasing the channel height should decrease the energy cost in two ways: (1) it reduces the ohmic losses at constant concentration, and (2) it reduces the total amount of fluid that needs to be pumped, and therefore reduces the pumping energy requirements. Figure 3.15 contains data for the energy penalty, in units of kJ/mol CO_2, as a function of channel height.

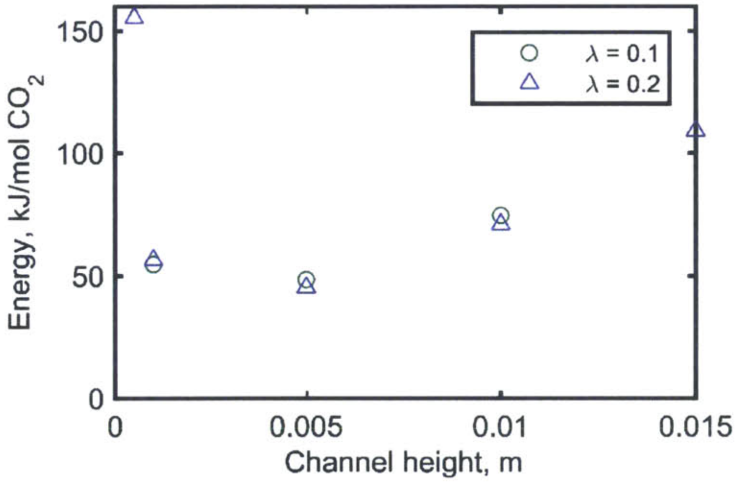

Figure 3.15 Energy cost, kJ/mol CO_2 as a function of channel height (m). Values are shown for 0.1 bar (circle) and 0.2 bar (triangle) CO_2 partial pressures.

The data indicate the range of channel heights that minimize the energy cost per mole CO_2 holding all other parameters constant. For these operating parameters, a channel height of 5 mm minimizes the energy cost per mole CO_2. Channel heights less than 5 mm are inefficient because the boundary layers begin to touch or cross each other. Specifically, for channel heights less than 5 mm, the carbon dioxide desorbed at the anode diffuses across the channel and reduces the carbon dioxide flux at the cathode. As a result, the net amount of carbon captured decreases, and the energy efficiency decreases. On the other hand, channel heights greater than 5 mm are less efficient because the space is filled by bulk fluid that leads to greater ohmic losses and greater pumping costs. Note that the channel height of 5 mm is necessarily sensitive to the channel length because the maximum boundary layer thickness is a function of channel length. For shorter channels, the maximum boundary layer thickness is lower (at the same flow rate), so the channel height can be shorter. Also, as the channels get shorter, the concept of frictional losses to the electrolyte must be addressed. This will require higher pressures to force the electrolyte through the channel, and therefore increase the overall energy cost.

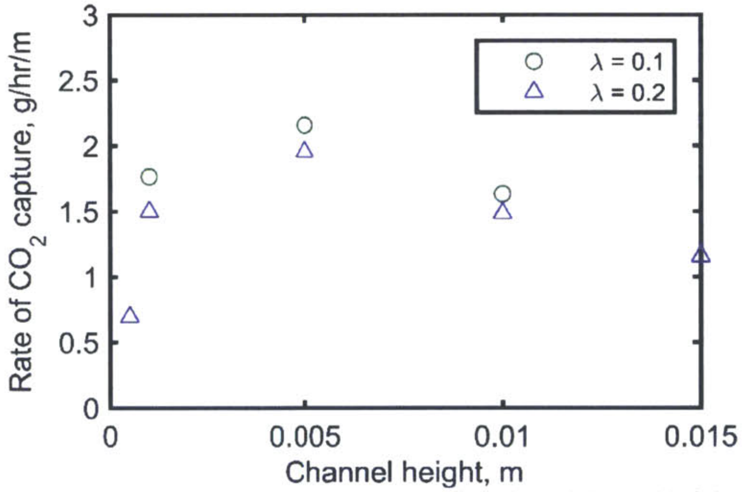

Figure 3.16 Rate of carbon capture, kg/hr/m depth, as a function of channel height. Values are shown for 0.1 bar (circle) and 0.2 bar (triangle) CO_2 partial pressures. Cell potential is 0.2 V.

Changing the channel height affects the rate of carbon capture in addition to the energy cost per mol CO_2. In Figure 3.16, the rate of carbon capture is plotted as a function of channel height. The current through the cell increases monotonically with decreasing channel height at constant potential. Current increases steadily because a smaller channel height reduces the ohmic losses. When potential is fixed, lower ohmic potential drops can be balanced with greater concentration polarization, and therefore greater current. Also, the rate of carbon capture increases with decreasing channel height, but only down to 5 mm. Channels thinner than 5 mm capture less carbon dioxide because the overlap of the CO_2 boundary layers reduces the net capture rate of the system.

3.2.4 Conclusions from numerical simulation and design analysis of quinone-dianion system

The design for a novel system of continuous carbon capture using a quinone as an electrochemical sorbent is introduced. Specifically, the quinone-dianion reaction occurs symmetrically at two electrodes, one porous and one solid. During operation, carbon dioxide is absorbed at the porous cathode and desorbed at the solid anode. In this design, it is possible to have regions near the anode where the electrolyte is supersaturated in carbon dioxide. As a result, a complete carbon capture system should have two flash tanks at different pressures to desorb and collect the carbon dioxide. The electrochemical cell and one flash tank should operate at atmospheric pressure. The second flash tank is a vacuum flash, where any remaining carbon dioxide is collected via vacuum pump and the electrolyte is regenerated.

Evaluation of the "quinone-dianion" system as a carbon capture technology requires quantification of the energy and carbon capture rate as functions of operating parameters. A numerical simulation was developed that calculates the concentrations of all species, and the resulting current and ionic potential. All of those variables are coupled to each other. The assumptions, governing equations, and boundary conditions for this model are described, and results for a typical simulation are presented and discussed. The numerical model provides reliable quantification of the electric energy demand and rate of carbon capture of the electrochemical cell. The design analysis was completed by quantifying the additional energy demand of the two pumps that make up the two other major system components.

The performance metrics for this system are the energy cost per mole carbon dioxide, and the overall rate of carbon capture (which acts as a proxy for capital cost). The design analysis shows clearly that the position of the stream break has a relatively small impact on the overall performance of the cell. The efficiency of the vacuum pump has a small, but significant and predictable impact on the overall system performance. Assuming no significant cost differential between less and more efficient vacuum pumps, the more efficient pump makes for a more efficient system of carbon capture.

The design impacts of the cell potential and the CO_2 bulk concentration are significant and surprising. Results show clearly that there is a cell potential that optimizes the energy cost per mole carbon dioxide. While electric energy demand increases monotonically with increasing cell potential, the rate of carbon capture increases exponentially as a function of this parameter. The impact of the carbon capture rate is greater than the increase in electric power demand, so the overall energy requirement decreases with increasing cell potential. The carbon capture rate increases monotonically with increasing cell potential, so one can expect the size of the system to have a comparable behavior.

Within the range of 0.1 to 0.3 bar, increasing the electrolyte saturation tends to decrease the overall energy requirement. While the increased electrolyte saturation tends to decrease the current efficiency, it reduces the pumping demand by a much greater margin, which makes the entire system more energy efficient. At the same time, the saturation parameter must be chosen to balance consideration for equipment size and capital cost.

Optimization of cell performance can be facilitated by optimization of the channel height. Under the conditions simulated in this work, the channel height that minimizes energy cost also maximizes carbon capture (both at fixed cell potential).

Future work in this area should focus on the impact of sorbent and electrolyte concentration first, and on the impact of optimal chemistry in general. The rate of carbon capture is a strong function of current, and the current is a strong function of the dianion concentration. The current at the electrode is carried entirely by the dianion adduct because that is the only species that is charged and that participates in Faradaic reactions. By inspection, one would expect that the optimal concentration is the highest possible quinone concentration that does not break the solubility limit at a given temperature. However, it is important to account for the supporting electrolyte, and its effect on the ohmic losses. The relative changes in ohmic losses and overall cell performance as functions of the relative and absolute amounts of the ionic species will determine the overall performance along this axis.

Future work should also investigate the performance and properties of the system at elevated temperature. Increasing the temperature will have several competing effects on the cell performance, and the design analysis can tease out the dominant behaviors. Increasing the operating temperature will increase the cell potential and the shaft work of the vacuum pump. For those reasons, increasing temperature reduces energy efficiency. At the same time, increasing the operating temperature should increase the diffusivities and solubilities of the quinones and the electrolyte, which will increase current and carbon capture rate. It will also reduce the overall viscosity, which should reduce frictional losses along the channel. Increasing temperature should also decrease the solubilities of the gaseous species. Reducing the gas permeabilities (up to a point), should enhance performance by increasing current efficiency and making it easier to supersaturate the electrolyte.

To conclude, this model provides some valuable information for designing a system for carbon capture, and fertile ground for future work.

4 Quinone-ferrocene as a reversible redox couple for CO_2 capture

4.1 Motivation for and description of new chemistry

Demonstration of CO_2 capture in any of these cell designs requires a mixture of the two central electroactive molecules. Experiments with cells designed for the quinone-dianion redox couple require the creation of an electrolyte mixture containing the neutral quinone and its dianion counterpart. In this work, 9,10-phenanthrenequinone (PQ) was typically the first choice for experiments, with the occasional use of 1,4-naphthoquinone (NQ) as an alternative. Recall that Simeon had highlighted these species as having electrochemical properties that are favorable for this application (Section 1.4, Figure 1.2). Both of these species can be purchased from Sigma Aldrich.

The major challenge in any of these experiments was the need for the dianion adduct. It is currently not possible to buy the dianion form of any quinone species, let alone the PQ or NQ variant. Therefore, the dianion form must be produced in the lab. There were four major attempts at this synthesis, and that work is summarized in Chapter 11: "Appendix: Experimental attempts at dianion quinone synthesis".

Table 4 Table of attempts to produce a stable salt of dianion quinone and the results.

Attempt	Result
Deprotonate hydroquinone using pyridine	Failed: pyridine is not basic enough to abstract either proton from hydroquinone in dimethyl sulfoxide.
Deprotonate hydroquinone using triethylamine (TEA)	Failed: TEA *should* be basic enough (even in DMSO) to remove at least the first proton. Time-lapsed data of CO_2 absorption show a difference in absorption kinetics of this mixture as compared to mixtures of either isolated TEA or isolated hydroquinone. Electrochemical experiments were either inconclusive or unproductive. TEA might be electrochemically active at the relevant potentials.
Electrochemical reduction of quinone in "flow battery configuration" with sacrificial mixture of supporting electrolyte as the counter electrode.	Produced a mixture of quinone and dianion that was used in the "flow battery configuration" to capture CO_2. However, experiments are time-consuming and it is difficult to transfer the electrolyte out of the "flow battery" apparatus, which limits the scope of experiments.
Electrochemical reduction of quinone in "bulk electrochemical cell" using ferrocene as the sacrificial reagent.	Reduced the quinone, and oxidized the ferrocene, but it was impossible to remove the electrolyte from the cell without exposing it to air. Ferrocenium is air-sensitive and degrades quickly, so this is the likely culprit.

Collectively, these challenges hindered demonstration and exploration of cell designs, and they motivated development of an alternative electrochemical couple that would work with quinones as the electrically-switchable sorbent. Ultimately, the most useful outcome of these failed quinone experiments was the development of a design in which ferrocene and quinone are electrochemically coupled to capture CO_2.

Several experiments planted the seeds that led ultimately to this new electrochemical couple, but the easiest connection can be made from the last attempt listed in Table 4. The plan was to use a bulk electrochemical cell with ferrocene as a sacrificial agent to produce a quinone-dianion mixture that could be pumped out of the cell and in to a given system for CO_2 capture (planar membrane, flow cell, etc). The bulk electrochemical cell set up is illustrated and pictured in Figure 4.1.

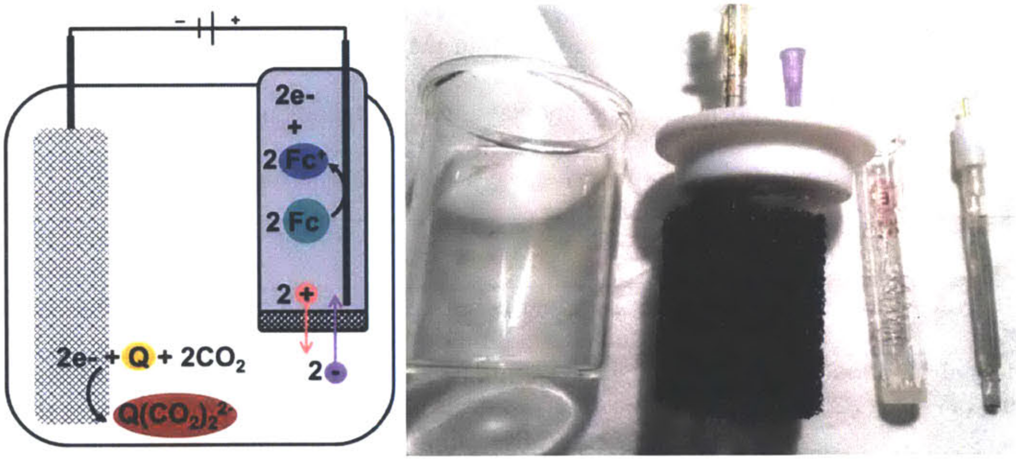

Figure 4.1 Cartoon (left) and picture (right) of bulk electrochemical cell system for partially reducing a quinone solution to produce a mixture of quinone and dianion adduct for use in experimental testing of cell designs.

The bulk electrochemical cell itself (the large glass cup) contains a glassy carbon electrode submerged in a solution of 9,10-phenanthrenequinone (PQ, “Q”), dissolved CO_2, and supporting electrolyte (shown as pink “+” and purple “-“). The counter electrode resides in a cylindrical glass chamber whose base is a glass frit. The glass chamber is submerged in the electrolyte inside the radius of the glassy carbon electrode. A solution containing ferrocene (Fc) with the same supporting electrolyte is segregated in the smaller glass chamber, and the frit allows ions to pass through in order to balance the charge of the two solutions as the electrochemical reactions progress. Whatever is in the glass chamber is oxidized via the counter electrode to provide electrons to reduce the quinone, and ions migrate through the glass frit to balance the charge transfer.

In terms of producing an electrolyte that could be pumped out of the cell and used in other experiments, this process failed repeatedly. The most likely explanation is that the quinone was reduced in the main chamber, the ferrocene was oxidized in the smaller chamber, and some ferrocenium permeated the glass frit and mixed with the quinone and dianion in the main chamber. This is a problem because ferrocenium would oxidize the newly-reduced dianion. Also, ferrocenium is highly air-sensitive, so any downstream exposure of the solution to air is a problem in terms of stability during transport [83, 84].

While the set up in Figure 4.1 was ultimately not a good way to produce an electrolyte for testing cell designs, the idea of coupling the ferrocene redox chemistry to the quinone redox chemistry is a good one. Since its discovery in the 1950's, ferrocene has been a staple in the electrochemical field [85], particularly for experiments in organic media. [86] The electrochemical oxidation of ferrocene to ferrocenium is reversible and kinetically fast in both directions in organic solvent. [85, 87, 88, 89] Both species are stable and reasonably soluble in polar organic solvents. [90, 91] In fact, the ferrocene-ferrocenium couple is often used as an internal reference potential [92], and sometimes the ferrocenium ion functions as an oxidizing agent. [93] Neither ferrocene nor ferrocenium reacts with CO_2. [94] For these reasons, the ferrocene-ferrocenium has been an attractive choice for experiments where an electron source was required to study quinone behavior. However, in all of the previous experiments, ferrocene was always ignored and/or used as a sacrificial agent.

By coupling ferrocene oxidation to quinone reduction, and dianion adduct oxidation to ferrocenium reduction, it is possible to achieve electrochemically-switchable absorption and desorption of CO_2 using the quinone sorbent. In other words, the quinone-ferrocene couple is an attractive alternative to the quinone-dianion couple for electrochemical systems for carbon capture. Both are illustrated side-by-side in Figure 4.2.

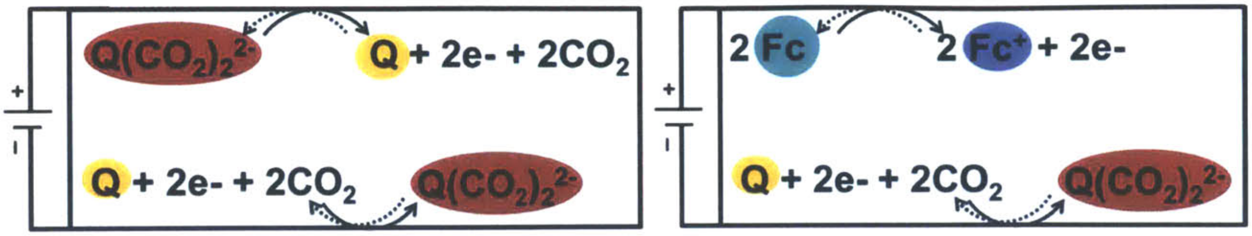

Figure 4.2 Illustration of the electrochemical couples employed for CO_2 capture. (left) The quinone-dianion electrochemical couple. (right) The quinone-ferrocene electrochemical couple. The reactions for absorption are illustrated with solid arrows, and the reactions for desorption are shown with dashed arrows.

The experimental results presented in this section show that it is possible to couple electrochemical oxidation of ferrocene to electrochemical reduction of quinone, and that it is easy to reverse the system. Two sets of results are presented in this chapter:

1. The current-potential curves for a system in which a set of two graphite electrodes are placed in electrolytes with various combinations of ferrocene, quinone, and supporting electrolyte.
2. Cycles of potentiostatic measurements in the same experimental set up showing that the quinone-ferrocene coupled reaction is cycle-able.

What follows are materials and methods, results, and conclusions sections. Once established, this electrochemical couple was used to demonstrate electrochemical CO_2 capture in three different configurations. Those results are presented in Chapters 5 and 6. Together, the results show that the electrochemical redox reactions of quinone and ferrocene can be coupled to each other and employed in several cell designs to capture carbon dioxide in a continuous fashion.

4.2 Materials and methods

The solvent for all experiments was dimethyl sulfoxide, purchased from Sigma-Aldrich (99.9% pure, anhydrous), and extracted from the container under Argon via a needle through the rubber septum. The following experimental materials were purchased and used directly from their containers: ferrocene (Sigma-Aldrich, 98%), 9,10-phenanthrenequinone (Sigma-Aldrich, >99%), tetrabutylammonium hexafluorophosphate (Sigma-Aldrich, >99.0%), and lithium perchlorate (Sigma-Aldrich). The electrodes were ¼" diameter, 6" long graphite rods that were purchased from McMaster-Carr. Experiments were performed in a small, glass electrochemical vial purchased from Bioanalytical Systems, Inc (Part #MF-

1082). Teflon caps purchased from Bioanalytical Systems, Inc (Part #ER-8946) were used to hold the graphite electrodes and the gas tube in place in the cell.

Volumetric flasks were cleaned with a combination of acetone and isopropyl alcohol and dried in an oven set at 100°C for at least 15 minutes. Mixtures of 50 – 100 mM concentrations of species were prepared using these volumetric flasks. A 10 mL sample of a mixture was placed in a small, glass electrochemical vial. Next, a Teflon lid was placed across the top of the electrochemical vial. One end of each graphite rod was cut to be thin enough to accommodate the electrical "alligator clips" at the ends of the wires connecting the potentiostat (Versastat 3, Princeton Applied Research) to the experimental system. The two graphite rods were placed in the respective holes in the Teflon lid, and they were held in place by black rubber o-rings. They were placed so that the bottoms were 1.2 cm above the base of the glass vial. The ends of the graphite rods that protruded from the experimental set up were filed down with a scalpel so that the "alligator" clips of the electrodes would remain clipped during the experiment. Figure 4.3 includes a schematic and picture of the experimental set up.

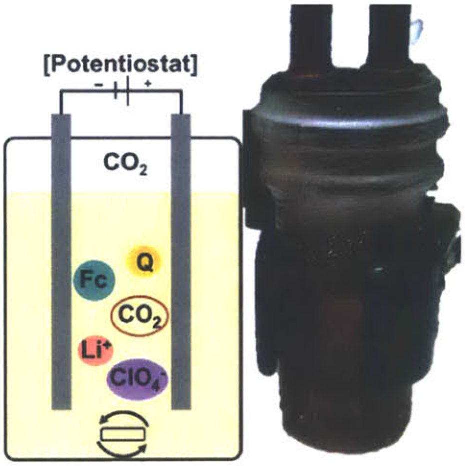

Figure 4.3 Schematic (left) and picture (right) of experiments to validate quinone-ferrocene electrochemical couple. Electrodes are made from 1/4" graphite rods, the electrolyte is stirred, and all experiments are performed under CO_2.

A small Teflon stir bar was placed in the vial, and the electrolyte was stirred at 500 rpm for the duration of the experiment. Prior to the electrochemical tests, the electrolyte was first purged with pure CO_2 for at least one hour, while stirring at 500 rpm. Note that brand new graphite rods were used for each experiment, and within a given experiment, several potentials were tested. New graphite rods are necessary because they are porous and very difficult to clean. Experimental results showed that re-using graphite rods affected the results of the experiments, presumably because reactive species may remain dissolved in the pores, and/or may crash out of solution. Work regarding the effect of washing and reusing graphite rods is presented in Chapter 10, entitled "Appendix: Notes on graphite electrodes in quinone-ferrocene experiments".

Within a given experiment, the method has the following steps:

1. Measure open circuit potential, 60 s
2. (Wait, 14 minutes)
3. Measure open circuit potential, 60s
4. Chronoamperometry: fixed potential, observe current, 300s (5 min)
5. (Repeat steps 1 through 4, doing different potentials in the chronoamperometry step)

The potentiostatic experiments are five minutes in duration because that time is long enough to achieve a pseudo steady state current, but it is not long enough (at the currents observed in this system) to produce significant changes in the chemistry of the electrolyte. The 14-minute breaks in between each potentiostatic run allow for stirring, gas bubbles, and time to break up any concentration boundary layers that have built up at the electrode surfaces during the chronoamperometry test, so that each test involves an electrolyte with uniform concentration everywhere. Each potentiostatic experiment was performed in order of increasing potential. The likelihood of side reactions and/or irreversible reactions increases with increasing potential. This means that performing the experiments from smallest to largest potentials minimizes the risk of side reactions that would create reactive intermediates that might affect subsequent chronoamperometry tests.

Table 5 contains descriptions of every mixture evaluated in these experiments. Two supporting electrolytes were tested: lithium perchlorate ($LiClO_4$) and tetrabutylammonium hexafluorophosphate

($tBAPF_6$). Each experiment entailed a series of chronoamperometry experiment, five minutes in duration, in the range of 0.1 V to 1.2 V, with a 16 minute break between each chronoamperometry.

Table 5 Concentrations of 9,10-phenanthrenequinone, ferrocene, and supporting electrolyte used in each experiment, along with the categorization of that experiment.

Phenanthrenequinone concentration	Ferrocene concentration	Supporting electrolyte concentration, mM	Designation
50 mM	50 mM	100 mM $LiClO_4$	Experiment
	50 mM	100 mM $LiClO_4$	control (no PQ)
50 mM		100 mM $LiClO_4$	control (no Fc)
		100 mM $LiClO_4$	control (no PQ, no Fc)
50 mM	50 mM	100 mM $tBAPF_6$	Experiment
	50 mM	100 mM $tBAPF_6$	Control (no PQ)
50 mM		100 mM $tBAPF_6$	Control (no Fc)
		100 mM $tBAPF_6$	Control (no PQ, no Fc)

4.3 Results

The electrochemical coupling of 9,10-phenanthrenequinone (PQ) and ferrocene (Fc) is demonstrated through a series of experiments that assess the reactions at graphite electrodes. The purpose is to validate the reactivity and reversibility of the two electrochemical reactions at graphite electrodes in the presence of CO_2. Figure 4.4 shows the current produced in mixtures containing PQ and Fc (diamond), PQ (triangle), Fc (square), and neither (circle). All mixtures have 0.1 M supporting electrolyte. The results in Figure 4.4 and Figure 4.5 are for systems with lithium perchlorate supporting electrolyte. The results in the two figures are identical, but Figure 4.4 has a linear ordinate and Figure 4.5 has a logarithmic ordinate.

For all mixtures, there is effectively no current through the system for potentials in the range of 0 to 0.5 V. For potentials greater than 0.5 V, there is still negligible electrochemical activity for all mixtures except the one that has *both* PQ and Fc. For that mixture, currents of 1 to 4 mA are observed for applied potentials in the range of 0.6 to 1.2 V. The distance between the two electrodes is less than 1 cm, and the electrolyte is stirred to reduce mass transfer resistances. The results show that the ferrocene reacts at one electrode, and the PQ reacts at the other, because those mixtures that lack either of those species produce minimal current.

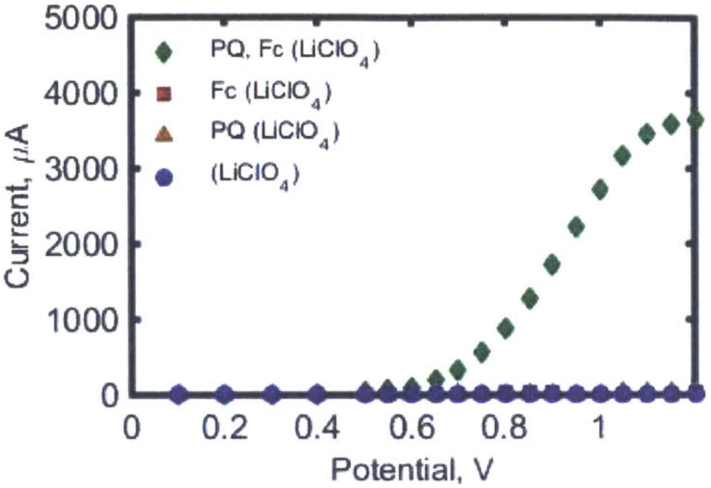

Figure 4.4 Steady-state current (μA) for each two-electrode experiment with graphite electrodes held at a constant potential (V). All experiments had 100 mM of $LiClO_4$ as the supporting electrolyte. This figure has linear axes.

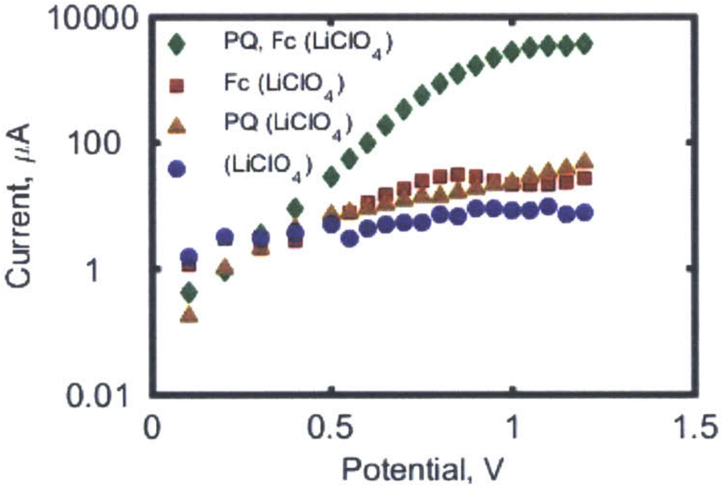

Figure 4.5 Steady-state current (μA) for each two-electrode experiment with graphite electrodes held at a constant potential (V). All experiments had 100 mM of $LiClO_4$ as the supporting electrolyte. This figure has a logarithmic ordinate.

Figure 4.5 shows the same data as Figure 4.4, but its ordinate is a logarithmic axis. The current for the system with equimolar amounts of PQ and Fc (green diamonds) is one to two orders of magnitude higher than the currents in the any of the three control experiments. These results support the hypothesis that in this system, the quinone is the species being reduced and the ferrocene is the species being oxidized.

Note that the currents produced in the PQ (diamond) and the Fc (square) control experiments are slightly higher than the current produced in the supporting electrolyte control (circle). While higher, these currents are still of the same order of magnitude as the control, and all three experiments produced currents that are two orders of magnitude less than the PQ-Fc system. Figure 4.6 shows more closely the currents for the control experiments on a linear axis where the maximum current shown is 100 μA.

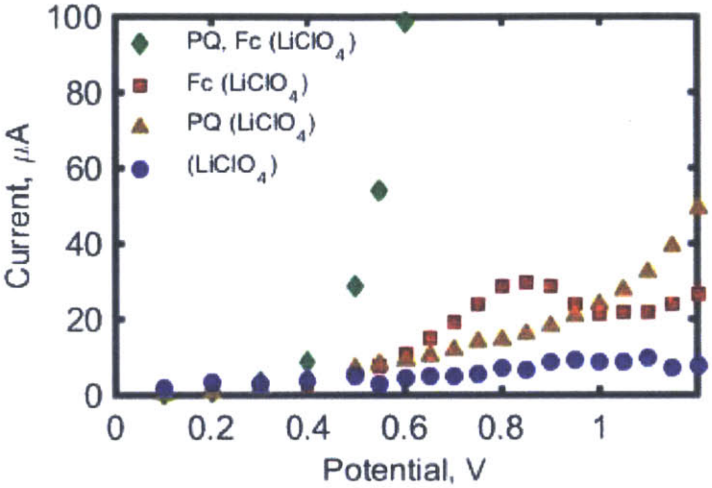

Figure 4.6 Steady-state current (μA) for each two-electrode experiment with graphite electrodes held at a constant potential (V). All experiments had 100 mM of $LiClO_4$ as the supporting electrolyte. This figure has linear axes, but it shows only those data whose currents have values between 0 and 100 μA.

Figure 4.5 and Figure 4.6 show clearly that the PQ-Fc system starts to exhibit dramatically higher currents at potentials as low as 0.5 V. However, Figure 4.6 also shows that at potentials of 0.8 V or higher, there is small but significant current in the PQ (diamond) and Fc (square) control experiments. In these controls, it is likely that the PQ is being reduced, and the ferrocene is being oxidized, respectively. There is no obvious counter-reaction to provide the electrons for the PQ or Fc reaction. In the PQ control, it is possible to oxidize any of the species available: PQ, ClO_4^-, DMSO, Li^+, or any trace contaminants. In the Fc control, it is possible to reduce any of the species available: Fc, Li, DMSO, ClO_4^-, CO_2, or any trace contaminants. Therefore, the potential range must be chosen carefully to isolate the redox coupling of PQ and Fc.

Figure 4.7 and Figure 4.8 contain the current measurements for the same set of mixtures in tetrabutylammonium hexafluorophosphate ($tBA^+PF_6^-$) supporting electrolyte. The results in the two figures are identical, but Figure 4.7 has a linear ordinate and Figure 4.8 has a logarithmic ordinate. Conceptually, the results are the same in both electrolytes. Two-electrode experiments show significant reactivity when coupling the electrochemical reactions of PQ and Fc in DMSO solvent using graphite electrodes.

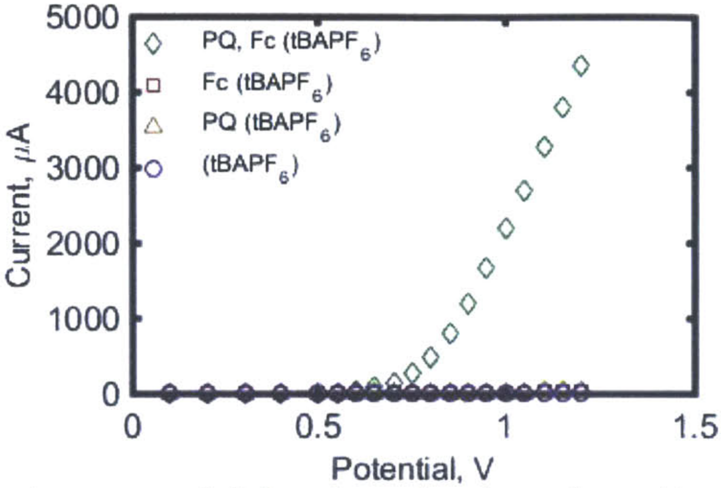

Figure 4.7 Steady-state current (μA) for each two-electrode experiment with graphite electrodes held at a constant potential (V). All experiments had 100 mM of tBAPF$_6$ as the supporting electrolyte. This figure has linear axes.

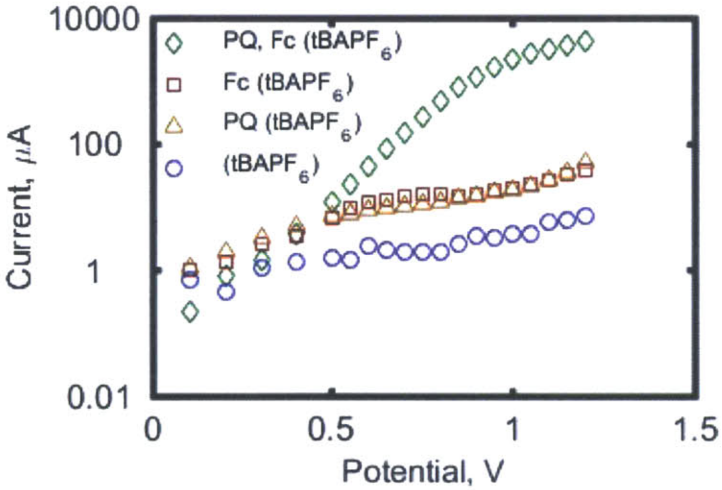

Figure 4.8 Steady-state current (μA) for each two-electrode experiment with graphite electrodes held at a constant potential (V). All experiments had 100 mM of tBAPF$_6$ as the supporting electrolyte. This figure has a logarithmic ordinate.

The results show that for potentials greater than 0.6 V, the current is at least 10 times higher for the sample with both PQ and Fc than for the samples that are missing one or both of those components. In this potential range, the high current is from a high rate of oxidation of ferrocene coupled to a high rate of reduction of PQ. Figure 4.8 shows the same currents on a logarithmic ordinate to better illustrate the scale of differences in the current. In the potential range of 0 – 0.2 V, the observed currents are all the same order of magnitude. In the range of 0.3 – 0.5 V, the currents of the samples with PQ or Fc or both are roughly the same. For potentials between 0.5 and 1.2 V, the currents of the samples with either PQ or Fc or both have currents that are significantly higher than the current of the "blank" control (tBAPF$_6$ in DMSO). It is interesting that the samples with isolated PQ or isolated Fc produce currents that are higher than the "blank" control for potentials greater than 0.5 V. This indicates that both PQ and ferrocene will exhibit *some* reactivity with something in the mixture. Either PQ or Fc could be reacting electrochemically with itself, the supporting electrolyte ions, and/or the solvent.

At a potential as low as 0.5 V, the sample with a mixture of PQ and Fc shows current significantly higher than either the PQ-only or Fc-only controls (12 μA versus 7 μA and 6.7 μA, respectively), and ten times higher than the blank control (12 μA versus 1.6 μA). Then, as the potential increases, the difference between the PQ-Fc sample and the others increases exponentially. At 0.7 V, the current for the PQ-Fc couple is 158 μA, while the PQ, Fc, and blank currents are 10, 15, and 2 μA, respectively.

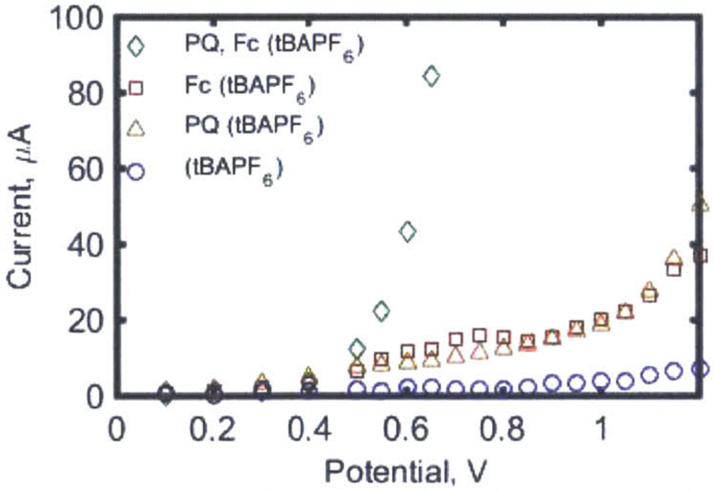

Figure 4.9 Steady-state current (μA) for each two-electrode experiment with graphite electrodes held at a constant potential (V). All experiments had 100 mM of tBAPF$_6$ as the supporting electrolyte. This figure has linear axes, but it shows only those data whose currents have values between 0 and 100 μA.

Figure 4.9 shows the steady-state current as a function of potential for systems with tBAPF$_6$ as the supporting electrolyte on a linear axis whose upper limit is 100 μA. In this figure, it is clear that the results are indistinguishable at low potentials. At a potential difference of 0.5 V, there is clear separation of the resulting currents. The "blank" has the lowest current. This validates the supporting electrolyte mixture as a control system because a supporting or inert electrolyte should behave essentially as a capacitor under these conditions. The PQ-alone and Fc-alone samples have distinctly higher currents than the blank, but still significantly lower currents than the PQ-Fc system, whose current is 10 times higher than the blank and 2 times higher than the other two controls. The PQ-Fc system shows exponential increases in current for all potentials greater than 0.5 V.

Note the "bump" in the Fc-alone results. This indication of reactivity in the range of 0.7-0.8 V is somewhat surprising, and a similar phenomenon occurs in $LiClO_4$. Note also that the Fc-alone and PQ-alone currents increase dramatically for voltages greater than 1 V. The scale of this reactivity is much less than the reactive coupling of quinone and ferrocene, but still indicates a system that is less inert than expected.

The purpose of these experiments is to elucidate a practical system of redox coupling for carbon capture that uses graphite electrodes. The results show that using two graphite electrodes, one can oxidize ferrocene and reduce PQ at significant rates when the potential difference across the system is 0.5 V or greater. These experiments were not intended to be measurements of standard potentials, nor are they. Simeon measured the formal potentials of the electrochemical reactions of quinones in the presence of CO_2, and he reports them as half-wave potentials relative to a ferrocene/ferrocenium internal reference in dimethyl formamide. [95] He also quantifies the equilibrium constant for the complexation of CO_2 by a quinone from the measured shift in the second-reduction potential. He reports a binding constant of 8.8×10^{16} M^{-1} for PQ in DMF at 30°C. With the acknowledgement of the multi-step mechanism that occurs during the electrochemical reduction of PQ and the chemical complexation with CO_2, he reports that the presence of CO_2 results in an effective two-electron transfer at the first reduction wave, and he reports a formal potential (half-wave potential) of -1.08 V versus ferrocene reference.

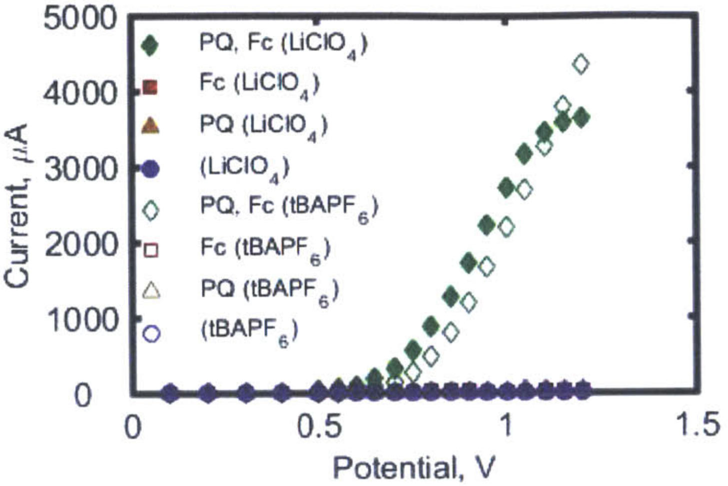

Figure 4.10 Current as a function of applied potential for the four experiments in both supporting electrolytes. The results from experiments with $LiClO_4$ have solid markers, and the results with $tBAPF_6$ have empty markers.

Figure 4.10 shows all eight results plotted on a single set of axes. The general conclusion is the same for the two electrolytes: the current produced for the samples with both PQ and Fc present is significantly higher than the current for samples that lack one or both species. Moreover, the incidence of this reaction occurs in the vicinity of 0.6 V for both electrolytes. The observed current is consistently higher in samples with $LiClO_4$ than in samples with $tBAPF_6$, except for experiments at potentials greater than 1.1V. The higher current is a result of having a lithium cation that is smaller and more mobile than the tetrabutylammonium cation (tBA^+). The concentrations of lithium and tetrabutylammonium are twice as high as the concentration of PQ or Fc in each case, so it is likely that lithium or tetrabutylammonium is the counterion for the PQ dianion in a given experiment. A faster and more compact cation can more easily stabilize and balance the PQ dianion, which facilitates a faster overall reaction.

Experiments on a sample with both PQ and Fc at 1.15 V and 1.2 V produce higher currents when $tBAPF_6$ is the supporting electrolyte, whereas the $LiClO_4$ produces higher currents at all other potentials tested. Closer inspection of the individual control experiments reveal significant reactivity between ferrocene and $tBAPF_6$. Thus, the lithium cation tends to produce higher currents for all systems except for samples that contain both Fc and $tBAPF_6$ at high potentials. Figure 4.11 shows the same set of eight results, but the ordinate is limited to the range of 0-100 μA. Comparing the two control experiments in which the supporting electrolyte is isolated, the current is higher in $LiClO_4$ for all potentials except 1.15 and 1.2 V, where the currents are identical. Similarly, the two control experiments in which PQ is isolated with the supporting electrolyte, the currents are higher in $LiClO_4$ for all potentials except 1.2 V, where the currents are identical. However, in the control experiments with Fc isolated in the supporting electrolyte, the current is significantly higher in $LiClO_4$ for potentials up to 1 V. In the range of 1.1 to 1.2 V, the current is higher for ferrocene isolated in $tBAPF_6$ than for ferrocene in $LiClO_4$. Taking these three comparisons together, it is clear that there significant reactivity between $tBAPF_6$ and ferrocene that is not observed with any of the other combinations.

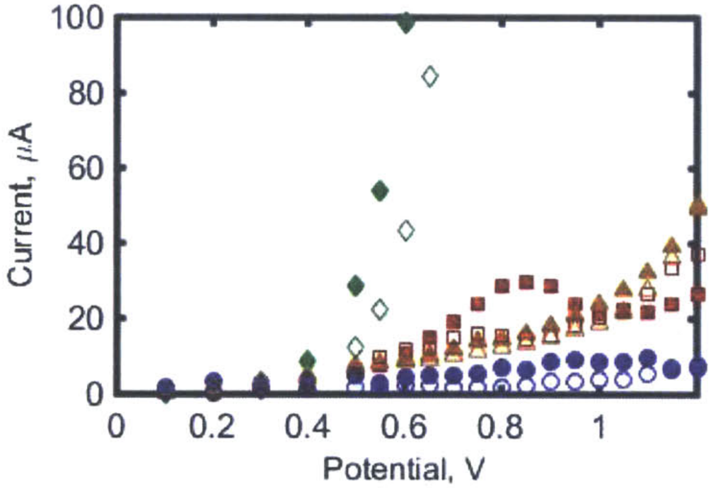

Figure 4.11 Current as a function of applied potential for the four experiments in both supporting electrolytes. The results from experiments with $LiClO_4$ have solid markers, and the results with $tBAPF_6$ have empty markers. Experiments with PQ and Fc are diamonds, Fc alone are squares, PQ alone are triangles, and supporting electrolyte alone are circles.

To summarize, when a potential of 0.1 to 1.2 V is applied across two graphite electrodes immersed in a mixture that has both PQ and ferrocene, the observed current is up to three orders of magnitude higher than when the same experiment is performed with a mixture that lacks one or both species. This means that it is possible to couple the electrochemical reduction of PQ to the electrochemical oxidation of ferrocene in dimethyl sulfoxide using graphite electrodes.

4.4 Reversibility results for the quinone-ferrocene redox couple and graphite electrodes

The results from the previous section show that in an experiment with two graphite electrodes, it is possible to couple the reduction of quinone at one electrode to the oxidation of ferrocene at the other electrode. However, those experiments do not show that the system is electrochemically reversible. The electrochemical couple for CO_2 capture must be highly reversible if it is to be used in any of the configurations presented in this thesis. In this section, the results from a series of reversibility experiments are presented to illustrate the (practical) degree of reversibility for this system.

The experimental set up is exactly the same for the reversibility experiments as described in Section 4.2, with the exception that only one electrolyte mixture was tested, and the steps in the potentiostat method were different. In the reversibility experiments, a mixture of 50 mM PQ, 50 mM Fc, and 100 mM $tBAPF_6$ in DMSO was placed in a glass vial with two (new) ¼" graphite rods as electrodes. This electrolyte was chosen as a representative mixture: equimolar concentration of quinone and ferrocene in a given electrode. The previous section shows that the supporting electrolyte does not (and should not) significantly affect the reaction chemistry. The presence of the supporting electrolyte is meant to reduce the contribution of migration to current and to enhance the conductivity of the electrolyte. Therefore, it is not necessary to test the other supporting electrolyte. Similarly, there is no reason to test any of the control mixtures, since it not germane to the demonstration of this technology to know if they are reversible or not.

The reversibility experiments had the following steps:

1. Measure open circuit potential, 60 s
2. (Wait, 14 minutes)
3. Measure open circuit potential, 60s
4. Chronoamperometry: positive, fixed potential, observe current, 300s (5 min)
5. Chronoamperometry: negative, fixed potential, observe current, 300s (5 min)
6. (Repeat steps 4 and 5 for 4 total "cycles" at a given fixed potential)
7. (Repeat steps 1 through 3)
8. (Repeat steps 4 and 5 for 4 total "cycles" at the next fixed potential, etc)

To summarize, a mixture of 50 mM PQ, 50 mM Fc was tested by cycling the potentials of two graphite electrodes between the positive and negative value of a given absolute potential for four cycles, and this process was repeated for potentials from 0.3 V to 1.2 V. The steady-state currents at each potential are presented in Figure 4.12.

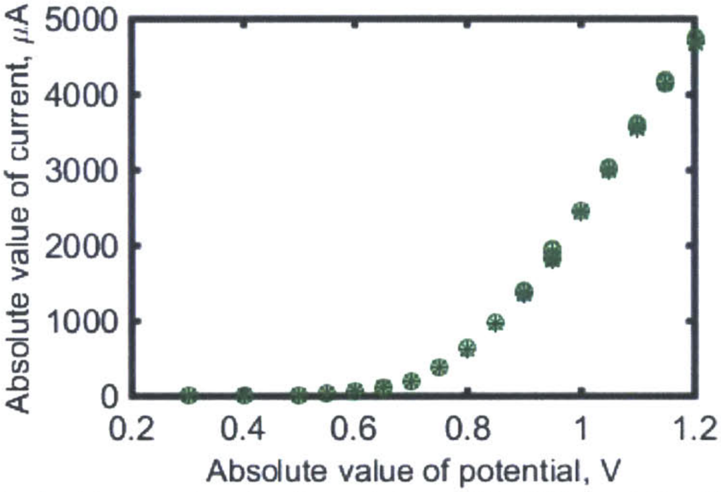

Figure 4.12 Steady state current produce by a mixture of 50 mM PQ and 50 mM Fc in 100 mM tBAPF$_6$ in DMSO under CO$_2$. Asterisks represent the positive potentials, and circles are the negative potentials.

Figure 4.12 shows the steady-state currents for the system as it is held at positive (asterisk) and negative (circle) potentials. Potentials from 0.3 V to 1.2 V were tested, in increasing order. The data show that at most potentials, there is no difference between the current observed at positive potential and the current observed at negative potential.

The fact that the currents at positive and negative potentials have the same magnitude leads to several positive and somewhat surprising conclusions. The current measured by the system is the net flux of electrons out of the cathode and into the anode. This flux is a function of the reactant concentrations, diffusivities, and kinetics. The diffusivities of neutral quinone and ferrocene are approximately the same, and the concentrations were set to be the same, so one would expect the currents to be the same only if the diffusivity and concentration were the only relevant factors. However, ignoring diffusivity and concentration gradient, the current from a positive voltage difference is a result of the combination of ferrocene oxidation kinetics and quinone reduction kinetics. Ferrocene oxidation is typically considered to be a one-step, one-electron reaction. [96] Quinone reduction has several steps, especially in the presence of

CO_2. Therefore, the current from a positive voltage is a result of the coupling of those two sets of reaction kinetics. Similarly, the current from a negative voltage comes from the combination of ferrocenium reduction kinetics and quinone dianion adduct oxidation kinetics. Again, the ferrocenium reduction can most likely be envisioned as a one-step, one-electron transfer. Quinone dianion adduct oxidation is not simple, as indicated by cyclic voltammetry. [95]

Therefore, it is a positive, although somewhat surprising, result to observe that the forward and backward reaction rates are the same, overall, in both directions. This supports the assumption that all four reactions (oxidation and reduction of quinone and ferrocene) are kinetically fast, at least relative to the mass transfer in the system. If the reaction kinetics of one reaction were significantly slower, then the observed current at the same potential would have been consistently lower in that direction. Also, if any of the reactions were irreversible, then the current would have degraded over time. Instead, the current was consistent and repeatable throughout the experiment, which indicates that the coupling of the reversible redox chemistries of quinone and ferrocene can be used in practical systems without concern for electrochemical degradation of species.

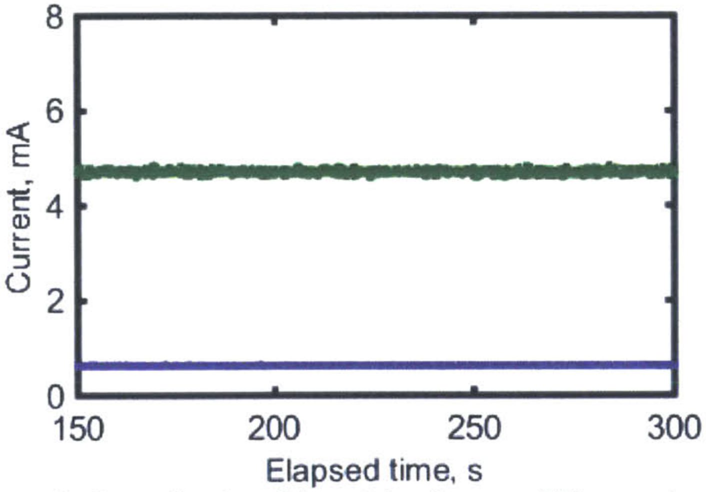

Figure 4.13 Current (mA) as a function of elapsed time for reversibility experiments at +/- 0.8 V (blue) and +/- 1.2V (green). The chronoamperometry measurements at positive potentials are indicated by a solid line, and the measurements at negative potentials are shown as dashed lines.

Figure 4.13 is a plot of the time-elapsed current measurements for the reversibility tests at 0.8 V (blue) and 1.2 V (green). The purpose of this figure is simply to show that the differences between the positive and negative current measurements at a given potential are small. These two samples are representative of the rest of the data in the reversibility test.

4.5 Conclusions

Electrochemical coupling of the redox reactions of PQ and Fc is a viable chemical system for CO_2 capture. These experiments prove that it is the quinone being reduced and the ferrocene being oxidized, and the experiments prove that the electrochemical coupling of the redox chemistries of quinone and ferrocene are reversible. The system can survive many cycles because no species degrades or reacts irreversibly. Furthermore, the reactions do not require catalytic electrodes. Instead, simple, graphite electrode surfaces work well for this chemistry.

5 Experimental demonstration of powered capture in a flowing electrolyte

5.1 Introduction

Chapter 3 is a design analysis for carbon capture using an electroactive sorbent in laminar flow between two planar electrodes. Chapter 4 introduces the capabilities of a new chemistry for carbon capture in an electrochemical system. This chapter presents results from a bench-scale demonstration of electrochemical carbon capture in a flowing electrolyte using the quinone-ferrocene couple. The chapter begins with a discussion of the design and construction of the demonstration cell. The rest of the chapter is the presentation and discussion of results from demonstration with a mixture of quinone and ferrocene in contact with 15% CO_2, 85% nitrogen (N_2). The chapter closes out with conclusions and suggestions for future work.

5.2 Design and construction of demonstration cell

The bench scale test cell was built by reconfiguring the components of a polymer electrolyte membrane (PEM) fuel cell test cell and incorporating a custom-built part for the flowing electrolyte. Figure 5.1 is a picture of the fuel cell test cell and its graphite electrodes.

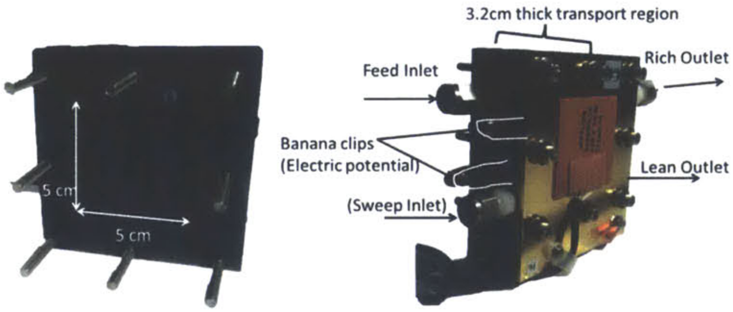

Figure 5.1 (left) Picture of a graphite gas diffusion electrode with bolts. (right) Picture of the assembled test cell.

The picture on the left in Figure 5.1 is a graphite gas diffusion electrode that has a 5 cm x 5 cm area cut with 1 mm deep gas channels. They have a serpentine flow pattern. This picture also shows the "through-bolt" assembly – those bolts span the entire cell. The picture on the right is the assembled test cell. The current-collector plates are gold-plated copper. This test cell is useful because it is designed to be gas-tight, and it comes with the electrical hardware (option for reference electrodes, banana clips) and fittings for connecting the test cell to a gas source and a gas outlet.

The fuel cell test cell has been re-designed to have a flowing electrolyte between the two plates. The existing gas contactor plates and current collector plates remain intact. Several prototype parts for the flowing electrolyte region have been designed and constructed. Early prototypes were made of Delrin, but the final prototype part was made from Teflon. Teflon is more difficult to machine, but easier to use in a system where sealing is important. The Teflon flow part has threaded fittings on both sides for the inlet and outlet tubes. All fittings have ¼" NPT threads. There are two channels carved into the Teflon to accommodate O-rings, which prevent leaks. Seven bolts are used to clamp the entire cell together. Figure 5.2 shows two design drawings for this part.

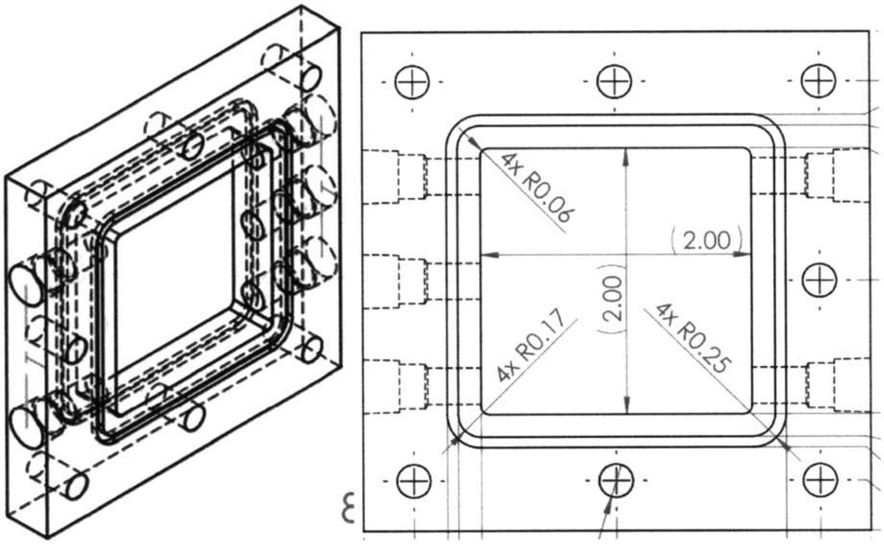

Figure 5.2 Two design drawing of the Teflon part for an electrochemical flow cell.

The top view of the part shows the position of the holes for the bolts to pass through this part to the other electrode. It also shows two fluid tubes on one side of the channel, and three on the other. These are holes in which a ¼" NPT threaded tube fitting screws. The purpose of having multiple inlet and outlet holes is to allow for experimentation with different flow configurations.

5.3 Demonstration cell with ferrocene model system

Operation and functionality of the fuel cell test cell was validated using the ferrocene-ferrocenium couple as a model system for the quinone-dianion couple. Ferrocene, and ferrocenium hexafluorophosphate were purchased from Sigma Aldrich. The experiment was performed in a glove box to ensure the absence of oxygen. Upon exposure to oxygen, ferrocenium will react and degrade. The system was tested on an electrolyte composed of 10 mM ferrocene (Fc), 9.0 mM ferrocenium hexafluorophosphate ($FcPF_6$), and 100 mM tetrabutylammonium hexafluorophosphate ($tBAPF_6$) in dimethyl sulfoxide (DMSO). Each trial was performed at a fixed cell potential, and the current was measured as a function of time (chronoamperometry) for 10 minutes. The fluid was pumped at a rate of 2.2 mL/s using a centrifugal pump. The results are shown in Figure 5.3.

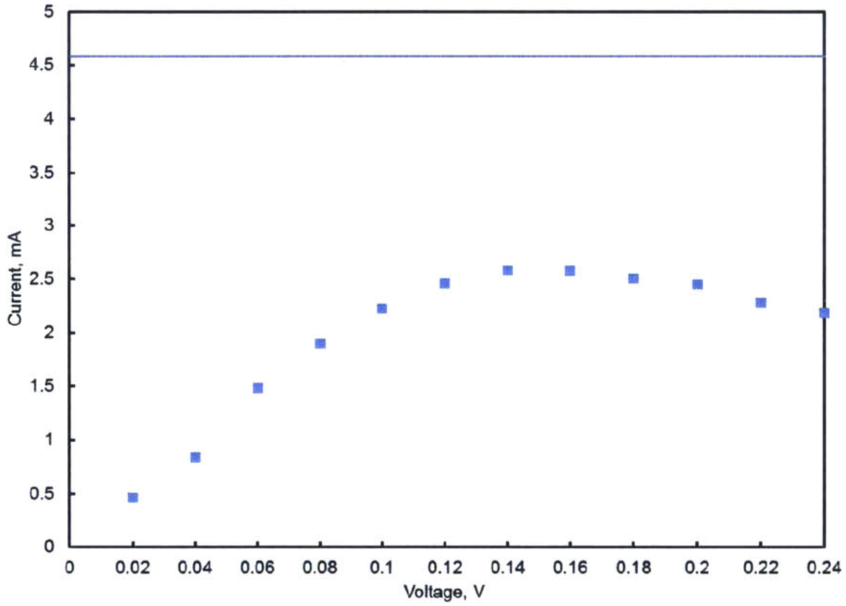

Figure 5.3 Steady-state current (mA) as a function of cell potential (V) for the ferrocene-ferrocenium redox couple in a laminar flow cell. The line at the top of the figure is the theoretical limiting current.

The straight line near the top of Figure 5.3 is placed at the theoretical limiting current calculated from the similarity solution using the experimental concentrations and flow rate. Each square is the steady-state current measured at that given potential. As expected, the current increases linearly with potential at low potentials. At higher values, the change in current as a function of potential should decrease as the system approaches the limiting current. Near the limiting current, the current should be relatively invariant with potential. The results show that at potentials greater than 0.14 V, the current stops increasing with potential. In the range of 0.14 to 0.24 V, the current actually decreases with increasing potential. During the time these potentials were applied, qualitative changes in the fluid were observed. The working fluid is normally a dark blue color, because ferrocenium hexafluorophosphate is blue. However, as the fluid circulated through the cell at higher potentials, one can observe a shift from blue to dark brown. One explanation is that there is a parasitic reaction that occurs at higher potentials that consumes either ferrocene or ferrocenium in an irreversible reaction. Because this parasitic reaction appears to be dependent on the electrochemical potential, it is most likely that this parasitic reaction involves the electrochemical reduction or oxidation of one of the species, or of the solvent.

The results show, qualitatively, the basic functionality of the flow cell. It was not possible to explore this system with the quinone-dianion couple without a salt of the dianion species. Instead, the ferrocene-ferrocenium couple served as a model system. The results at higher potential revealed the limitations of this redox couple, in addition to the fact that it is not able to capture CO_2. Therefore, subsequent experimental work employed the quinone-ferrocene in the electrochemical flow system.

5.4 Demonstration of CO_2 capture in electrolyte flow cell

5.4.1 Introduction

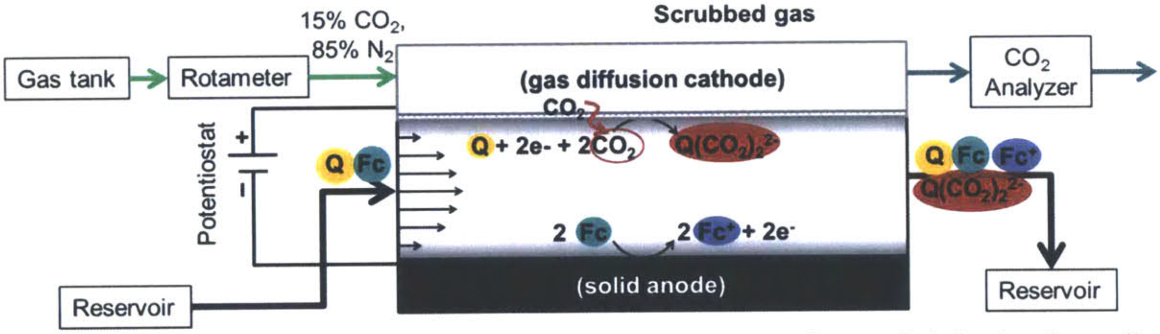

Figure 5.4 Schematic of experimental set up for quinone-ferrocene redox couple in laminar flow cell.

Figure 5.4 is a schematic of the complete bench-scale set up for experimental demonstration of CO_2 capture using the quinone-ferrocene redox couple in the electrolyte flow cell. The flue gas is a mixture of 15% CO_2, 85% N_2 from a tank. The volumetric flow rate of this mixture is controlled by a rotameter, and this gas stream flows in to the gas diffusion electrode and contacts the electrolyte at the wetted porous carbon mat. At that interface, the quinone absorbs some CO_2 as it is reduced to form the dianion adduct. The remaining gas flows out of the system and in to the CO_2 Analyzer, which provides real-time measurements of the percentage CO_2 in this gas stream. An electrolyte containing phenanthrenequinone

(PQ) and ferrocene (Fc) is pumped from a reservoir in to the electrochemical cell, where it flows between two planar electrodes. One electrode is the porous carbon cathode in contact with the gas phase, and the other is a solid, graphite anode. The electrolyte exits the cell and goes to a separate reservoir. The potential of the electrodes is controlled by a potentiostat, and that machine measures the current in real-time.

5.4.2 Materials and methods

The solvent for all experiments was dimethyl sulfoxide, purchased from Sigma-Aldrich (99.9% pure, anhydrous), and extracted from the container under Argon via a needle through the rubber septum. The following experimental materials were purchased and used directly from their containers: ferrocene (Sigma-Aldrich, 98%), 9,10-phenanthrenequinone (Sigma-Aldrich, >99%), and lithium perchlorate (Sigma-Aldrich).

Volumetric flasks and 3-neck flasks were cleaned with a combination of acetone and isopropyl alcohol and dried in an oven set at 100°C for at least 15 minutes. Every experiment involved an electrolyte that is 50 mM PQ, 50 mM Fc, and 100 mM $LiClO_4$ in dimethyl sulfoxide (DMSO) solvent. This mixture was prepared using these volumetric flasks. 100-200 mL of this mixture was placed in a clean and dry 3-neck flask with a clean and dry stir bar, and purged with a gas stream that is 15% CO_2, 85% N_2 while stirring for about two hours before the experiment began.

The test cell described in Section 5.2 was configured as shown in Figure 5.5 to facilitate this particular experiment: quinone reduction at a porous cathode in contact with a flue gas mixture, and ferrocene oxidation at a solid anode. Every part of the test cell was cleaned and dried before and after each experiment. For each experiment, the test cell was assembled according to the layers shown in Figure 5.5. The bolts that span the entire “sandwich” were placed and finger tightened in a diagonal and then circular pattern. A torque wrench was used to tighten the bolts to 5 in-lb torque in a diagonal pattern, and then they were further tightened to 6 in-lb torque in a circular pattern. Having even pressure is especially important for this particular cell design because the bolt pattern is slightly asymmetric (one side has three bolts while the other has two).

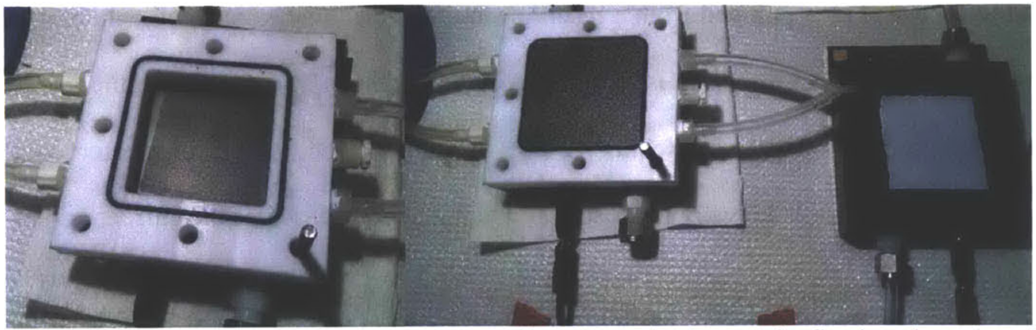

Figure 5.5 (left) Picture of the solid anode and the Teflon frame that houses the flowing electrolyte. (right) Picture of the porous carbon fiber mat that spans the top of the Teflon frame, acting as a porous cathode. At the far right the gas diffusion electrode (cathode) is shown with a piece of porous polypropylene.

Figure 5.5 shows the components of the test cell and their assembly. The picture on the far left shows the solid, planar graphite electrode underneath the Teflon fixture, and the plastic tubing for the electrolyte going in and out of the Teflon fixture. The picture in the middle shows the same set up as the left picture with the addition of the carbon fiber mat that functions as the porous cathode. At the far right the gas diffusion electrode (cathode) is shown with a piece of porous polypropylene (Celgard brand) that is used to prevent the electrolyte from leaking in to the gas channels. The porous carbon fiber mat makes physical, electrical contact with the graphite cathode around the border of the polypropylene.

A practical design challenge to this particular test cell design was the configuration of the gas channels, the porous polypropylene layer, the carbon fiber mat, and the o-ring. This configuration is both delicate and important. The polypropylene layer must span the gas channels. Its purpose is to prevent the electrolyte from leaking in to the gas channels and plugging or interrupting the path of the gas through the gas diffusion electrode. The carbon fiber mat must have physical, electrical contact with the graphite electrode to maintain the electric circuit. Electrons move through the solid graphite electrode to the carbon fiber mat and then to the reactants in the electrolyte. To maintain electrical contact and simultaneously minimize leaking, the polypropylene layer must be cut to an area slightly greater than the area of the gas channels and the carbon fiber mat must be cut to an area that is larger than the polypropylene layer but smaller than the area designated by the bolt holes.

Figure 5.6 is a picture of the full experimental set up, which includes the flow cell (bottom left), the CO_2 Analyzer (top left), the rotary vane pump (center, black), and the 3-neck flask acting as a reservoir for the circulating electrolyte (right).

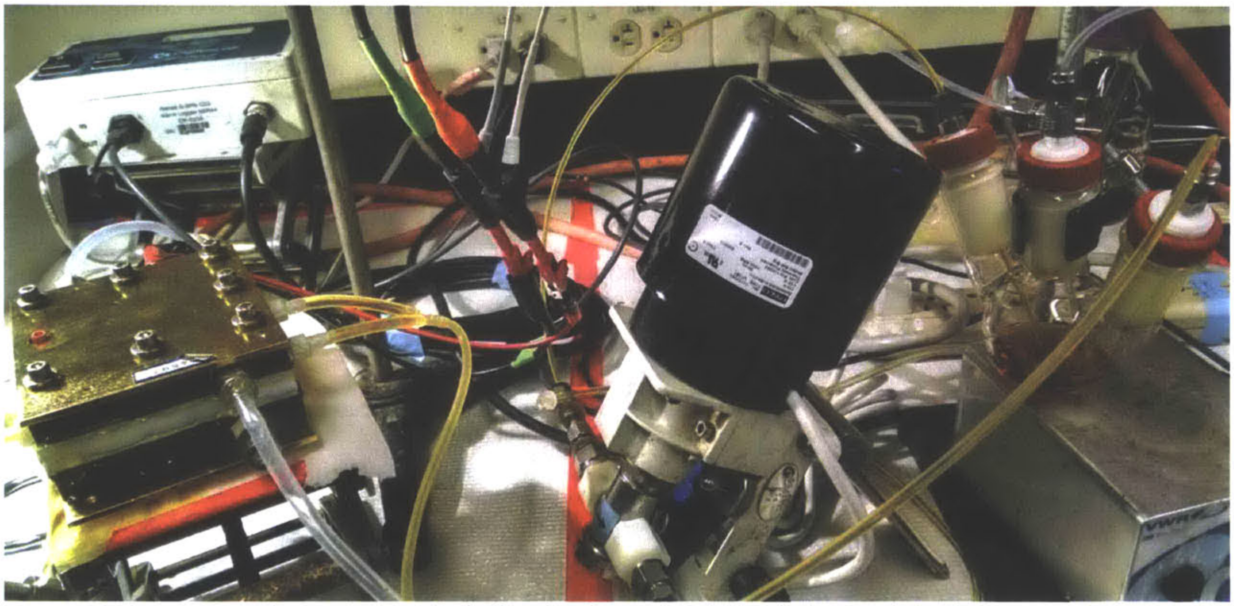

Figure 5.6 Experimental set up, including the electrochemical cell (bottom left), the CO_2 Analyzer (top left), the rotary vane pump (center, black motor), and the 3-neck flask reservoir for the recirculating electrolyte (right).

The CO_2 Analyzer was purchased from co2meter.com, and it uses non-dispersive infrared (NDIR) technology to measure the fraction of CO_2 in a gas sample. It connects to the computer via a USB port, and the data can be exported as .CSV. The rotary vane pump is a laboratory and industrial metering pump purchased from Fluid Metering Inc, and outfitted with special Teflon fittings that are safe to use with aggressive organic solvents like DMSO. All tubing was either 1/8" Teflon tubing or chemically-resistant Masterflex tubing, and all fitting were either polypropylene or stainless steel. The Teflon stoppers in the 3-neck flask are chemically-resistant. They were modified to be threaded for ¼-NPT stainless steel compression fittings that would seal the connection between Teflon stopper and the Teflon tubing passing through the stainless steel fittings. Teflon gaskets were placed between the Teflon stopper and the necks of the glass flask to seal the connection.

5.4.3 Results

Many experiments were performed in which a mixture of 9,10-phenanthrenequinone (PQ) and ferrocene (Fc) flowed through the test cell and the current, potential, gas composition, gas flow rate, and liquid flow rates were recorded. The results are split in to two sections according to the two configurations that were most successful. The results show clearly that upon application of a potential gradient across the cell, the system produces current and the system absorbs CO_2 from a mixture of 15% CO_2 and 85% N_2 at ambient temperature and pressure.

The first successful experiments with the demonstration happened with the membrane and carbon fiber mat arranged according to Configuration A. Table 2 contains the materials and experimental parameters and a detailed description of the configuration of polymer membrane and carbon paper.

Table 6 Table of experimental conditions for runs 1 and 2, performed with Configuration A.

Index	Membrane	Carbon paper	Gas flow rate mL/min	Liquid flow rate mL/min	Potential Volts	Notes
1	Celgard 3401	Spectra Carb 2050-A 200 μm thick	6.1 - 6.5	3.3	1	Leaked, but slowly enough to get useful data.
2	Celgard 3401	Spectra Carb 2050-A 200 μm thick	6.1 - 6.5	26	1	Leaked, and ran out of material.
Configuration A = Polymer membrane cut to span entire graphite plate in flow direction, but only slightly wider than exposed gas channel area. Carbon paper cut to be larger than O-ring but inside the bolts. Bolts tightened to 5 and then 6 in-lb torque.						

Each experimental run involves establishing a baseline for the observed percentage CO_2, and then using the change in percentage CO_2 combined with a constant inlet flow rate and composition to quantify the amount of CO_2 captured in a given run. Note that there is some delay between the inception of the electrochemical activity and the change in gas composition, and this delay is proportional to the length of piping between the electrochemical system and the CO_2 analyzer. Figure 5.7 shows the observed percentage of CO_2 in the outlet gas (right) and the observed current (left) for the duration of Run 1 (see

Table 6 for details). The data show clearly that the amount of CO_2 in the outlet gas drops in response to the electrochemical reaction that produces quinone dianion, which binds CO_2 and absorbs it.

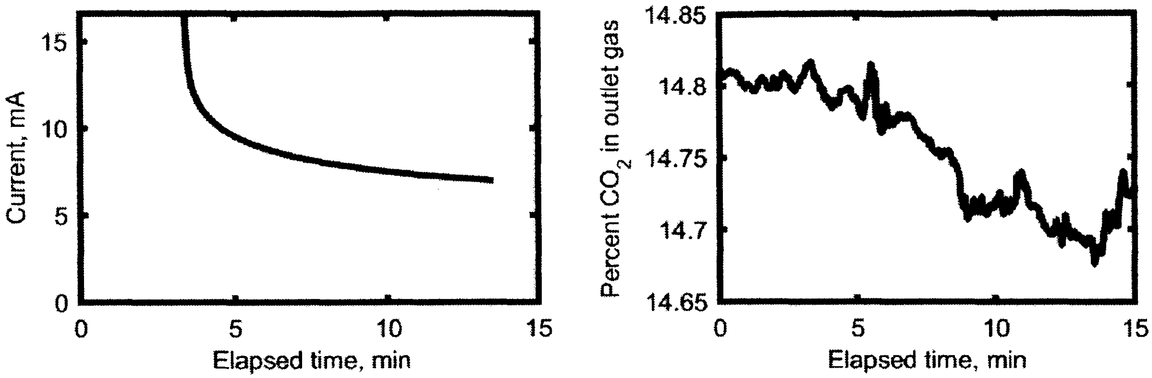

Figure 5.7 Experimental data from Run Index 1 of the quinone-ferrocene couple in the flow system showing the current (left) and the percent of CO_2 in the outlet gas measured by the CO_2 analyzer (right).

In each experiment, the current, gas flow rate, and gas composition data can be converted to molar flow rates of CO_2 and electrons. These flow rates can be integrated to quantify the cumulative amounts of electrons transferred and CO_2 captured. Shown below are those data for this run. Current efficiency describes the rate of electron transfer compared to the rate of CO_2 capture. In Run 1, the rate of electron transfer was 7.3×10^{-8} moles/s at steady state, and the comparable rate of CO_2 capture was 6.4×10^{-9} moles/s. At these rates, there is a ratio of 11 moles of electrons transferred per mole of CO_2 captured, which equates to a current efficiency of 8.8%.

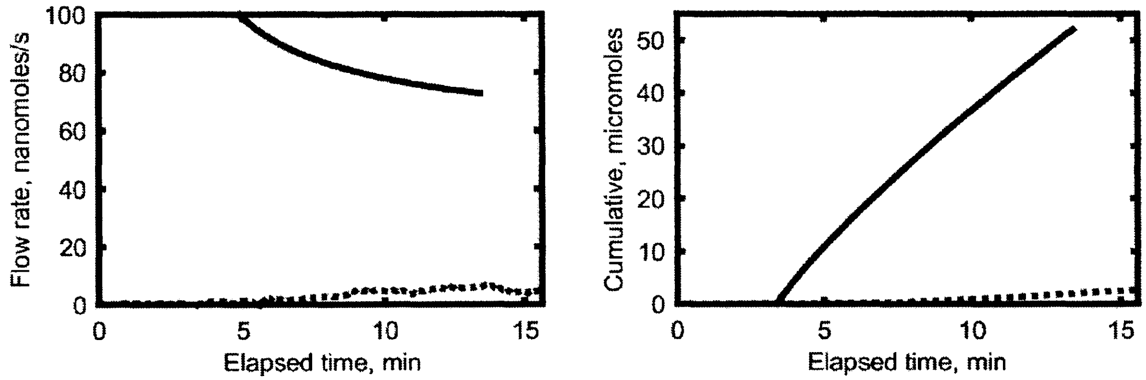

Figure 5.8 Run 1 flow rate and accumulation results. (left) Flow rate of electron transfer (solid) and CO_2 absorbed (dashed) in nanomoles/s over the duration of the experiment (min). (right) Cumulative amount of electrons transferred (solid) and CO_2 absorbed (dashed), in units of micromoles, over the duration of the experiment (min).

Run 2 was attempted under the same conditions but with a faster electrolyte flow rate. The results are shown in Figure 5.9. As expected, the faster electrolyte flow rate produces a higher current, but the commensurate CO_2 capture cannot be observed because the system to measure CO_2 failed. It may have failed because it leaked too much and ran out of material, which means the electrolyte chamber was no longer filled, and the pressure changed. The results were not good enough for further analysis.

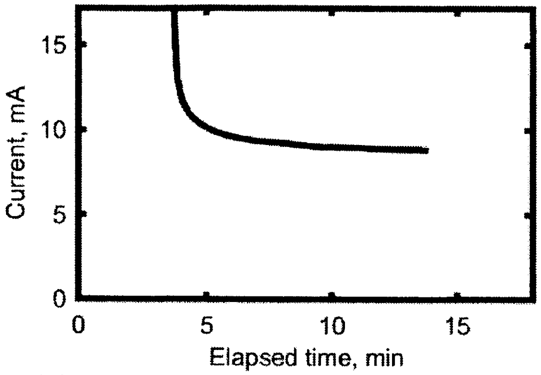

Figure 5.9 Experimental data from Run 2 of the quinone-ferrocene couple in the flow system showing the current (mA) as a function of elapsed time (min).

Between two sets of runs, the cell was rebuilt and reconfigured to address a leaking issue. In the second configuration (Configuration B), the polymer membrane was cut to span the entire graphite plate in the flow direction, but only slightly wider than the exposed gas channel area. The carbon paper was cut to the same area as the O-ring so as to maximize its contact with the graphite but to prevent leaking "across" the O-ring via the porous carbon paper and membrane. Again, the system was sealed all around with hot glue and again, the system leaked. The system leaked a lot more slowly in this set up. However, the fact that the system still leaks places a constraint on the number and duration of experiments possible before enough material was lost as to render the system useless.

Table 7 Table of experimental conditions for Runs 3 and 4, performed with Configuration B.

Index	Membrane	Carbon paper	Configuration	Gas flow rate mL/min	Liquid flow rate mL/min	Potential Volts
3	Celgard 3401	Spectra Carb 2050-A, 200 μm thick	B	6.2	11.2	1
Note: Run 3 leaked, but slowly enough to get useful data.						
4	Celgard 3401	Spectra Carb 2050-A, 200 μm thick	B*	6.3	11.2	1
*Replaced right side tubing at inlet to try to get better liquid flow Note: Run 4 leaked out the sides, and liquid leaked in to gas tubes. It stabilized there, and the gas would bubble through the liquid before heading in to the CO2 analyzer.						
5	Celgard 3401	Spectra Carb 2050-A, 200 μm thick	(same as 4)	6.3	11.2	1.5

Configuration B = Polymer membrane cut to span the entire graphite plate in flow direction, but only slightly wider than exposed gas channel area. Carbon paper cut to the same area as the O-ring, so as to maximize its contact with the graphite but to prevent leaking "across" the O-ring via the porous carbon paper and membrane. Bolts tightened to 5 and then 6 in-lb torque. The system was sealed all around with hot glue.

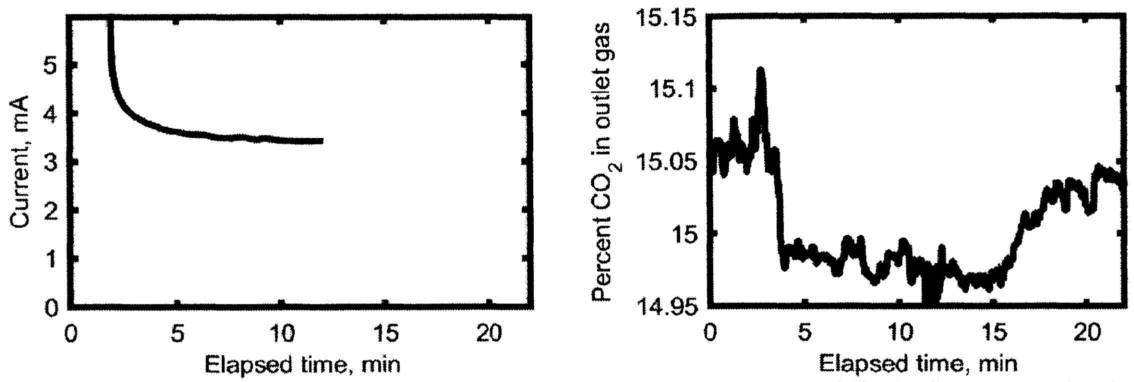

Figure 5.10 Experimental data from Run 3 of the quinone-ferrocene couple in the flow system showing the current (left) and the percent of CO_2 in the outlet gas measured by the CO_2 analyzer (right).

Run 3 improved upon Runs 1 and 2 in two ways. First, although it leaked, the slower leak provided more time to get better results. Second, the plot of percent CO_2 over time in Figure 5.10 more clearly shows the capture of CO_2 in response to an applied electrochemical potential and it shows a recovery of the baseline once the cell is turned off. These data clearly highlight the link between CO_2 capture and current.

Figure 5.11 contains plots of molar flow rates of electrons and CO_2, and the accumulation of these species. In Run 3, the rate of electron transfer was 3.5×10^{-8} moles/s at steady state, and the comparable rate of CO_2 capture was 4.9×10^{-9} moles/s. At these rates, there is a ratio of 7 moles of electrons transferred per mole of CO_2 captured, which equates to a current efficiency of 14.7%.

Note that this run produced a higher current efficiency (14.7% versus 8.8%), but a lower overall current. A comparison of the results reveals that Run 3 levelled off at 3.5 mA given 1V of potential and 11 mL/min liquid flow while Run 1 produced over 8 mA of current at +1V of potential and 3.3 mL/min. This is unexpected, since faster flow rates should produce higher currents at constant potential. The reason for the lower current is the difference in the configuration of the carbon paper and polymer membrane in the cell. In configuration B, there is less total electrochemical surface area available because the carbon paper was cut to a smaller footprint. However, this configuration with the smaller footprint is more efficient than

Configuration A. In the less efficient configuration, much of the contact area is not exposed to the gas phase, so there is no CO_2 to be absorbed, and the current that flows through there is wasted.

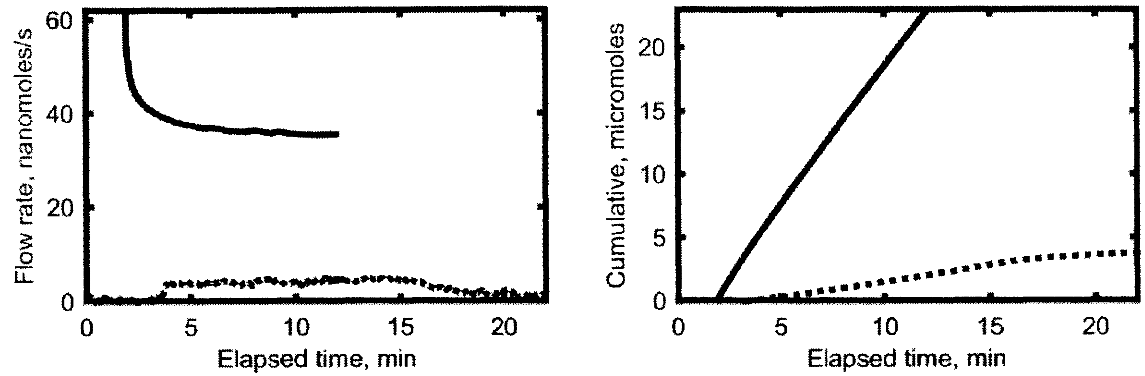

Figure 5.11 Run 3 flow rate and accumulation results. (left) Flow rate of electron transfer (solid) and CO_2 absorbed (dashed) in nanomoles/s over the duration of the experiment (min). (right) Cumulative amount of electrons transferred (solid) and CO_2 absorbed (dashed), in units of micromoles, over the duration of the experiment (min).

Table 8 Summary of electron and CO_2 flow rates, and experimental efficiencies.

Run Index	Electron flow rate moles/s	CO_2 absorption rate moles/s	Mole ratio e-:CO_2	Current efficiency
1	7.3×10^{-8}	6.4×10^{-9}	11:1	8.8%
3	3.5×10^{-8}	4.9×10^{-9}	7:1	14.7%

Table 8 summarizes the key results from Runs 1 and 3. Under an applied potential of 1 Volt, Run 1 produced a steady state current of 7 mA, and absorbed CO_2 at a rate of 6.4 nanomoles per second. These rates correspond to a ratio of 11 moles of electrons transferred per mole of CO_2 captured. In this case, current efficiency is defined as the (molar) rate of electron transfer divided by the (molar) rate of CO_2 absorption, presented as a percentage. Run 1 captured carbon at an 8.8% current efficiency. Run 3 had the same applied potential (1 V) but a faster electrolyte flow rate and a different configuration of carbon mat and polypropylene. The results were a steady state current of 3.4 mA and absorption of CO_2 at a rate of 4.9 nanomoles per second. While the flow rates of current and CO_2 were both lower, the efficiencies were higher. Run 3 operated at a 14.7% current efficiency, corresponding to a ratio of 7 moles of electrons transfer per mole of CO_2 captured.

One would expect Run 3, at a higher liquid flow rate, to produce higher currents and CO_2 absorption rates but lower efficiencies. The fact that the opposite is true can be explained in part by some of the experimental factors. If a system is mass transfer limited and in the regime of laminar flow, the steady state current (mass flux) is proportional to the Peclet number with an exponential of 1/3. This means that although the linear velocity is four times greater in Run 3, the limiting current would only be 1.5 times greater, at most. Also, the particular pump used in this experiment produced a high degree of variability in flow rates at a given setting, which means it is feasible that the second flow rate was not actually four times higher than the first.

A more important factor is the arrangement of the carbon mat and the polypropylene in the two experiments. The carbon mat in Run 1 was cut to have an area equal to the area inside the bolts, while the carbon mat in Run 3 was cut to a much smaller area. The surface tension between the electrolyte and the carbon mat was such that the carbon mat was completely wetted for the duration of the experiment. Moreover, the electrolyte had a tendency to creep in to the region in which the graphite electrode, O-ring, and polypropylene were meant to seal the flow area. As a result, there was some electrode surface area in which the electrode and electrolyte contacted each other, but did not contact the gas phase. One could explain the efficiency differences between Runs 1 and 3 as being directly proportional to the amount of this "unused" electrode area. Run 1 had a high amount of electroactive area that was not exposed to the gas phase (because the carbon mat had a high area), whereas there was much less *unused* electrode area in Run 3 because the carbon mat was cut to be much closer to the gas phase area.

5.4.4 Conclusions and recommendations

A bench-scale test cell for electrochemical carbon capture in a flowing electrolyte was designed and built for demonstration. An electrolyte mixture of phenanthrenequinone and ferrocene was used in each experiment, and the current, voltage, and carbon capture rates were quantified. This is the first demonstration of carbon capture in a system like this, and the first demonstration of an electrochemical cell that couples quinone and ferrocene in organic media in a functional way.

The results have provided key indicators for future work in the test cell. Experiments were severely limited by the fact that it was not possible to assemble this cell in a way that avoids leaking of the fluid out of the cell and leaking in to the gas line. In this particular design, the main culprit was the inability to seal the gas channel area *and* seal the Teflon-graphite interface with the O-ring. A new design that uses the same graphite electrodes should have an o-ring diameter that is as large as possible, but still inside the bolt pattern. Then, it would be easier to ensure the polypropylene spans the channel area, and the carbon fiber mat makes good electrical connections. Teflon-treated carbon paper may also improve the system. A gasket may be a better alternative to the O-ring because it would fill the space between the Teflon part and the graphite plates. At the same time, gaskets tend to be harder to seal because the greater surface area requires a greater pressure to compress and seal the system.

The flow channel itself should be designed to eliminate "dead spots" and fluid mixing. The liquid inlet and outlet channels should be re-designed to better approximate laminar flow between the electrodes. It is hypothesized that the current efficiency was reduced by the fact that the fluid must be forced from a channel height of 1 cm through two pipe diameters that are smaller than 1 cm. Most likely, the fluid mixes as it nears the end of the channel, and some of the ferrocenium oxidizes the dianion and desorbs the CO_2 before the fluid exits the system. In addition, the rectangular design means there is asymmetric flow through the channel, with slower flow in some of the corners, and mixing at the outlet. This reduces the current by making for larger regions where it is mass-transfer limited at the electrode surface.

6 Experimental demonstration of CO_2 capture and release in flow-through-electrodes design

6.1 Introduction

The operational challenges faced in demonstrating carbon capture in the laminar flow with planar electrodes (Chapter 5) motivated the idea to use the quinone-ferrocene couple in a "flow battery" configuration to demonstrate electrochemical absorption and desorption.

The system was tested in two configurations. In Configuration 1, the quinone sorbent was contacted with the simulated flue gas (15% CO_2, 85% N_2) in the reservoir, and recirculated between the reservoir and the porous carbon electrode compartment. Figure 6.1 is a cartoon showing the relevant species, equipment, and compartments for a flow battery design in Configuration 1.

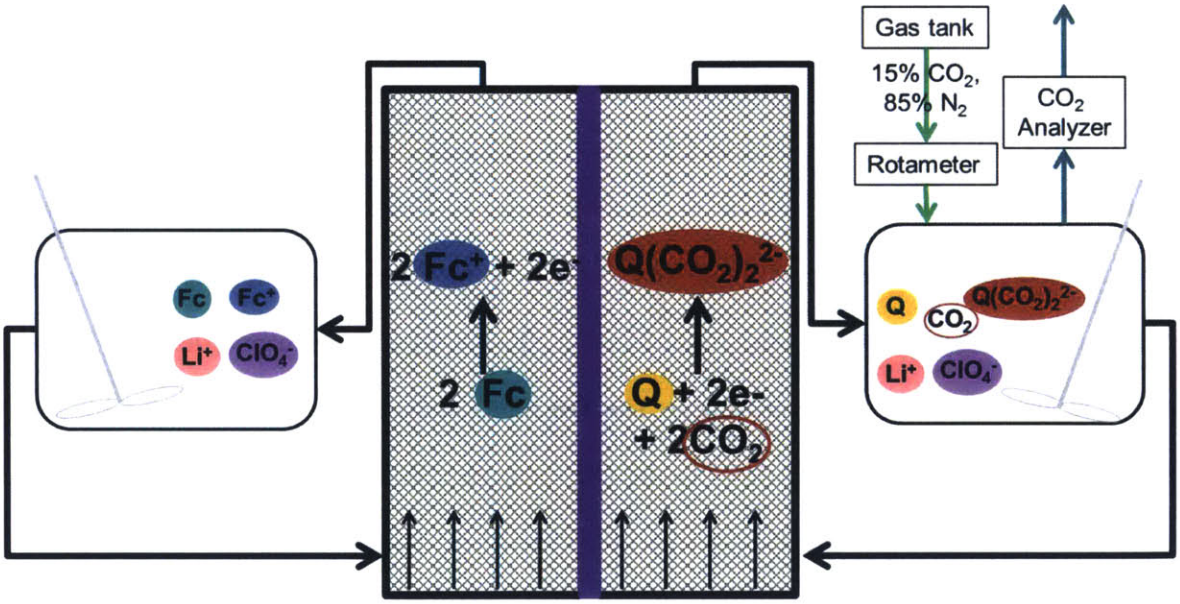

Figure 6.1 Flow through electrodes, Configuration 1, Reduction/absorption step.

In Configuration 2, the simulated flue gas enters the system at a branch at the entrance to the electrode compartment, so that it is essentially bubbled through the porous electrode, while the electrolyte flows through the same porous electrode. Figure 6.2 is a cartoon showing the relevant species, equipment, and compartments for Configuration 2.

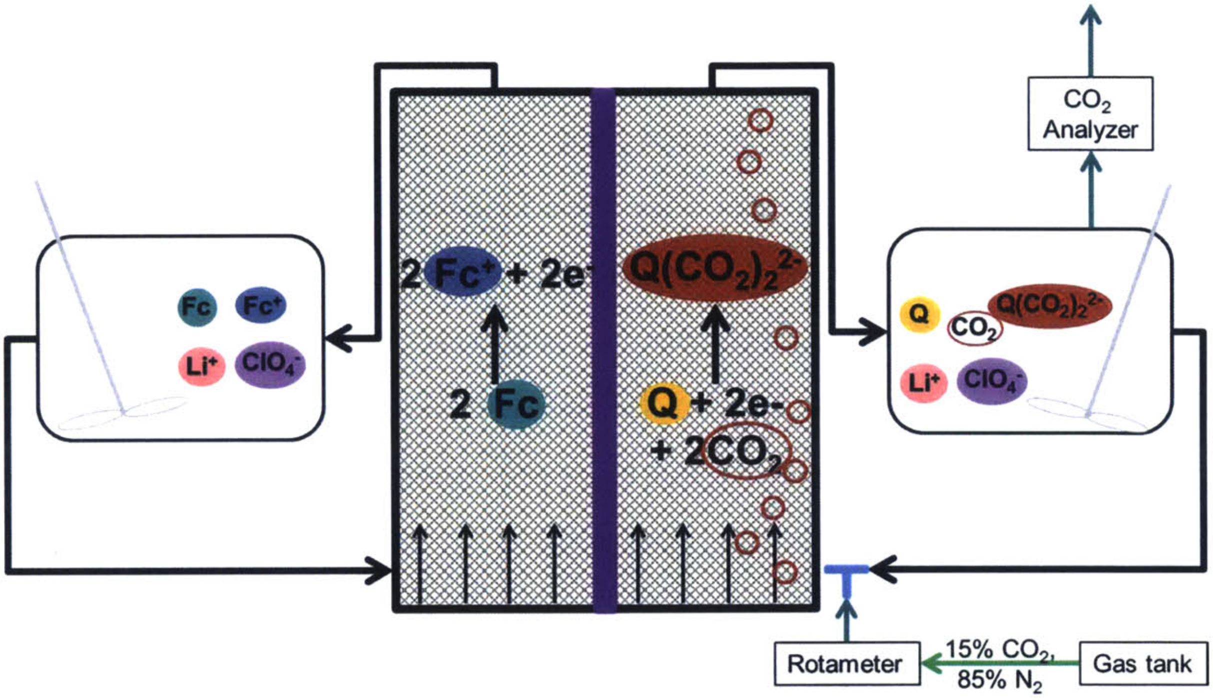

Figure 6.2 Flow through electrodes, Configuration 2, Reduction/absorption step.

In both configurations, a solution of 50 mM ferrocene is recirculated in the other electrode compartment, and the electrodes are separated by a porous polypropylene membrane. The Tee fitting at the lower right corner of the flow cell allows for one stream (fluid only) or two streams (fluid and gas at the same time) to enter the electrode compartment. The Tee fitting at the center neck of the 3-neck flask is where the gas exits the system (and flows to the CO_2 analyzer). When the second tube of the Tee is connected to the gas stream then the flue gas enters the system here. Each liquid stream has its own pump.

6.2 Materials and methods

The solvent for all experiments was dimethyl sulfoxide, purchased from Sigma-Aldrich (99.9% pure, anhydrous), and extracted from the container under Argon via a needle through the rubber septum. The following experimental materials were purchased and used directly from their containers: ferrocene (Sigma-Aldrich, 98%), 9,10-phenanthrenequinone (Sigma-Aldrich, >99%), and lithium perchlorate (Sigma-Aldrich).

Volumetric flasks and 3-neck flasks were cleaned with a combination of acetone and isopropyl alcohol and dried in an oven set at 100°C for at least 15 minutes. Every experiment involved two electrolyte mixture in dimethyl sulfoxide (DMSO) solvent: one was 50 mM PQ and 100 mM $LiClO_4$, and the other was 50 mM Fc, 100 mM $LiClO_4$. The mixtures were prepared in the volumetric flasks. 100-200 mL of each mixture was placed in its own clean and dry 3-neck flask with a clean and dry stir bar, and purged with a gas stream whose composition was 15% CO_2, 85% N_2 .

The experimental apparatus was originally designed and built by Stern [50], and Figure 6.3 contains a picture of the apparatus, partially disassembled. The apparatus consists of two white plastic parts (made of Delrin), that have a 1.5 in^3 compartment (1" x 3" x 0.5"). In each compartment is a flow-through electrode made of glassy carbon "foam". Through the top of each plastic chamber, a ¼" graphite rod passes through the wall, providing an electrical contact to an external power source. The electrical connection is reinforced with carbon "felt", a soft, fibrous form of carbon that is malleable and easily shaped. On the "back" side of each Delrin chamber (not shown), two stainless steel fittings are threaded in to the plastic part. The stainless steel fittings have threading on one side, and a Luerlock-type fitting on the other side. The threaded side turns in to the Delrin chamber and ensures a tight seal, and the Luerlock fitting makes for easy connection to the inlet and outlet tube fittings.

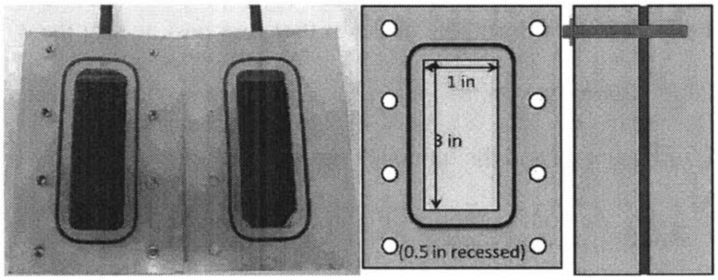

Figure 6.3 (left) Picture of the two chambers containing flow-through electrodes, shown side-by-side. (right) A schematic of what the chambers look like when the system is closed.

Stern's original device was not meant to withstand aggressive solvents, like DMSO, and it could not remain sealed if the contents were under significant pressure. Therefore, the electrodes and the Delrin compartments were modified to better suit this experimental set up. Originally, there was a ¼" diameter hole at the top of each chamber. After pushing a graphite rod through the hole and making sure it was in touch with the carbon foam, the designer used hot glue around the top of the rod to "seal" the hole.

Obviously, this seal did not survive contact with DMSO. A better design for sealing the system is to use compression fittings that would be threaded on one side, and compression fittings on the other side. For this work, the plastic compartments from the original device were drilled and tapped so that they could accommodate the threaded fitting. Using appropriate compression fittings, it was possible to seal the connection to the plastic compartment and the connection to the graphite rod. This connection provided a reliable seal even when working with DMSO and with some added pressure.

Every part of the flow-through apparatus was cleaned and dried before and after each experiment. For each experiment, two layers of Celgard 3501 membrane were used as a separator between the two flow-through chambers so that the liquids would not mix. The bolts that span the entire device were placed and finger tightened in a diagonal and then circular pattern.

For each experiment, the two 3-neck flasks acted as reservoirs for their respective fluids. Both flasks were stirred, and both flasks were fitted with Teflon stoppers that were custom-built to be threaded for ¼-NPT stainless steel compression fittings. The compression fittings are required to seal the connection between the Teflon stopper and the Teflon tubing passing through the stainless steel fittings. Teflon gaskets were placed between the Teflon stopper and the necks of the glass flask to seal the connection. Figure 6.4 is a picture of the actual laboratory set up. Mixture of red and green food dye were used to highlight the paths of the ferrocene ("red") stream and the quinone ("green") stream.

To be able to test the two configurations (Figure 6.1 and Figure 6.2), the inlet connection on the quinone chamber was modified with a "Tee" fitting (shown in Figure 6.4). The Tee allows for one or two streams to flow in to the electrode chamber at that point. Therefore, it is possible to have the flue gas enter at that branch on the inlet side to an electrode chamber (lower right) or not. Similarly, the Tee fitting at the center neck of the 3-neck flask (right side of Figure 6.4, green dye) allows the option for the flue gas to enter there, or not.

Figure 6.4 Experimental set up for CO_2 capture using flow-through electrodes. Liquid paths are highlighted using solutions of red and green food dye.

The CO_2 Analyzer was purchased from co2meter.com. A rotary vane pump was used to pump the quinone electrolyte, and it was purchased from Fluid Metering Inc, and outfitted with special Teflon fittings that are safe to use with organic solvent. A peristaltic pump was used to pump the ferrocene electrolyte. All tubing was either 1/8" Teflon tubing or chemically-resistant Masterflex tubing, and all fitting were either polypropylene or stainless steel.

For the experiment performed in Configuration 1, the gas mixture of 15% CO_2, 85% N_2 was pumped in and out of the 3-neck flask/reservoir at a rate of 14 to 15 mL/min. For the experiment performed in Configuration 2, the gas mixture was pumped in at the inlet fitting to the cathode chamber, and the outlet gas exited the system from the 3-neck flask.

In each experiment, a mixture of 50 mM Fc and 100 mM $LiClO_4$ in DMSO was pumped at a rate of about 10 mL/min on the left side. The mixture was saturated with a gas mixture of 15% CO_2 and 85% N_2 before and during the experiment. A mixture of 50 mM PQ and 100 mM $LiClO_4$ in DMSO was pumped at a rate of 11.2 mL/min on the right side. During each experiment, the current, voltage, and percent CO_2 in the outlet gas were recorded, along with the gas and liquid flow rates. After establishing a baseline for the percentage CO_2 readout, a potential of +1 V was applied, and the current and percent CO_2 were observed, while the gas flow rate was maintained constant. After re-establishing the baseline, the same procedure was used, but a potential of -1V was applied.

6.3 Results

There were two sets of experiments performed with the flow-through electrode apparatus. The first was set up in Configuration 1 – with the gas stream entering and exiting the system at the glass reservoir. The current and percent CO_2 in the outlet are plotted as functions of the experimental duration in Figure 6.5 and Figure 6.6. Figure 6.5 shows the current for the reduction of quinone (left). The consequential drop in the percentage of CO_2 as it exits the absorber (shown on the right in Figure 6.5) proves the CO_2 is being absorbed by the reduced quinone. Figure 6.6 shows the same measurements for the oxidation step. For clarity, the absolute value of the current is presented for the oxidation step. In reality, oxidation of the quinone corresponds to a negative current.

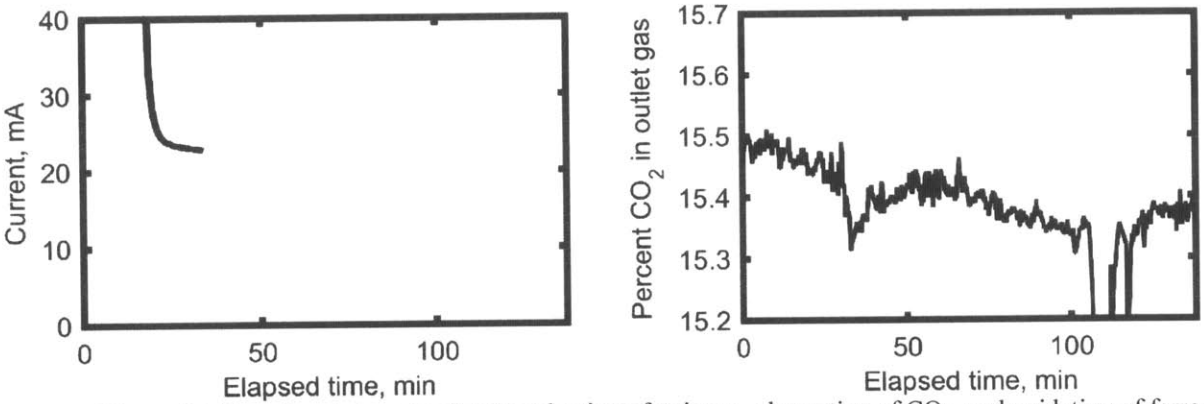

Figure 6.5 Experimental results for the reduction of quinone, absorption of CO_2, and oxidation of ferrocene. The plots show the current (left) and the percent of CO_2 in the outlet gas measured by the CO_2 analyzer (right).

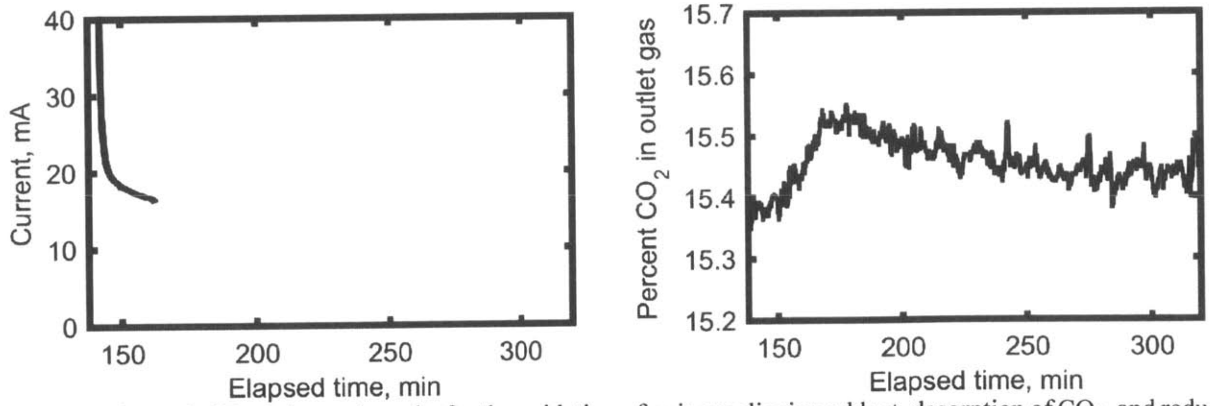

Figure 6.6 Experimental results for the oxidation of quinone dianion adduct, desorption of CO_2, and reduction of ferrocene. The plots show the current (left) and the percent of CO_2 in the outlet gas measured by the CO_2 analyzer (right).

Qualitatively, the drop in percent CO_2 in the outlet stream (Figure 6.5, right) is a clear indication of CO_2 capture linked to electrochemical reduction of quinone (Figure 6.5, left). The increase in percent CO_2 capture in the outlet stream (Figure 6.6, right) indicates a release of CO_2 that is linked to oxidation of quinone (Figure 6.6, left). The time scales on the x-axes illustrate that these experiments are much longer than the experiments in which the quinone and ferrocene move through the flow cell experiments (Section 5.4), but they show much more dramatic CO_2 capture and release, at a larger scale. Note that the data points around 2 hours (15.2%) are not experimental. Rather, they reflect an unexpected drop in pressure of the inlet gas stream. Similarly, one observes a shift in the baseline CO_2 percentage from the reduction test to the oxidation test. The baseline is somewhat sensitive to changes in the inlet gas flow rate and pressure. Therefore, the shift in baseline is most likely a result of a slight change in the inlet gas flow rate, controlled by a rotameter. The oxidation data are smoother and clearer because a better procedure for controlling the inlet gas flow rate and pressure was implemented between the two runs.

One would expect better performance from a cell in which the gas contacting occurs in the electrode chamber. A system in which the gas stream entered the system at the electrode compartment would resolve this issue. An experiment in which the 15% gas stream entered the system at the branch was set up, using the same liquid concentrations and flow rates. The set up is describe in Figure 6.2. The gas flow rate was set and stabilized at 11 mL/min before the liquid pumps were turned on. Once the liquid pumps were turned on, it was impossible to control the pressure and flow rate of the inlet gas, because the rotameter is very sensitive to downstream pressure. Also, the liquid lines in the system are somewhat prone to clogging, and this issue is exacerbated by the disruption of flow by the gas bubbles. Moreover, the liquid outlet from the electrode chamber is not at the top of the chamber, so there tends to be a buildup of a gas bubble that periodically purges through the liquid outlet. This behavior drives a huge variability in the outlet flow rate of gas and liquid, which leads to variability in the inlet flow rates of gas and liquid. Sometimes the liquid would drain in to the gas line, and then the pressure would change and the gas line would push it back in to the chamber. As a result, it was not possible to draw quantitative conclusions from this experiment. It may be possible to reconfigure the system to fix some of these issues.

6.4 Conclusions

A design for electrochemical carbon capture in a flow-through electrode system, and its experimental results, are presented in this chapter. The results link the electrochemical cycling of the quinone-ferrocene couple to absorption and desorption of carbon dioxide. These results, combined with those presented in Chapter 4, demonstrate the first application of quionone and ferrocene as an electrolyte for electrochemically-mediated carbon capture. The inherent flaws of a system in which the carbon absorption/desorption occur at the reservoir were addressed with an attempt to have the flue gas enter the cathode chamber, but the CO_2 measurements were not sufficient to demonstrate viable carbon capture in that configuration. Better control of the pressure and flow rate of the gas and liquid streams as they enter and exit the cathode chamber would improve these experiments in the future.

7 Conclusions and recommendations for future work

7.1 Summary of major work and contributions

Several novel designs are proposed and analyzed for implementation of a quinone as an electrically-controlled CO_2 sorbent for separation from a flue gas. In Chapter 2, a design in which the quinone is a vehicle for facilitated transport across a supported liquid membrane is introduced. An analytical solution for the current-potential equation is derived and used to evaluate the performance of this system in terms of energy and flux capabilities. Calculations relating the energy cost to the CO_2 flux elucidated operating regimes that were most likely to be optimal, and those parameters that would have both relatively significant (membrane thickness, quinone permeability, gas permeability) and insignificant (electrolyte conductivity) effects on cell performance. The issue of solvent loss in a supported liquid membrane design is highlighted, and this motivates exploration of alternative designs.

Motivated by mass transfer limitations and solvent loss, a design for a novel system of continuous carbon capture using a quinone in a flowing electrolyte is explored. In this design, the quinone-dianion reaction occurs symmetrically at two electrodes, one porous and one solid. During operation, carbon dioxide is absorbed at the porous cathode and desorbed at the solid anode. When the flux is high enough, there is a region near the anode where the electrolyte is supersaturated in carbon dioxide. Therefore, the complete system has two flash tanks at different pressures to desorb and collect the carbon dioxide. A numerical simulation is proposed and created to calculate the concentrations and potential in the flowing electrolyte. The electric energy demand and rate of CO_2 capture is calculated from the simulation results, and the additional energy demands of the two pumps are included in the calculation of the work of capture. The design analysis reveals the impact of the position of the stream break and the efficiency of the vacuum pump, and other factors. Results show clearly that there is a cell potential that optimizes the energy cost per mole carbon dioxide. Within the range of 0.1 to 0.3 bar, increasing the electrolyte saturation actually decreases the overall energy requirement because it reduces the pumping demand more than it reduces current efficiency.

Chapter 4 is the first presentation of a novel coupling of the reversible, electrochemical reactions of quinone to ferrocene for applications in carbon capture. Experimental results with two graphite rods as electrodes in various mixtures demonstrate the electrochemical activity of such as system, and its reversibility. These experiments demonstrate the reactive coupling of the Faradaic reactions of quinone and ferrocene at graphite surfaces, and the ability to cycle these reactions.

To demonstrate the concepts presented in Chapters 3 and 4, a bench-scale test cell for electrochemical carbon capture in a flowing electrolyte is designed and built. A mixture of ferrocene and ferrocenium is used as a proxy for the quinone-dianion system, and the steady-state current-potential curves for that electrolyte in flow are shown. Using a mixture of phenanthrenequinone and ferrocene, the current, voltage, and carbon capture rates of the system are measured. This is the first demonstration of carbon capture in a system like this, and the first demonstration of an electrochemical cell that couples quinone and ferrocene in organic media for this application.

Experimental issues prevented demonstration of CO_2 desorption using the laminar flow electrochemical cell. Instead, electrochemical cycling of CO_2 absorption-desorption via quinone is demonstrated in a flow-through electrode design. The results link the electrochemical cycling of the quinone-ferrocene couple to absorption and desorption of carbon dioxide. This work is presented in Chapter 6.

Together, these results serve as an evaluation of two designs and two chemistries for electrochemical carbon capture. A flowing electrolyte is advantageous because there is enhanced mass transfer across the boundary layer (as compared to a stagnant thin film) at the same time that the laminar flow profile prevents reactant crossover. Coupling the redox-switchable sorbent, the quinone, to the fast, reversible electrochemical interconversion of ferrocene and ferrocenium is a novel and practical chemistry for carbon capture in these designs.

7.2 Directions for future research

All of the designs presented here would benefit from development of the electrolyte and the sorbent chemistry. In all cases, the rate of carbon capture is a strong function of current, and the current is a strong function of the quinone concentration. By inspection, the optimal concentration should be the highest possible quinone concentration that does not break the solubility limit at a given temperature. However, it is important to account for ferrocene and the supporting electrolyte. If the ohmic losses increase dramatically as the relative amount of supporting electrolyte goes down, it may counteract the increase in performance from increased quinone solubility.

Future work should also investigate the performance and properties of the membranes at elevated temperature. Increasing the temperature will have several competing effects on the cell performance, and a design analysis can tease out the dominant behaviors to find cost-effective solutions. Increasing the operating temperature will reduce efficiency by increasing the cell voltage and the shaft work of the vacuum pump. At the same time, the permeability and conductivity of the electrolyte increases with increasing temperature. This increased permeability will produce higher currents and carbon capture rates. It will also reduce the overall viscosity, which should reduce frictional losses along the channel. Increasing temperature should also decrease the solubilities of the gaseous species. Reducing the gas permeabilities (up to a point), should enhance performance by increasing current efficiency and making it easier to supersaturate the electrolyte. Thus, temperature is an interesting parameter that can be investigated with the existing model and accounting for changes in physical parameters from increased temperature.

The specific chemistry of ferrocene and ferrocenium is somewhat challening for carbon capture because ferrocenium is known to be oxygen sensitive. However, the literature reports that sufficient alkylation of the cyclopentadienyl ring can stabilize the species. Specifically, octamethylferrocene and decamethylferrocene are reported to be stable to the presence of dissolved oxygen in acetonitrile solvent. [96]

Future work with the flow cell design from Chapter 5 should focus on improving the design to eliminate the issue of the electrolyte leaking in to the gas channels and leaking out of the cell itself. A new design that uses the same graphite electrodes should have an o-ring diameter that is as large as possible, but still inside the bolt pattern. Teflon-treated carbon paper may also improve the results. A gasket may be a better alternative to the O-ring, but gaskets tend to be harder to seal because the greater surface area requires a greater pressure to compress and seal the system. In addition, the flow channel itself should be designed to eliminate "dead spots" and fluid mixing. The liquid inlet and outlet channels should be re-designed to better approximate laminar flow between the electrodes. That may include flow distributors or other devices that improve the transition from flow in a ¼" tube to flow in a 1 cm channel.

A complete system of electrochemical carbon capture using the quinone-ferrocene couple in a flow cell might include a "chemical desorber", in which the fluid that is rich in ferrocenium (anode boundary layer) and dianion adduct (cathode boundary layer) is mixed together. In the desorption tank, the ferrocenium oxidizes the dianion adduct and the carbon dioxide is released. Alternatively, there is opportunity to use the accumulation of ferrocenium and dianion adduct at the flow cell outlet as a "battery" and desorb the CO_2 at the same time. A second laminar flow cell downstream of the absorption cell could implement galvanic operation to convert the chemical energy of the ferrocenium-dianion mixture to electric energy, and desorb CO_2 in a gas diffusion electrode. The chemical energy is converted to heat when the two fluids are simply mixed, and the mixture that results must be cooled before it can be recycled to the flow cell. A galvanic cell design would facilitate the recovery of the chemical energy through an electric circuit.

In the new design, the pressure of the second cell will determine its utility. Desorption at 1 bar CO_2 partial pressure may not be effective, depending on the physical solubility of CO_2 in the electrolyte. It might be difficult to run the electrochemical cell at sub-atmospheric pressure, because it is likely that the electrolyte would just get sucked in to the gas channels. A more feasible alternative is to desorb CO_2 at atmospheric pressure and then use a flash tank downstream to evaporate any remaining CO_2 at lower pressures, before re-pressurizing and recycling the electrolyte.

8 References

[1] NOAA National Centers for Environmental Information, "State of the Climate: Global Analysis for March 2016," usa.gov, Asheville, 2016.

[2] M. Wild, "Decadal changes in radiative fluxes at land and ocean surfaces and their relevance for global warming," *Wiley Interdisciplinary Reviews: Climate Change,* vol. 7, no. 1, pp. 91-107, 2016.

[3] C. K. A. S. W. N. T. G. D. H. J. A. A. A. E. L. P. M. N. D. D. E. M. J. B. M. S. A. M. B. R. e. a. ,. T. P. P. Sweeney, "Seasonal climatology of CO2 across North America from aircraft measurements in the NOAA/ESRL Global Greenhouse Gas Reference Network," *Journal of Geophysical Research: Atmospheres,* vol. 120, no. 10, pp. 5155-5190, 23 May 2015.

[4] R. Pielke, The Climate Fix, Philadelphia: Basic Books, Perseus Books Group, 2010.

[5] D. E. M. B. V. R. A. C. L. M. U. C. K. M. K. M. G. M. A. T. K. Archer, "Atmospheric lifetime of fossil fuel carbon dioxide," *Annual Review of Earth & Planetary Sciences,* vol. 37, no. 1, pp. 117-134, 2009.

[6] J. C. Abanades, M. Akai, H. de Coninck, S. Benson, P. Cook, K. Caldeira, H. de Coninck, P. Cook, O. Davidson, R. Doctor, J. Dooley, P. Freund, J. Gale, W. Heidug, H. Herzog, D. Keith, M. Mazzotti and B. Betz, "Summary for Policymakers: A Special Report of Working Group III of the Intergovernmental Panel on Climate Change," Montreal, 2005.

[7] Freund, "Make deep reductions in CO2 emissions from coal-fired power plant using capture and storage of CO2," *Proceedings of The Institution of Mechanical Engineers Part A - Journal of Power and Energy,* vol. 217, pp. 1-8, 2003.

[8] U. S. Department of Energy, "Report on the first Quadrennial Technology Review," 2011.

[9] U. S. Energy Information Administration, "Annual Energy Outlook 2015 with projections to 2040," Washington, DC, 2015.

[10] C. W. Jones, "CO2 Capture from Dilute Gases as a Component of Modern Global Carbon Management," *Annual Review of Chemical and Biomolecular Engineering,* vol. 2, pp. 31-51, 2011.

[11] A. Kather and G. Scheffknecht, "The oxycoal process with cryogenic oxygen supply," *Die Naturwissenschaften,* vol. 96, no. 9, pp. 993-1010, 2009.

[12] C. M. White, B. R. Strazisar, E. J. Granite, J. S. Hoffman and H. W. Pennline, "Separation and Capture of CO2 from Large Stationary Sources and Sequestration in Geological Formation - Coalbeds and Deep Saline Aquifers," *Journal of the Air and Waste Management Association,* vol. 53, no. 6, pp. 645-715, 2003.

[13] T. C. Lieuwen, R. Yetter and V. Yang, Synthesis Gas Combustion: Fundamentals and Applications, Boca Raton: CRC Press, 2010.

[14] M. Wang, A. Lawal, P. Stephenson, J. Sidders and C. Ramshaw, "Post-combustion CO2 capture with chemical absorption: A state-of-the-art review," *Chemical Engineering Research and Design,* vol. 89, no. 9, pp. 1609-1624, 2011.

[15] J. Davison, "Performance and costs of power plants with capture and storage of CO2," *Energy,* pp. 1163-1176, 2006.

[16] G. T. Rochelle, "Amine scrubbing for CO2 capture," *Science,* vol. 325, no. 5948, pp. 1652-4, 2009.

[17] P. Markewitz, W. Kuckshinrichs, W. Leitner, J. Linssen, P. Zapp, R. Bongartz, A. Schreiber and T. E. Muller, "Worldwide innovatinos in teh development of carbon capture technologies and the utilization of CO2," *Energy & Environmental Science,* pp. 7281-7305, 2012.

[18] R. R. Bottoms, "Process for separating acidic gases". USA Patent US 1783901 A, 2 December 1930.

[19] A. Hartono, E. F. da Silva and H. F. Svendsen, "Kinetics of carbon dioxide absorption in aqueous solution of diethylenetriamine (DETA)," *Chemical Engineering Science,* vol. 64, no. 14, pp. 3205-3213, 2009.

[20] D. Y. C. Leung, G. Caramanna and M. M. Maroto-Valer, "An overview of current status of carbon dioxide capture and storage technologies," *Renewable and Sustainable Energy Reviews,* vol. 39, pp. 426-443, 2014.

[21] Z. Liang, W. Rongwong, H. Liu, K. Fu, H. Gao, F. Cao, R. Zhang, T. Sema, A. Henni, K. Sumon, D. Nath, D. Gelowitz, W. Srisang, C. Saiwan, A. Benamor, M. Al-Marri, H. Shi, T. Supap, C. Chan, Q. Zhou, M. Abu-Zahra, W. Malcolm, W. Olson, R. Idem and P. Tontiwachwuthikul, "Recent progress and new developments in post-combustion carbon-capture technology with amine based solvents," *International Journal of Greenhouse Gas Control,* vol. 40, pp. 26-54, 2015.

[22] E. Chabanon, R. Bounaceur, C. Castel, S. Rode, D. Roizard and E. Favre, "Pushing the limits of intensified CO2 post-combustion capture by gas-liquid absorption through a membrane contactor," *Chemical Engineering and Processing,* vol. 91, pp. 7-22, 2015.

[23] M. C. Stern, F. Simeon, H. Herzog and T. A. Hatton, "Post-combustion carbon dioxide capture using electrochemically mediated amine regeneration," *Energy & Environmental Science,* pp. 2505-2517, 2013.

[24] M. C. Stern and T. A. Hatton, "Bench-scale demonstration of CO2 capture with electrochemically-mediated amine regeneration," *RSC Advance,* vol. 4, no. 12, pp. 5906-5914, 2014.

[25] D. Camper, J. E. Bara, D. L. Gin and R. D. Noble, "Room-Temperature Ionic Liquid-Amine Solutions: Tunable Solvents for Efficient and Reversible Capture of Co2," *Industrial & Engineering Chemistry Research,* vol. 47, no. 21, pp. 8496-8498, 2008.

[26] J. F. Brennecke and B. E. Gurkan, "Ionic Liquids for Co2 Capture and Emission Reduction," *The Journal of Physical Chemistry Letters,* vol. 1, no. 24, pp. 3459-3464, 2010.

[27] S. Choi, J. H. Drese and C. W. Jones, "Adsorbent Materials for Carbon Dioxide Capture from Large Anthropogenic Point Sources," *ChemSusChem,* vol. 2, no. 9, pp. 796-854, 2009.

[28] H. Gupta and L. Fan, "Carbonation-Calcination Cycle Using High Reactivity Calcium Oxide for Carbon Dioxide Separation from Flue Gas," *Society,* vol. 41, pp. 4035-4042, 2002.

[29] J. Winnick, H. Toghiani and P. D. Quattrone, "Carbon Dioxide Concentration for Manned Spacecraft Using a Molten Carbonate Electrochemical Cell," *AIChE Journal,* vol. 28, no. 1, pp. 103-111, 1982.

[30] J. L. Weaver, "The Molten Carbonate Carbon Dioxide Concentrator: Cathode Performance at High CO2 Utilization," *Journal of The Electrochemical Society,* vol. 130, no. 1, pp. 20-28, 1983.

[31] M. P. Kang and J. Winnick, "Concentration of carbon dioxide by a high-temperature electrochemical membrane cell," *Journal of Applied Electrochemistry,* vol. 15, no. 3, pp. 431-439, 1985.

[32] H. W. Pennline, E. J. Granite, D. R. Luebke, J. R. Kitchin, J. Landon and L. M. Weiland, "Separation of CO2 from flue gas using electrochemical cells," *Fuel,* vol. 89, pp. 1307-1314, 2010.

[33] J.-H. Wee, "Carbon dioxide emission reduction using molten carbonate fuel cell systems," *Renewable and Sustainable Energy Reviews,* vol. 32, pp. 178-191, 2014.

[34] J. Landon and J. R. Kitchin, "Electrochemical Concentration of Carbon Dioxide from an Oxygen/Carbon Dioxide Containing Gas Stream," *Journal of The Electrochemical Society,* vol. 157, no. 8, pp. B1149-B1153, 2010.

[35] J. D. Watkins, N. S. Siefert, X. Zhou, C. R. Myers, J. R. Kitchin, D. P. Hopkinson and H. B. Nulwala, "Redox-Mediated Separation of Carbon Dioxide from Flue Gas," *Energy & Fuels,* vol. 29, pp. 7508-8515, 2015.

[36] W. J. Ward and W. L. Robb, "Carbon Dioxide-Oxygen Separation: Facilitated Transport of Carbon Dioxide across a Liquid Film," *Science,* vol. 156, no. 3781, pp. 1481-1484, 1967.

[37] W. J. Ward, "Analytical and experimental studies of facilitated transport," *AIChE Journal,* vol. 16, no. 3, pp. 405-410, 1970.

[38] W. J. Ward, "Electrically Induced Carrier Transport," *Nature,* vol. 227, pp. 162-163, 1970.

[39] D. L. DuBois, A. Miedaner, W. Bell and J. C. Smart, "Chapter 4: Electrochemical Concentration of Carbon Dioxide," in *Electrochemical and Electrocatalytic Reactions of Carbon Dioxide,* Golden, Elsevier B. V., 1993, pp. 94-117.

[40] R. Newell, A. Appel, D. L. DuBois and M. R. DuBois, "Studies of Bicarbonate Binding by Dinuclear and Mononuclear Ni(II) Complexes," *Inorganic Chemistry,* vol. 44, no. 2, pp. 365-373, 2005.

[41] A. M. Appel, R. Newell, D. L. DuBois and M. R. DuBois, "Concentration of Carbon Dioxide by Electrochemically Modulated Complexation with a Binuclear Copper Complex," *Inorganic Chemistry,* vol. 44, no. 9, pp. 3046-3056, 2005.

[42] Rakowski, M. DuBois and D. L. DuBois, "Development of molecular electrocatalysts for CO2 reduction and H2 production/oxidation," *Accounts of Chemical Research,* vol. 42, no. 12, pp. 1974-1982, 2009.

[43] A. D. McNaught and A. Wilkinson, "Quinones," in *Compendium of Chemical Terminology*, International Union of Pure and Applied Chemistry, 1997, p. 1362.

[44] J. Q. Chambers, "Electrochemistry of quinones," in *Th Chemsitry of Quinonoid Compounds, Vol I,* Chichester, John Wiley & Sons, Inc., 1988.

[45] J. L. Cape, M. K. Bowman and D. M. Kramer, "Computation of the redox and protonation properties of quinones: Towards the prediction of redox cycling natural products," *Phytochemistry,* vol. 67, no. 16, pp. 1781-1788, 2006.

[46] M. B. Mizen and M. S. Wrighton, "Reductive Addition of CO2 to 9,10-Phenanthrenequinone," *Journal of the Electrochemical Society,* vol. 136, no. 4, pp. 941-946, 1989.

[47] R. Ranjan, J. Olson, P. Singh, E. D. Lorance, D. A. Buttry and I. R. Gould, "Reversible Electrochemical Trapping of Carbon Dioxide Using 4,4'-Bipyridine That Does Not Require Thermal Activation," *The Journal of Physical Chemistry Letters,* vol. 6, pp. 4943 - 4946, 2015.

[48] Y. Tomita, S. Teruya, O. Koga and Y. Hori, "Electrochemical Reduction of Carbon Dioxide at a Platinum Electrode in Acetonitrile-Water Mixture," *Journal of The Electrochemical Society,* vol. 147, no. 11, pp. 4164-4167, 2000.

[49] T. Nagaoka, N. Nishii, K. Fujii and K. Ogura, "Mechanisms of reductive addition of CO2 to quinones in acetonitrile," *Journal of Electroanalytical Chemistry,* vol. 322, pp. 383-389, 1992.

[50] M. C. Stern, "Electrochemically-Mediated Amine Regeneration for Carbon Dioxide Separations," Massachusetts Institute of Technology, Cambridge, 2014.

[51] P. Scovazzo, J. Poshusta, D. DuBois, C. Koval and R. Noble, "Electrochemical Separation and Concentration of <1% Carbon Dioxide from Nitrogen," *Journal of The Electrochemical Society,* vol. 150, no. 5, pp. D91-D98, 2003.

[52] R. Ferrigno, A. D. Stroock, T. D. Clark, M. Mayer and G. M. Whitesides, "Membraneless Vanadium Redox Fuel Cell Using Laminar Flow," *Journal of the American Chemical Society,* vol. 124, no. 44, pp. 12930-12931, 2002.

[53] E. R. Choban, L. J. Markowski, J. Stoltzfus, J. S. Moore and P. J. Kenis, "Microfluidic Fuel Cells That Lack a PEM," *Power Sources Proceedings,* vol. 40, 2002.

[54] R. S. Jayashree, L. Gancs, E. R. Choban, A. Primak, D. Natarajan, L. Markoski and P. J. A. Kenis, "Air-Breathing Laminar Flow-Based Microfluidic Fuel Cell," *Journal of The American Chemical Society,* vol. 127, no. 48, pp. 16758-16759, 2005.

[55] W. A. Braff, M. Z. Bazant and C. R. Buie, "Membrane-less hydrogen bromine flow battery," *Nature Communications,* vol. 4, 2013.

[56] W. A. Braff, C. R. Buie and M. Z. Bazant, "Numerical and Analytical Modeling of a Membraneless Hydrogen Bromine Laminar Flow Battery," *ECS Transactions,* vol. 53, no. 7, 2013.

[57] M.-A. Goulet and E. Kjeang, "Reacant recirculation in lectrochemical co-laminar flow cells," *Electrochimica Acta,* vol. 140, pp. 217-224, 2014.

[58] B. Huskinson, M. P. Marshak, C. Suh, S. Er, M. R. Gerhardt, C. J. Galvin, X. Chen, A. Aspuru-Guzik, R. G. Gordon and M. J. Aziz, "A metal-free organic-inorganic aqueous flow battery," *Nature,* vol. 505, no. 7482, pp. 195-198, 2014.

[59] S. Er, C. Suh, M. P. Marshak and A. Aspuru-Guzik, "Computational design of molecules for an all-quinone redox flow battery," *Chemical Science,* vol. 6, pp. 885-893, 2015.

[60] X. Li, "Modeling and simulation study of a metal free organic-inorganic aqueous flow battery with flow through electrodes," *Electrochmica Acta,* vol. 170, pp. 98-109, 2015.

[61] K. Lin, Q. Chen, M. R. Gerhardt, L. Tong, S. B. Kim, L. Eisenach, A. W. Valle, D. Hardee, R. G. Gordon, M. J. Aziz and M. P. Marshak, "Alkaline quinone flow battery," *Science,* vol. 349, no. 6255, pp. 1529-1532, 2015.

[62] S. A. M. Shaegh, N.-T. Nguyen and S. H. Chan, "A review on membraneless laminar flow-based fuel cells," *International Journal of Hydrogen Energy,* vol. 36, no. 9, pp. 5675-5694, 2011.

[63] G. Lagger, H. Jensen, J. Josserand and H. H. Girault, "Hydro-voltaic cells: Part I. Concentration cells," *Journal of Electroanalytical Chemistry,* vol. 545, pp. 1-6, 2003.

[64] S.-H. Cho, J. Shim, S.-H. Yun and S.-H. Moon, "Enzyme-catalyzed conversion of phenol by using immpobilized hresradish peroxidase (HRP) in a membraneless electrochemical reactor," *Applied Catalysis A: General,* vol. 331, no. 1, pp. 66-72, 2008.

[65] M. S. Hasenbank, E. Fu, J. B. Nelson, D. T. Schwartz and P. Yager, "Investigation of heterogeneous electrochemical processes using multi-stream laminar flow in a microchannel," *Lab on a Chip,* vol. 7, pp. 441-447, 2007.

[66] B. Levich, "The theory of concentration polarization," *Actia Physicochimica URSS,* vol. 17, pp. 257-307, 1942.

[67] K. T. Chu, "Asymptotic Analysis of Extreme Electrochemical Transport," Massachusetts Institute of Technology, Cambridge, 2005.

[68] W. M. Deen, Analysis of Transport Phenomena, New York: Oxford University Press, 1998.

[69] P. J. Welford, B. A. Brookes, J. D. Wadhawan, H. B. McPeak, C. E. W. Hahn and R. G. Compton, "The Electro-reduction of Carbon Dioxide in Dimethyl Sulfoxide at Gold Microdisk Electrodes: Current | Voltage Waveshape Analysis," *The Journal of Physical Chemistry B,* vol. 105, no. 22, pp. 5253-5261, 2001.

[70] M. Shokouhi, H. Farahani and M. Hosseini-Jenab, "Experimental solubility of hydrogen sulfide and carbon dioxide in dimethylformamide and dimethylsulfoxide," *Fluid Phase Equilibria,* vol. 367, pp. 29-37, 2014.

[71] A. Kordikowski, A. P. Schenk, R. M. Van Nielen and C. J. Peters, "Volume Expansions and Vapor-Liquid Equilibria of Binary Mixtures of a Variety of Polar Solvents and Certain Near-Critical Solvents," *The Journal of Supercritical Fluids,* vol. 8, pp. 205-216, 1995.

[72] M. F. H. H.-J. M. Shokouhi, "Experimental solubility of hydrogen sulfide adn carbon dioxide in dimethylformamide and dimethylsulfoxide," *Fluid Phase Equilibria,* vol. 367, pp. 29-37, 2014.

[73] "NumPy," NumPy, 2016. [Online]. Available: http://www.numpy.org/.

[74] D. Nikolic, "DAE Tools Project," DAE Tools, 2016. [Online]. Available: http://www.daetools.com/.

[75] D. P. G. F. J. Valencia, "Estimation of diffusion coefficients by using a linear correlation between the diffusion coefficient and molecular weight," *Jornal of Electroanalytical Chemistry,* pp. 121-126, 2012.

[76] A. Gennaro, A. A. Isse and E. Vianello, "Solubility and electrochemical determination of CO2 in some dipolar aprotic solvents," *Journal of Electroanalytical Chemistry and Interfacial Electrochemistry,* vol. 289, no. 1-2, pp. 203-215, 1990.

[77] O. Ciocirlan, A. Fedeles and O. Iulian, "Density and refractive indices of dimethyl sulfoxide + 1-hexanol system at temperatures from (298.15 to 323.15) K," *Revue Roumaine de Chimie,* vol. 55, no. 9, p. 579, 2010.

[78] L. Hau, "Thermodynamic model of solubility for CO2 in dimethyl sulfoxide," *Physics and Chemistry of Liquids,* vol. 47, no. 3, pp. 296-301, 2009.

[79] M. Shokouhi, H. Farahani and M. Hosseini-Jenab, "Experimental solubility of hydrogen sulfide and carbon dioxide in dimethyl formamide and dimethyl sulfoxide," *Fluid Phase Equilibria,* vol. 367, pp. 29-37, 2014.

[80] A. Kordikowski, A. P. Schenk, R. M. Van Nielen and C. J. Peters, "Volume expansions and vapor-liquid equilibria of binary mixtures of a variety of polar solvents and certain near-critical solvents," *Journal of Supercritical Fluids,* vol. 8, no. 3, pp. 205-216, 1995.

[81] J. M. V. N. H. C. A. M. M. Smith, Introduction to Chemical Engineering Thermodynamics, New York: McGraw-Hill, 2005.

[82] H. Silla, Chemical process engineering: design and economics, New York: M. Dekker, 2003.

[83] J. P. Hurvois and C. Moinet, "Reactivity of ferrocenium cations with molecular oxygen in polar organic solvents: Decomposition, redox reactions and stabilization," *Jouranl of Organometallic Chemistry,* vol. 690, pp. 1829 - 1839, 2005.

[84] M. Sato, T. Yamada and A. Nishimura, "Electrolytic Oxidation of Ferrocene in the Presence of Trace Amounts of Dissolved Oxygen," *Chemistry Letters,* no. 8, pp. 925-926, 1980.

[85] W. E. Geiger, "Organometallic Electrochemistry: Origins, Deveoopment, and Future," *Organometallics,* vol. 26, pp. 5738-5765, 2007.

[86] E. I. Rogers, D. S. Silvester, D. L. Poole, L. Aldous, C. Hardacre and R. G. Compton, "Voltammetric Characterization of the Ferrocene|Ferrocenium and Cobaltocenium|Cobaltocene Redox Couples in RTILs," *The Journal of Physical Chemistry C,* vol. 112, no. 7, pp. 2729-2735, 2008.

[87] D. E. Bublitz, G. Hoh and T. Kuwana, "Chronopotentiometric Oxidation of Ferrocene, Ruthenocene, Osmocene, and some of their derivatives," *Chemistry & Industry,* no. 20, pp. 635-636, 1959.

[88] T. Kuwana, D. E. Bublitz and G. Hoh, "Chronopotentiometric Studies on the Oxidation of Ferrocene, Ruthenocene, Osmocene, and some of their derivatives," *Journal of the American Chemical Society,* vol. 82, no. 22, pp. 5811-5817, 1960.

[89] K. M. Kadish and C. H. Su, "Relationships between Electron-Transfer Rate Constants of Bis(ligated)(octaethylporphinato)iron(III) Perchlorate and the Presence of a Spin Equilibria," *Journal of the American Chemical Society,* vol. 105, no. 2, pp. 177-180, 1983.

[90] M. Dabrowski, B. Misterkiewicz and A. Sporzynski, "Solubilities of Substituted Ferrocenes in Organic Solvents," *Journal of Chemical and Engineering Data,* vol. 46, no. 6, pp. 1627-1631, 2001.

[91] S. Toma and R. Sebesta, "Applications of Ferrocenium Salts in Organic Synthesis," *Synthesis,* vol. 47, no. 12, pp. 1683-1695, 2015.

[92] G. Gritzner and J. Kuta, "Recommendations on reporting electrode potentials in nonaqueous solvents," *Pure and Applied Chemistry,* vol. 56, no. 4, pp. 461-466, 1984.

[93] N. G. Connelly and W. E. Geiger, "Chemical Redox Agents for Organometallic Chemistry," *Chemical Reviews,* vol. 96, pp. 877-910, 1996.

[94] L. E. Barrosse-Antle, C. Hardacre and R. G. Compton, "Voltammetric Currents in Room Temperature Ionic Liquid Can Reflect Solutes Other Than the

Electroactive Species and Are Influenced by Carbon Dioxide," *Journal of Physical Chemistry B,* vol. 113, no. 9, pp. 2805-2809, 2009.

[95] F. Simeon, M. C. Stern, H. J. Herzog and T. A. Hatton, *Electrochemical and Molecular Assessment for Quinones as CO2-Binding Redox Molecules.*

[96] J. K. Bashkin and P. J. Kinlen, "Oxygen-Stable Ferrocene Reference Electrodes," *Inorganic Chemistry,* vol. 29, no. 22, pp. 4507-4509, 1990.

[97] Z. A. H. N. L. M. a. J. S. N. Cenas, "Structure-Activity Relationships in Two-Electron Reduction of Quinones," *Methods in Enzymology,* vol. 382, pp. 258-277, 2004.

[98] H. J. Reich, "Bordwell pKa Table (Acidity in DMSO)," University of Wisconsin-Madison, 2012. [Online]. Available: http://www.chem.wisc.edu/areas/reich/pkatable/index.htm. [Accessed 1 May 2016].

[99] F. G. Bordwell, R. J. McCallum and W. N. Olmstead, "Acidities and Hydrogen Bonding of Phenols in Dimethyl Sulfoxide," *Journal of Organic Chemistry,* vol. 49, pp. 1424-1427, 1984.

[100] N. Cenas, Z. Anusevicius, H. Nivinskas, L. Miseviciene and J. Sarlauskas, "Structure-Activity Relationships in Two-Electron Reduction of Quinones," *Methods in Enzymology,* vol. 382, pp. 258-277, 2004.

[101] B. M. Stoltz, "pKa Values for a Few Common Organic Acids," California Institute of Technology, [Online]. Available: http://stoltz.caltech.edu/classes/chem41a/fall2009/Files/pKa%20table.pdf. [Accessed 1 May 2016].

[102] F. G. Bordwell, "Equilibrium acidities in dimethyl sulfoxide solution," *Accounts of Chemical Research,* vol. 21, no. 12, pp. 456-463, 1988.

[103] D. H. Ripin and D. A. Evans, "Evans pKa Table," Harvard University, 4 November 2005. [Online]. Available: http://evans.rc.fas.harvard.edu/pdf/evans_pKa_table.pdf. [Accessed 1 May 2016].

[104] W. N. Olmstead, Z. Margolin and F. G. Bordwell, "Acidities of water and simple alcohols in dimethyl sulfoxide solution," *The Journal of Organic Chemistry,* vol. 45, no. 16, pp. 3295-3299, 1980.

[105] N. G. Tsierkezos, "Cyclic Voltammetric Studies of Ferrocene in Nonaqueous Solvents in the Temperature Range from 248.15 to 298.15 K," *Journal of Solution Chemistry,* pp. 289-302, 2007.

[106] W. A. B. C. R. B. M. Z. Braff, "Numerical and analytical modeling of a Membraneless Hydrogen Bromine Laminar Flow Battery," *ECS Transactions,* vol. 53, no. 7, pp. 51-62, 2013.

[107] B. Gurkan, F. Simeon and T. A. Hatton, "Quinone Reduction in Ionic Liquids for Electrochemical CO2 Separation," *ACS Sustainable Chemistry & Engineering,* vol. 3, no. 7, pp. 1394-1405, 2015.

[108] R. S. Stojanovic and A. M. Bond, "Examination of Conditions under Which the Reduction of the Cobaltocenium Cation Can Be Used as a Standard Voltammetric Reference Process in Orgnic and Aqueous Solvents," *Analytical Chemistry,* vol. 65, no. 1, pp. 56-64, 1993.

[109] J.-C. Shyu, C.-S. Wei, C.-J. Lee and C.-C. Wang, "Investigation of bubble effect in microfluidic fuel cells by a simplified microfluidic reactor," *Applied Thermal Engineering,* vol. 30, pp. 1863-1871, 2010.

[110] P. J. Welford, B. A. Brookes, J. D. Wadhawan, H. B. McPeak, C. E. W. Hahn and R. G. Compton, "The Electro-reduction of Carbon Dioxide in Dimethyl Sulfoxide at Gold Microdisk Electrodes: Current | Voltage Waveshape Analysis," *The Journal of Physical Chemistry B.*

9 Appendix: Derivation of Navier-Stokes equation for pressure-driven flow between flat plates with correct coordinates

The modeling in Chapter 3 employs the coordinate system shown below. Note that the origin is in the lower left corner of the channel itself. The lower section (from y=0 to y = -w, and x = 0 to x = L) is the region where the flue gas flows through the device and contacts the cathode. The cathode is modeled as a vanishingly thin planar interface at y=0. The middle section (from y=0 to y=h) is where the electrolyte flows between the two electrodes. The anode is modeled as a thin planar interface at y = h.

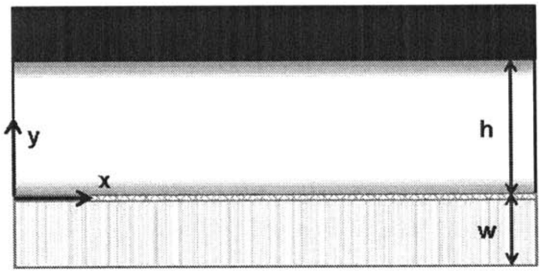

Figure 9.1 Coordinate system and dimensions for flowing electrolyte membrane.

Solution of the Navier-Stokes equation for pressure-driven flow between flat plates produces the velocity profile for the electrolyte fluid (membrane). Here, expressions for the velocity profile and average velocity are derived with the (dimensional) variables and coordinates consistent with this document.

The Navier-Stokes equation for the x-component of the velocity vector, in Cartesian coordinates, simplifies to the pressure term and the viscous term. The equation is reduced to a linear partial differential equation. It is assumed that the density is constant. With unidirectional flow, the pressure gradient is not dependent on the y-coordinate, so it is treated as a constant and the equation is simplified to an ordinary differential equation.

$$0 = \rho g_x - \frac{\partial P}{\partial x} + \mu \frac{d^2 v_x}{dy^2} \tag{102}$$

Boundary conditions – no slip conditions at both walls

$$v_x(y=0) = 0 \tag{103}$$

$$v_x(y=h) = 0 \tag{104}$$

It is convenient to non-dimensionalize the spatial coordinates of the problem (in terms of the definitions in Section 3). The dimensionless ODE is shown below.

$$0 = \rho g_x - \frac{1}{L}\frac{\partial P}{\partial \tilde{x}} + \frac{\mu}{h^2}\frac{\partial^2 v_x}{\partial \tilde{y}^2} \qquad (105)$$

$$v_x(\tilde{y}=0) = v_x(\tilde{y}=1) = 0$$

Integration of the differential equation in terms of y and application of the boundary condition yields the following velocity profile. The physical parameters that govern this profile include the viscosity (μ), the pressure gradient, and the channel height (h).

$$v_x(\tilde{y}) = \frac{h^2}{2\mu}\left(\rho g_x - \frac{1}{L}\frac{\partial P}{\partial \tilde{x}}\right)\left[\tilde{y} - \tilde{y}^2\right] \qquad (106)$$

It is convenient to non-dimensionalize the velocity to the average velocity, U. The expression for the average velocity as a function of the flow parameters is derived here.

$$U = \int_{\tilde{y}=0}^{\tilde{y}=1} v_x(\tilde{y})d\tilde{y} \qquad (107)$$

$$U = \frac{h^2}{2\mu}\left(\rho g_x - \frac{1}{L}\frac{\partial P}{\partial \tilde{x}}\right)\int_0^1(\tilde{y} - \tilde{y}^2)d\tilde{y} \qquad (108)$$

$$U = \frac{h^2}{12\mu}\left(\rho g_x - \frac{1}{L}\frac{\partial P}{\partial \tilde{x}}\right) \qquad (109)$$

For completeness, the dimensional and dimensionless velocity profiles are shown below.

$$v_x(y) = \frac{h^2}{2\mu}\left(\rho g_x - \frac{\partial P}{\partial x}\right)\left[\frac{y}{h} - \left(\frac{y}{h}\right)^2\right] \qquad (110)$$

$$v_x(y) = 6U\left[\frac{y}{h} - \left(\frac{y}{h}\right)^2\right] \qquad (111)$$

$$\tilde{v}_x(\tilde{y}) = \frac{v_x}{U} = 6\left[\tilde{y} - \tilde{y}^2\right] \qquad (112)$$

10 Appendix: Notes on graphite electrodes in quinone-ferrocene experiments

For the initial tests of the quinone-ferrocene coupled system, I used ¼" graphite rods purchased from McMaster-Carr for the experiments. Initially, I thought I could wash and reuse the graphite electrodes.

I found that the process for washing and reusing the graphite electrodes didn't work in a reliable way. When I measured the open circuit potential of the experiment before the entire process, and in between each chronoamperometry, I observed huge variations in the initial open circuit potential when the initial open circuit potential should always be effectively zero.

For a homogenous mixture and two identical electrodes, the open circuit voltage measured between those two electrodes should be approximately zero. That is, there should be no difference in the electrochemical potential between the two electrodes and the two adjacent electrolytes. To validate this and to determine if it were possible to wash and re-use graphite rods as electrodes, the open circuit potential was measured before each of the experiments in the "quinone-ferrocene" series. The results show that the experiments in which the electrodes are re-used produce open circuit voltages that are much higher than those for new electrodes. Most likely, the washing step is ineffective at removing material that is in the pores or adsorbed on to the graphite surface. Once these results were observed, future experiments were performed exclusively with new electrodes, and the experiments that involved tainted electrodes were repeated with new electrodes to ensure reliable data.

The first series of experiments proving the reduction of quinone and oxidation of ferrocene were performed in a small glass vial. They were stirred with a Teflon magnetic stir bar rotating at 500 rpm for the duration of the experiment. The electrodes were two identical graphite electrodes, ¼" in diameter, purchased from McMaster-Carr (part #9121K71). The part from McMaster-Carr is a 6 inch rod that is cut in half to produce two electrodes. One end of each electrode is "shaved" so that it is thin enough to be connected to the potentiostat leads.

Reasons for using graphite electrodes instead of glassy carbon ones:

1. Minimize mass transfer limitation

    a. The graphite electrodes have much higher surface area than the glassy carbon electrodes.
    b. A stirred electrolyte has better mixing and faster mass transfer than a quiescent electrolyte.
2. Approximate operation in the flow cell test cell
    a. The flow cell electrodes are also graphite (most likely from a different manufacturer). Both types of graphite electrodes are porous. By comparison, the glassy carbon electrodes have a polished, well-defined surface area and surface chemistry.

The disadvantages of the graphite electrodes are that the surface reactivity is not well-defined and not necessarily nor precisely consistent from one graphite rod to the next, or from one type of graphite to the next. Similarly, they are not machined to precise surface areas, so there is likely some variation among experiments.

To summarize, the graphite electrodes are advantageous because they are a better representation of the results expected from the flow cell test cell. The disadvantage is that the variability in surface chemistry and resistance adds a certain amount of uncertainty to quantitative results. To reduce the impact of this potential variability, the same kind of graphite rods were used for every experiment, and rods were not re-used. Moreover, the experiments were designed with the intent of observing differences in reactivity that are large enough that this uncertainty is acceptable. The results corroborate this assumption: the currents observed for the mixtures with both quinone and ferrocene are approximately 100 times higher than the currents observed in mixtures that are missing either or both of those components (see Section 4.3). It is highly unlikely that the surface reactivity and surface area of the graphite electrodes would vary by two orders of magnitude from one experiment to the next.

Finally, to determine if it were possible to wash and re-use graphite rods as electrodes, the open circuit potential was measured before each of the experiments in the “quinone-ferrocene” series. Figure 10.1 is a plot of the open circuit potentials for the first 10 experiments in this series. The orange bars represent the open circuit potential at the beginning of an experiment in which the graphite electrodes had been washed with DMSO, and then with acetone, and then dried with air. The blue bars represent the open circuit potential of an experiment with brand new electrodes (with no specific preparation step). The results show that the experiments in which the electrodes are re-used produce open circuit voltages that are much higher than those for new electrodes (0.1-0.2 V, compared to 0.01-0.02V).

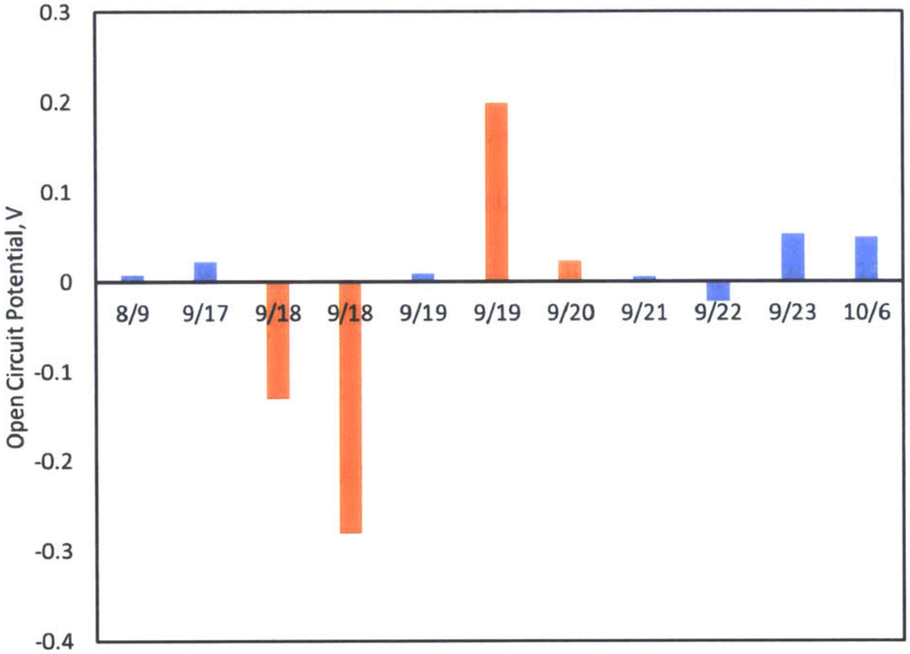

Figure 10.1 Open circuit potential for the first ten experiments in the quinone-ferrocene series. The blue bars indicate experiments with new, unused graphite rods. The orange bars indicate experiments in which used graphite rods were cleaned and re-used in a new mixture. The expeirments are labelled by the date they were performed.

Most likely, the washing step is ineffective at removing material that is in the pores or adsorbed on to the graphite surface. Once these results were observed, future experiments were performed exclusively with new electrodes, and the experiments that involved tainted electrodes were repeated with new electrodes to ensure reliable data.

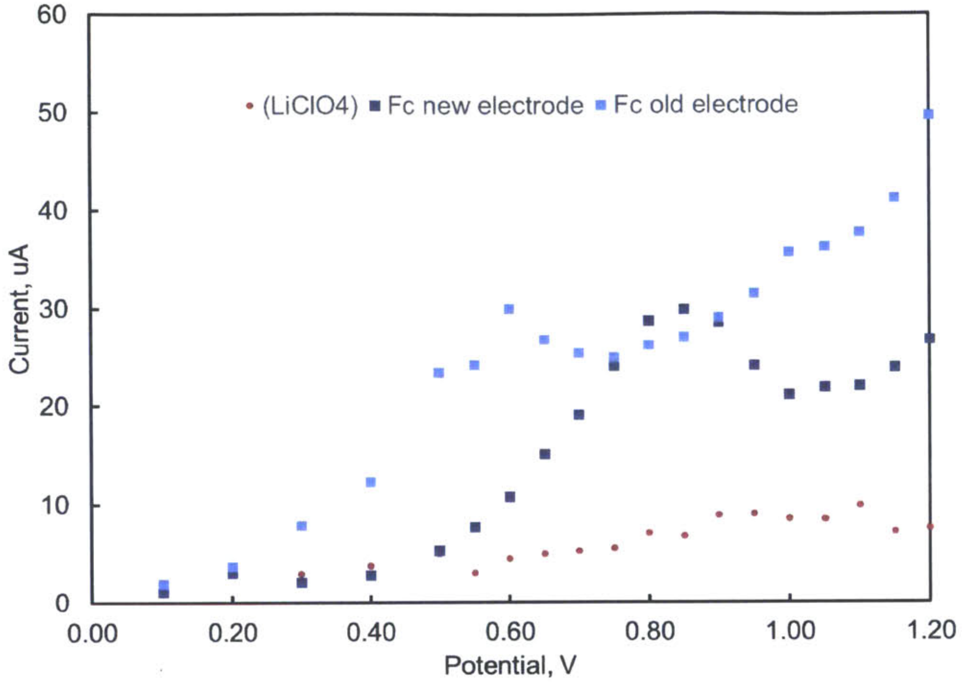

Figure 10.2 Current as a function of applied potential for a two-electrode experiment with two graphite electrodes. The two sets of blue data were gathered using identical mixtures. The red data are from a "blank" experiment on a mixture of 100 mM LiClO4 in DMSO.

Figure 10.2 contains data from three experiments. Two of the experiments involve mixtures of 50 mM ferrocene, 100 mM $LiClO_4$ in DMSO solvent. The light blue data are from an experiment involving two graphite electrodes that had been washed and dried from their previous use. The dark blue data are from an experiment involving two new, unused graphite electrodes. The red data are meant to act as a reference; they are from an experiment involving two new, unused graphite electrodes in 100 mM $LiClO_4$ in DMSO solvent (a "blank" experiment). The differences in the light and blue data highlight the issue with re-using graphite electrodes. The light blue data show a system that is significantly more reactive at low potentials as compared to the system with new electrodes. Most likely, the re-used electrodes have reactive species embedded in the pores and/or adsorbed to the graphite surface.

11 Appendix: Experimental attempts at dianion quinone synthesis

11.1 Introduction

Demonstration of CO_2 capture using the quinone-dianion couple requires the creation of an electrolyte mixture containing the neutral quinone and the dianion. The dianion may or may not be complexed with CO_2. For most of the quinones intended for electrochemical CO_2 capture, it is possible to purchase the neutral form of the quinone from Sigma-Aldrich as a powder. In some cases, it is possible to buy quinones whose ketone oxygens are reduced to the hydroxyl form. At this time, it is not possible to purchase *any* quinones in which one or both of the ketone oxygens is in the radical anion form with a cation to balance the charge. Therefore, the dianion form must be produced in the lab before the redox couple can be used for systematic carbon capture.

In this project, I attempted to create the quinone-dianion mixture using three different methods before switching to the quinone-ferrocene couple for experiments. The three methods are listed below.

1. Deprotonation of a hydroxyquinone to produce a salt in which the dianion quinone is the anion.
2. Electrochemical reduction in the "flow battery" apparatus.
3. Electrochemical reduction in a "bulk electrochemical cell", and then pumping the quinone-dianion mixture in to a different electrochemical apparatus.

The first and third methods failed to produce a useful electrolyte mixture. The second method was successful, but inflexible and difficult. The series of experiments to produce an electrolyte containing quinone and dianion are summarized in Table 4. In this appendix, the results are presented in more detail.

11.2 Deprotonation of hydroquinone

In this experiment, two attempts to deprotonate quinhydrone and produce 1,4-benzoquinone in the dianion form, balanced by the conjugate acids of the two bases. Pyridine and trimethylamine were recommended by a collaborator as common organic bases. Table 9 contains the pKa values of hydroquinone, pyridinium, trimethylamine, and *tert*-butyl alcohol in water and DMSO. The results show that the proton in pyridinium is more acidic than the proton for hydroquinone, and that means that pyridine is not basic enough to deprotonate hydroquinone. Note that the pKa value listed for hydroquinone is the pKa of one of the protons (the molecule is symmetric), the pKa of the "second" proton will be higher. However, based on the tabulated pKa values, trimethylamine should be basic enough to deprotonate hydroquinone. At the least, it should be able to remove the "first" of the two protons available in hydroquinone.

Table 9 Table of pKas of select species in water and DMSO

Species	pKa in water	pKa in DMSO
semiquinone ($QH^{\cdot}$)	4.10 [97]	*Phenol: 18.0* [98, 99]
Protonated dianion quinone (QH_2)	9.9 [100]	*(not found)*
Pyridinium	5.2 [101]	3.4 [98, 102]
Triethylammonium	10.75 [103]	9.00 [103]
tert-Butyl alcohol	19 [101], 17.0 [103]	29.4 [103], 32.2 [98, 104]

The solvent for all experiments was dimethyl sulfoxide (DMSO), purchased from Sigma-Aldrich (99.9% pure, anhydrous), and extracted from the container under Argon via a needle through the rubber septum. The following experimental materials were purchased and used directly from their containers: quinhydrone (QH, Sigma-Aldrich, 97%), pyridine (Sigma-Aldrich, anhydrous, 99.8%), triethylamine (Sigma-Aldrich, >99%). Quinhydrone is a complex that is 1:1 1,4-benzoquinone and 1,4-benzenediol (a.k.a. hydroquinone). Experiments were performed in a 50 mL round-bottom flask that was cleaned with acetone and isopropyl alcohol, and dried in a glassware oven at temperatures greater than 80°C for at least 15 minutes. A small, clean Teflon stir bar was used to stir the experiments.

For each experiment, 45 mL of the mixture was first purged with pure nitrogen for at least 30 minutes. Then, a gas mixture of 15% CO_2 and 85% nitrogen (N_2) was bubbled in to the fluid, and the amounts of CO_2 and N_2 that left the flask were quantified using a gas chromatograph. The resulting data describe the equilibrium CO2 capacity of a given mixture (Table 10) and the rate at which CO_2 is absorbed as a function of time (**Error! Reference source not found.**).

Table 10 Concentration of CO_2 in equilibrium with a gas composed of 15% CO_2, 85% N_2 at 50°C.

	DMSO	50 mM QH, DMSO	100 mM TEA, DMSO	50 mM QH, 100 mM TEA, DMSO

CO_2 Concentration (mM)	24	23	90	69
Extra CO_2 capacity (mM)	[baseline]	0	66	45
mole CO_2 per mole absorption site			0.66	0.51*

Temperature = 50°C. "QH" is quinhydrone, "TEA" is trimethylamine, "DMSO" is dimethyl sulfoxide. *The maximum capacity is calculated assuming the TEA remove one proton per hydroquinone, and the remaining 50 mM TEA absorbs 0.66 mol CO_2 per mol TEA.

The data in Table 10 show that all four mixtures absorb CO_2. The physical absorption of 45 mL of DMSO is 24 mM, and the absorption is the same for a mixture of 50 mM quinhydrone (50 mM benzoquinone, 50 mM hydroquinone). There is no additional absorption from the benzoquinone and hydroquinone, which is as expected because all binding sites are protonated. The solution of 100 mM triethylamine and the mixture of 50 mM hydroquinone, 100 mM triethylamine demonstrate significant CO_2 absorption capacity above the baseline value. A mixture of 100 mM triethylamine absorbs 90 mM CO_2 total, and the presence of triethylamine accounts for an additional 66 mM CO_2 absorbed on top of the physical absorption of the solvent. The mixture of 50 mM hydroquinone and 100 mM trimethylamine absorbs 69 mM CO_2 total, and the presence of the quinone and amine accounts for an additional 45 mM CO_2 absorbed.

The capacity of a mixture of quinhydrone and triethylamine depends on the state of each base present in the mixture. The quinhydrone in that mixture is really 50 mM benzoquinone (which is "inert" in terms of CO_2 absorption) and 50 mM hydroquinone. If both protons are abstracted from the hydroquinone hydroxyl groups, then the maximum capacity of a fluid with 50 mM quinhydrone is 100 mM CO_2 plus the physical solubility, assuming that every radical ketone on the quinone absorbs CO_2 at equilibrium. If triethylamine is only capable of removing one proton per hydroquinone, then the maximum capacity is 50 mM CO_2 plus the physical solubility. The control experiment with triethylamine alone indicates that it will absorb 66 mM CO_2 per 100 mM triethylamine. Therefore, the results seem to indicate that at best, the triethylamine removes one proton per hydroquinone, producing 50 mM of the benzoquinone radical anion for CO2 absorption. In addition, there should be 50 mM of triethylamine available for CO_2 absorption, providing an additional 33 mM CO_2 absorption capacity. Therefore, the mixture could absorb a maximum of 88 mM CO_2 on top of the physical solubility. The measured value is 45 mM CO_2 absorbed in addition to the baseline value.

The cumulative absorption data alone cannot reveal the distribution of absorbed CO_2 between the quinone and triethylamine. Figure 11.1 illustrates the instantaneous rate of CO_2 absorption over the elapsed time of the experiment for each of the four mixtures. A steeper slope of the rate curve corresponds to a faster rate of absorption. The results for 45 mL of DMSO (red) and 45 mL of 50 mM quinhydrone in DMSO (green) are nearly identical. For both those cases, the rate of absorption decays to zero within the first 40 minutes of the experiment. Those curves indicate the overall rate of physical absorption to the point of equilibrium. The black curve represents the mixture of 50 mM quinhydrone and 100 mM triethylamine and the blue curve represents the solution of 100 mM triethylamine by itself. The mixture of quinhydrone and triethylamine absorbs CO_2 more slowly than the physical absorption of the solvent and more quickly than triethylamine by itself. The fact that the absorption rates are different for the mixture and for the triethylamine control supports the claim that in the mixture, the quinone radical is absorbing some CO_2. If the triethylamine were unaffected by the quinone, then the absorption rate should be unaffected. If the two species interact but the triethylamine is the one that absorbs CO_2, then the total amount of CO_2 absorbed should be the same for the mixture as for the triethylamine control, even if the absorption rate is different. The observed reaction rates are consistent with the voltammetry data that indicate that quinone radicals (and anions) complex with CO_2 relatively quickly. They are also consistent with the literature data that indicate that absorption of CO_2 by tertiary amines is relatively slow. Together, the results indicate that the triethylamine deprotonates some of the hydroquinone, and the resulting quinone species absorbs CO_2.

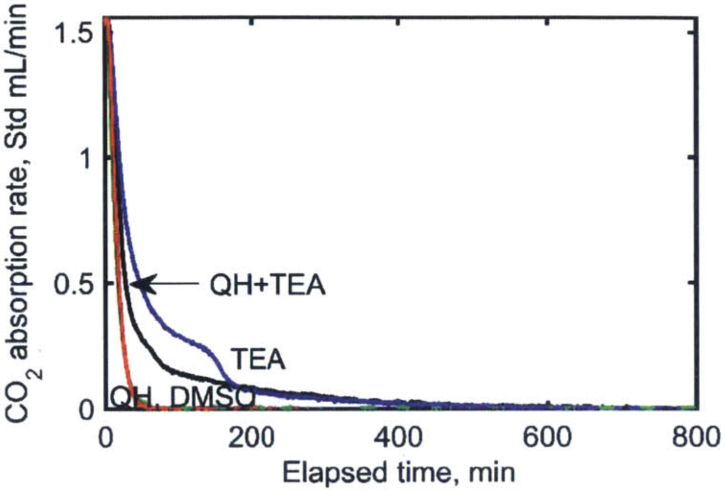

Figure 11.1Rate of CO$_2$ absorption, in standard mL/min, as a function of elapsed time for a mixture containing DMSO, quinhydrone, triethylamine, and a mixture of quinhydrone and triethylamine.

The purpose of deprotonating quinhydrone is to produce a mixture of neutral and reduced quinone for electrochemical experiments. This system only works if the protonated amine, triethylammonium, is stable under conditions of electrochemically-driven absorption and desorption. This means that the triethylammonium must stay protonated (in organic solvent) while the quinone absorbs and desorbs CO$_2$, and it must not react electrically in the neighborhood of the quinone redox potentials.

To test the feasibility of the quinhydrone-triethylamine mixture as a useable electrolyte, the mixture was tested as a thin film between two planar electrodes. Specifically, a mixture of 10 mM quinhydrone and 22 mM triethylamine in propylene carbonate was prepared using volumetric flasks and purged with CO$_2$ for at least an hour. A small amount of this mixture was placed in a "1D" cell whose walls consists of two glassy carbon electrodes, each with an area of 0.07 cm^2, placed with their surfaces in a vertical orientation, and parallel to each other. The mixture is placed between these electrodes, and the entire membrane is under 100% CO$_2$ atmosphere. If the quinhydrone-triethylamine reaction produces a stable mixture of radical anion or dianion adduct, benzoquinone, and triethylammonium cation, then it should be possible to have steady-state reduction of benzoquinone and oxidation of the radical anion or dianion adduct in a planar membrane configuration (See Chapter 2 for more details on this configuration). The results are shown in Figure 11.2.

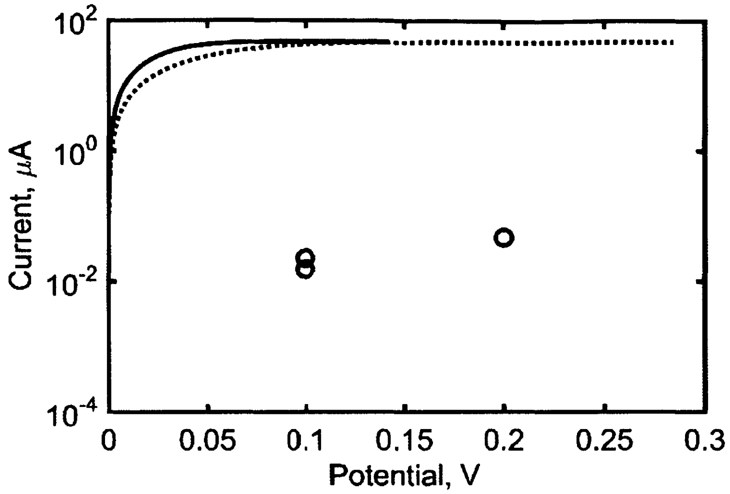

Figure 11.2 Theoretical I-V profile (lines) and experimental results (circles) for benzoquinone-radical anion couple in planar membrane.

If the deprotonation produces a stable mixture of 1,4-benzoquinone and a reduced form of 1,4-benzoquinone, then it should be possible to circulate those species in a planar membrane. A successful experimental run would produce a steady-state current carried by reduction of 1,4-benzoquinone at the cathode and oxidation of 1,4-benzoquinone radical or dianion at the anode. The two species should steadily diffuse from one electrode to the other. Figure 11.2 shows a plot of the theoretical current-potential profile for a benzoquionone-dianion couple (solid black line), a benzoquinone-radical anion couple (dashed black line) and the experimental results (circles). The experimental currents are nearly two orders of magnitude lower than they should be according to the model. Practically, experimental currents of nanoamps indicate that there is no real electrochemical activity under the conditions tested. Extremely low currents are an indication that one of the electrochemically-coupled species is unreactive or simply not present in the way it should be.

The results show that the observed currents are two orders of magnitude lower than those predicted by the model. There are several possible reasons for this result. Hydroquinone is known to be air sensitive and light sensitive. There were measures taken to protect the electrolyte from exposure to air and light, but it is still possible that the material degraded before the triethylamine was able to deprotonate the quinone. It is also possible that one of the species in the mixture reacts irreversibly under the electric potentials tested, so that the redox couple degrades quickly and cannot function as a sustainable "redox couple" for a membrane. The system can only function if quinone is oxidized and reduce at both electrodes; if one or both species is affected by the chemistry of the triethylamine, then the whole system fails.

The low current cannot be explained by the stoichiometry of the acid-base reaction between quinhyrone and triethylamine. The literature pKa values listed in Table 9 indicate that in *water*, the semiquinone radical is only slightly more acidic than pyridine, but both the semiquinone and hydroquinone forms are more acidic than triethylammonium. There are no literature values for pKas of quinones reported in DMSO. Also, it is difficult to predict a trend for changing from water to organic solvent, because the values for triethylamine and pyridine in DMSO show that their pKas are more acidic in DMSO, but *tert*-butyl alcohol has a more basic pKA in DMSO than water. Therefore, it is difficult to predict if triethylamine is basic enough to remove both protons from hydroquinone. Even if triethylamine is only basic enough to remove the first proton, the current should not be 100 times lower than that predicted by the model; it should be half the value. At the same time, the CO_2 absorption results show a difference in CO_2 absorption capacity and rate for the quinhydrone-triethylamine mixture as compared to either species alone. Regardless of the explanation, the quinhydrone-triethylamine mixture cannot function as an electrolyte for any of the CO_2 capture designs presented in this thesis if its electrochemical activity does not reveal that it is possible to couple the quinone to the radical anion or the dianion. Thus, this experimental direction was abandoned.

Further discussions with collaborators in the MIT Chemistry Department revealed that chemical generation of the radical anion or the dianion has several issues to take in to account. They suggested that there are several possible reactions that can occur in a mixture of triethylamine and quinhydrone:

- Triethylamine can sometimes act as a one-electron reducing agent, which means it might reduce some of the benzoquinone (BQ) in the quinhydrone (QH) to a radical anion or dianion rather than deprotonating the hydroquinone (HQ).
- The pKa of triethylamine is close enough to the pKa of hydroquinone that it is unlikely to produce full deprotonation of the HQ starting material, even with two-equivalents of triethylamine. If this

is the case in organic solvent, then mixing 2 equivalents of triethylamine with 1 equivalent of quinhydrone would produce a mixture in which the quinone is distributed among three states: 50% benzoquinone, 25% hydroquinone, 25% radical anion.

- Dianions are more unstable, in general.
- If oxygen is present, it may oxidize the anion quinone back to benzoquinone. This shouldn't happen in the presence of CO_2, but it is still possible.

Therefore, they suggest that the chemical combination of triethylamine and hydroquinone is not the optimal system for this application. They suggested I might use a stronger base, such as potassium *tert*-butoxide, that has a stronger likelihood of removing at least the first proton, and maybe the second proton as well. They also suggested I use a napthoquinone, because the neighboring benzene ring should help stabilize the quinone and protect it against oxidization by any oxygen present and stabilize the anion and dianion forms. Even so, they are not sure of the electrochemical behavior of a mixture of protonated quinone and potassium *tert*-butoxide. If the potassium *tert*-butoxide produces a stable quinone anion or dianion, the electrolyte is still only useful if the *tert*-butyl alcohol is electrochemically inert.

11.3 Electrochemical reduction in a flow-through electrode apparatus

Because of the inherent challenges of finding an appropriate protonated quinone and the correct base to produce the dianion, the experimental focused shifted to electrochemical methods for producing the electrolyte. One such method involved circulating two electrolyte through two porous electrodes, and oxidizing something in the sacrificial material in order to reduce the quinones in the other electrolyte. Specifically, a flow system was created to electrochemically reduce 9,10-phenanthrenequinone (PQ) in dimethylsulfoxide (DMSO).

The flow system (Figure 11.3) has two chambers that are connected through the electric circuit and a cation-selective membrane (Nafion) that allows the balance of charge while inhibiting the transport of other species. In one chamber, a solution of 94 mM PQ in DMSO is pumped through a porous electrode. There, the solution is reduced in the presence of dissolved CO_2. The product of this reduction should be the dianion adduct ($PQ(CO_2)_2^{2-}$). In the other chamber there is a solution of 100 mM tetrabutylammonium hexafluorophosphate (tBAPF6) in DMSO. This solution, also saturated in CO_2, provides electrons and counter-ions for the reduction of quinone. Without knowing explicitly what is being oxidized, the most obvious choices are the hexafluorophosphate anion (PF_6^-) or the solvent, DMSO. The expectation is that something in this solution is oxidized to provide electrons for the reduction of the quinones, and the tetrabutylammonium cations will diffuse through the Nafion membrane to balance the charge of the newly-formed quinone dianions.

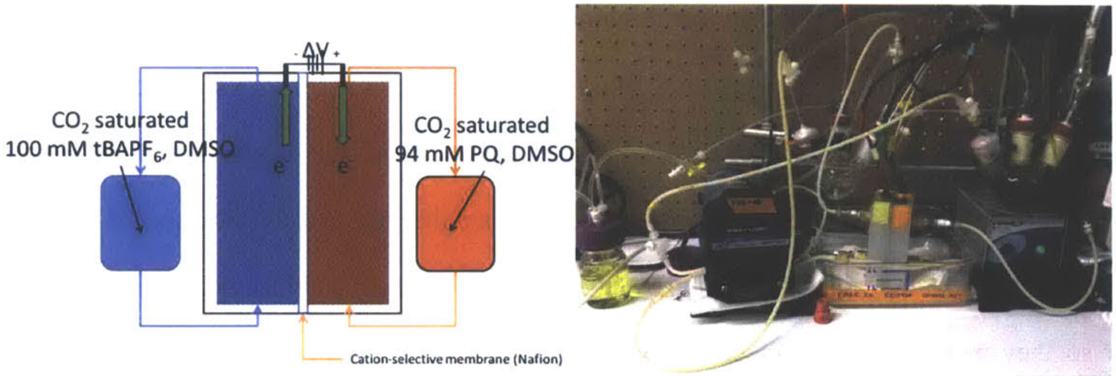

Figure 11.3 (left) Schematic of electrochemical reduction of PQ and oxidatino of sacrificial material. (right) Picture of the experimental set up.

The picture in Figure 11.3 shows the actual experimental set up. A peristaltic pump is used to circulate the electrolyte as it move through its reservoir and then its porous electrode "chamber". The 3-neck flask on the right side of the picture is the reservoir for the PQ, and it is the point at which the electrolyte is saturated with 100% CO_2. The glass vial with the purple lid on the left side of the picture is the reservoir for the sacrificial material.

In this experiment, approximately half of the PQ is reduced to the dianion adduct. The potential across the cell is set to a value between 2 and 2.5 V, and the current is observed as a function of time. Figure 11.4 shows the chronoamperometry results for the quinone reduction and the control experiments. The steady-state current for the system with 94 mM PQ in the cathode chamber is -14 mA, while the current for the two control experiments is approximately 0.7 mA at the same potential. The control experiments are performed using a mixture of 100 mM tBAPF$_6$ in DMSO (the sacrificial material) in both electrode chambers, and they produce currents that are two orders of magnitude lower than a system with 100 mM tBAPF$_6$ in DMSO in the anode chamber, and 94 mM PQ, 100 mM tBAPF6, DMSO in the cathode chamber.

Comparison of the control experiments to the PQ experiment reveals that the quinone participates in electrochemical reduction in the cathode chamber because its presence results in a 100-fold increase in current. These data are consistent with the electrochemical behavior of the quinone.

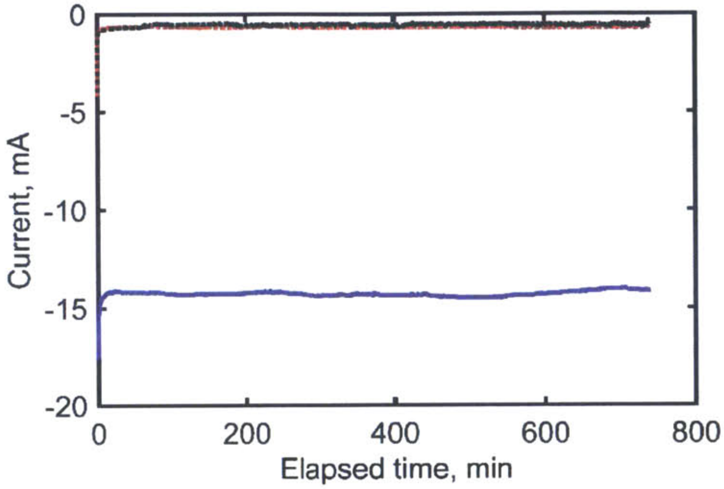

Figure 11.4 Current (mA) in the flow cell as a function of elapsed time (min) at a potential of -2.25V and room temperature. The solid blue line is data from a system with PQ in the cathode chamber. The dashed lines (red and black) are data from control experiments with 100 mM $tBAPF_6$ in both chambers.

Once the quinone mixture is produced, the flow apparatus can be reconfigured to a "figure eight" setup so that it functions as an electrochemical CO_2 capture unit. Figure 11.5 shows a schematic and a picture of the flow-through electrochemical cell and two reservoirs in a figure-eight set up. The sacrificial material is pumped out of the anode chamber and discarded, and the piping is rearranged so that the fluid flows in and out of a chamber, then in and out of a reservoir, then through the other chamber and reservoir before returning to the starting point. In this process, a solution of PQ, saturated in CO_2, enters the cathode, where it is reduced. In Figure 11.5, the cathode chamber is the right chamber of the flow-through electrochemical cell. Upon leaving the cathode, the solution enters a vessel that is purged with a stream of 100% CO_2 at room temperature and atmospheric pressure. This solution enters the anode, where the quinone is oxidized and the CO_2 desorbed. The solution leaves the anode and enters a vessel that is also purged with a stream of 100% CO_2 at atmospheric conditions. Completing the cycle, this solution returns to the cathode inlet.

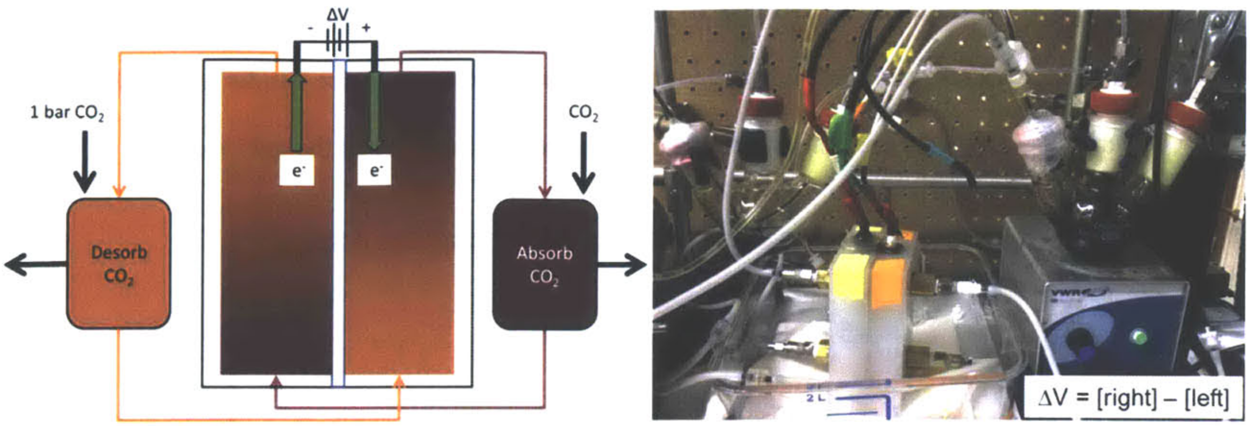

(a) (b)

Figure 11.5 (left) Schematic and (right) picture of "figure eight" set up of the flow-through electrochemical system.

Using the set up described above, a series of experiments have been performed in which the volumetric flow rate of solution and the potential across the cell are fixed, and the current through the cell is observed over time. The steady state current is recorded as a function of applied potential and flow rate. Figure 11.6 is a plot of the resulting steady-state currents measured for potentials ranging from -2 to 2 V, and flow rates ranging from 4 to 13 mL/min.

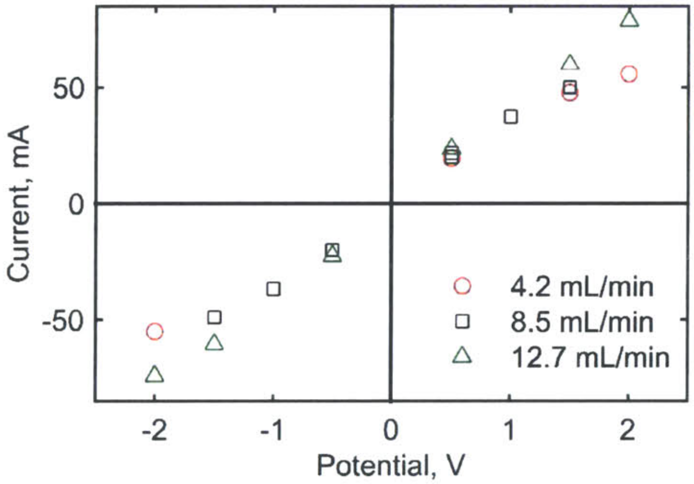

Figure 11.6 Steady-state current (mA) as a function of potential (V) and flow rate (mL/min) for the quinone-dianion couple in the figure-eight flow-through set up.

There are several qualitative and quantitative validations of the experimental data to note. First, there was no precipitate observed after the reduction process. Also, the open circuit potential was monitored for the "figure eight" flow system, and the observed potential was zero. An open circuit potential of zero validates that the solutions at each electrode are identical before and between each experiment. Third, an applied potential of positive or negative 1 V produces the same magnitude of current, and the sign of the current and potential reveal the direction of electronic flux. The "symmetry" of the results indicate that the electrolytes flowing through the two chambers are identical. All of these observations support the conclusion that the system is running properly.

The results in Figure 11.6 show trends that are consistent with expectations for the system. Higher potentials produces higher currents, regardless of direction. The difference in flow between the 4 mL/min and 8.5 mL data is greater than the increase from 8.5 mL/min to 12.7 mL/min. The fact that higher flow rates produce higher currents at the same potentials means that, to some extent, the current is limited by mass transfer to the surface of the electrode. If the flux is limited by mass transfer from the bulk electrolyte to the electrode surface, then the change in current relative to the change in flow rate should behave in a predicable way. To check this, we assume the system behaves as if it were laminar, fully-developed flow past a flat plate at limiting current. In this case, the governing equation for quinone transport in the electrolyte simplifies to a partial differential equation with a convective and diffusive term.

$$Pe\tilde{v}_x \frac{\partial \Theta}{\partial \tilde{x}} = \frac{\partial^2 \Theta}{\partial \tilde{y}^2} \tag{0.113}$$

The term "Θ" is the dimensionless quinone concentration, scaled to the bulk value, "*x*" and "*y*" are dimensionless length scales, and "*Pe*" is the Peclet number, which is the product of the average velocity and the length scale divided by the quinone diffusivity.

The current is carried by the quinone dianion, because that is the only charged, electroactive species in the system. The flux of the dianion quinone has components of convection, migration, and diffusion. For the purpose of this analysis, it is assumed that the diffusion of the dianion quinone is the dominant component of its flux, and therefore drives current through the cell. The equation below shows how the current is related to the dimensionless diffusion of quinone. It is assumed the electrode surface is at "*y=0*".

$$i_y = \frac{2FD_{Q(CO_2)_2^{2-}} C^0_{Q(CO_2)_2^{2-}}}{l} \left. \frac{\partial \Theta}{\partial \tilde{y}} \right|_{\tilde{y}=0} \tag{0.114}$$

Recall that the term "limiting current" describes the electron flux at which the concentration of quinone dianion approaches zero at the electrode surface. Under the conditions of limiting current, and no bulk flow normal to the surface, it is possible to solve the partial differential equation using the similarity technique. Then, the derivative of the similarity solution provides an expression for the derivative of concentration with respect to the positional coordinate, *y*, as a function of Peclet number and the distance from the leading edge of the electrode "plate" (*x*).

$$-\left. \frac{\partial \Theta}{\partial \tilde{y}} \right|_{\tilde{y}=0} = 0.978 \left(\frac{Pe}{\tilde{x}} \right)^{1/3} = 0.978 \left(\frac{Ul}{D_{Q(CO_2)_2^{2-}} \tilde{x}} \right)^{1/3} \tag{0.115}$$

Combining the results of the similarity solution derivative with the expression for current, the resulting expression relates the current to the average velocity, length scale, diffusivity, and distance from leading edge.

$$i_y = -\frac{1.956FD_{Q(CO_2)_2^{2-}} C^0_{Q(CO_2)_2^{2-}}}{l} \left(\frac{Ul}{D_{Q(CO_2)_2^{2-}} \tilde{x}} \right)^{1/3} \tag{0.116}$$

In the set of experimental data presented in Figure 11.6, the only parameter that changes is the volumetric flow rate. Therefore, if the system is mass-transfer limited according to mass transfer from the bulk of a fluid in laminar flow, then the current should increase in proportion to the velocity to the 1/3 power. This can be validated by calculating the slope of the natural log of the current as a function of the natural log of the velocity.

$$\ln i_y = \frac{1}{3} \ln U + \ln \frac{1.956FD_{Q(CO_2)_2^{2-}} C^0_{Q(CO_2)_2^{2-}}}{l} \left(\frac{l}{D_{Q(CO_2)_2^{2-}} \tilde{x}} \right)^{1/3} \tag{0.117}$$

The average velocity for each experiment is calculated by dividing the volumetric flow rate by the dimensions of the electrode chamber. The data for three potentials are plotted as separate lines. The results are show in Figure 11.7Figure 11.7.

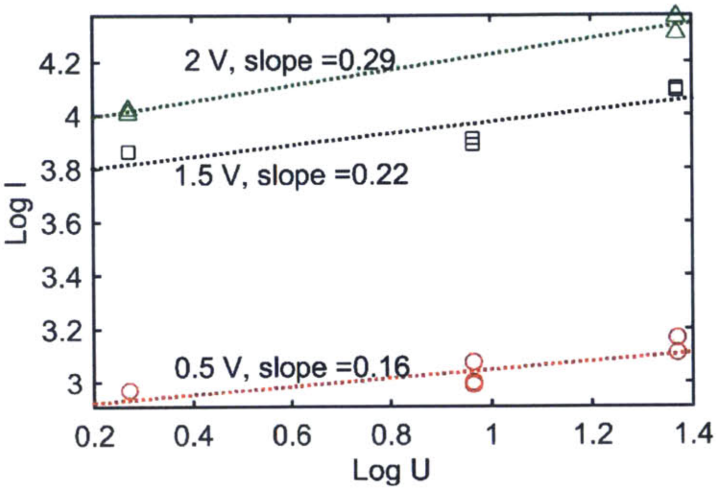

Figure 11.7 Natural log of current plotted as a function of the natural log of mean velocity for the quinone-dianion couple in the flow-through electrode system, figure-eight configuration.

If the system is mass-transfer limited under the experimental conditions, then the slopes of the lines should be approximately 1/3. The data in Figure 11.7 show that the current does not follow the "1/3" dependence on flow rate for any of the potentials tested. Instead, it is weakly dependent on flow rate. At the highest potential (2 Volts), the slope does approach the 1/3 value that is characteristic of laminar flow at limiting flux. At the lower potentials (0.5, 1, and 1.5 Volts), other resistances are comparable to mass transfer resistance. For example, the membrane that separates the two electrode chambers is made of Nafion, and it is cation-selective. It is likely that the resistance of the Nafion membrane to mass transfer of the cations to balance the charge is comparable or greater than the mass transfer resistance, especially at lower potentials. It is also possible that mixing and advection as the electrolyte flows through the porous carbon electrodes are sufficient to enhance mass transfer and mixing enough that other resistances are comparable or greater.

To date, this system is the best way to create a sorbent mixture that contains both the neutral and reduced quinone species for a desired quinone. Compared to chemical reduction (Section 11.2), it is more flexible because any quinone species can be reduced electrochemically in the system. It is not limited to the phenol and benzenediol species available for purchase. Results presented in Section 6 illustrate the possibilities for using the "flow through electrode" system for carbon capture using a quinone and reservoirs. At the same time, those results indicate the challenges to systemic carbon capture using this set up. In addition, it is very time consuming to reduce the quinone using this device. In addition, pumping the fluid out of this system and in to another experimental device is practically difficult, because it requires that both devices are designed to accommodate that fluid transfer before any experiment can happen. If there are concerns about air and/or water exposure, then controlling the environment of reduction and transfer becomes an added challenge to experimental work. Ultimately, the quinone-ferrocene proved to be a more productive experimental choice.

11.4 Electrochemical reduction in bulk electrochemical cell

Considering the challenges to chemical methods of producing quinone radical anion or dianion, electrochemical techniques are more flexible in that a wider variety of neutral quinones can be reduced electrochemically than can be purchased in their "hydroxyl" forms. At the same time, the electrochemical method is only useful if it reliably produces a mixture of reduced quinone that can be transferred from the electrochemical cell to the experimental apparatus.

Given the challenges to the "flow through" system, a bulk electrochemical cell was procured and modified for the purpose of producing a quinone-anion electrolyte that can be pumped out of the cell and in to the flow systems for carbon capture. In fact, bulk electrochemical cells are designed to electrically convert a species from one oxidation state to another and observing that conversion via current and charge measurements. That electrochemical cell is presented schematically and in a picture in Figure 11.8.

The bulk electrochemical cell consists of a glass vial that contains a glassy carbon electrode which is the working electrode. The counter electrode is usually a platinum wire encased in a glass vial whose base is a glass frit. The frit allows passage of ions to balance charge, but should not allow bulk flow of material. The reference electrode is also placed inside the system, in contact with the electrolyte. The experiment is run as a three-electrode experiment. The potential of the working electrode is set relative to the potential of the reference electrode, but current flows between the working and counter electrodes.

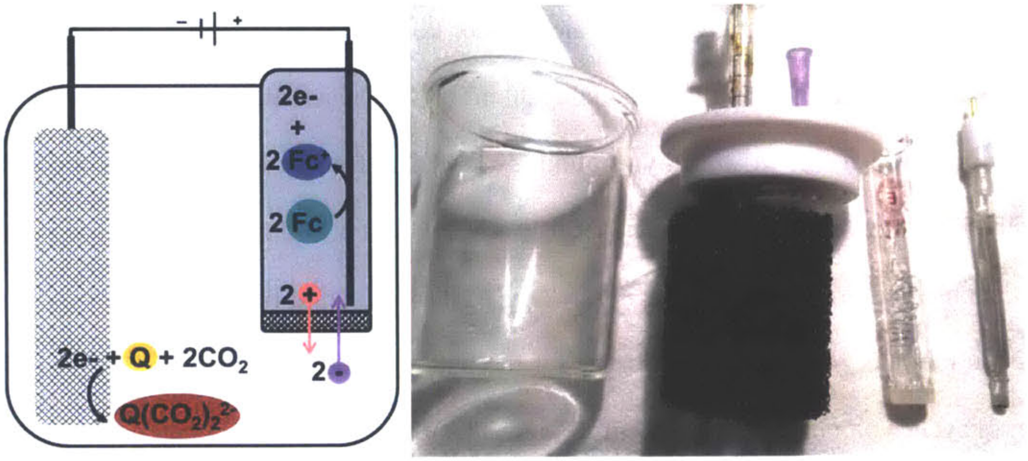

Figure 11.8 Cartoon (left) and picture (right) of bulk electrochemical cell sytem for reducing a quinone solution to produce a mixure of quinone and dianion adduct for use in experimental testing of cell designs.

For this experiment, the bulk electrochemical cell itself (the large glass cup) is filled with a solution containing 9,10-phenanthrenequinone (PQ, "Q"), dissolved CO_2, and supporting electrolyte (shown as pink "+" and purple "-"). The glass chamber that houses the counter electrode is filled with a solution containing ferrocene (Fc) and the same supporting electrolyte. The chamber itself is submerged in the electrolyte inside the radius of the glassy carbon electrode. In concept, the ferrocene in the glass chamber is oxidized at the counter electrode to provide electrons to reduce the quinone, and ions migrate through the glass frit to balance the changing charge distribution.

The picture in Figure 11.8 shows how the Teflon cap of the cell is modified to allow for gas purging and pumping the fluid out of the cell. The purple plastic part is a Luer lock fitting to a needle that is connected to Teflon tubing. This fitting is used to connect a gas line to the system. For quinone reduction, the gas line is used to ensure that the system is saturated with CO_2 for the duration of the experiment. The plastic "syringe" is fitted and sealed to the cap, and connects to stainless steel tubing that spans the entire height of the electrochemical cell. The electrolyte is pumped out of the cell through the stainless steel tubing, and then through plastic tubing connecting the electrochemical cell to a peristaltic pump and then to the experimental apparatus.

In concept, this bulk electrochemical cell can use ferrocene as a sacrificial agent that provides electrons for the production of a quinone-dianion mixture. Then, the mixture is pumped out of the cell and in to a given system for CO_2 capture (planar membrane, flow cell, etc). This procedure was tested by attempting to reduce 80 mL of a mixture containing 30 mM 9,10-phenanthrenequinone (PQ), and 100 mM lithium perchlorate ($LiCLO_4$) in dimethyl sulfoxide (DMSO). The counter electrode was filled with approximately 5 mL of 60 mM ferrocene (Fc) and 100 mM $LiCLO_4$ in DMSO. The reference electrode was a silver wire submerged in 10 mM of silver nitrate ($AgNO_3$) and 100 mM $tBAPF_6$, DMSO.

Prior to the bulk reduction, the voltages for the bulk reduction were chosen based on the results from a series of cyclic voltammetry experiments (Figure 11.9). The cyclic voltammograms show the applied potential (compared to an $Ag/AgNO_3$ reference) at which quinone is reduced. The reduction reaction occurs at an appreciable rate at potentials in the range of -0.45 to -0.55 V.

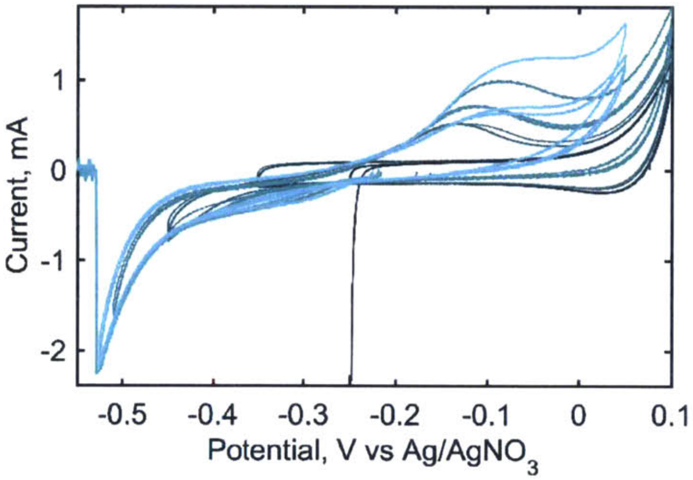

Figure 11.9 Cyclic voltammograms for a glassy carbon working electrode in a mixture of 30 mM PQ, 100 mM $LiClO_4$, DMSO with an $Ag/AgNO_3$ reference electrode.

In the cyclic voltammetry results in Figure 11.9, there are two lines that are inconsistent with the other results. At potentials of -0.25 V and -0.55 V, there is a deviation in the current profile where it appears as a "spike" and then zero current. This result occurs when the internal resistance in the cell is too high and the potentiostat cannot apply enough potential to achieve the desired reaction conditions. The potentiostat cannot apply more than 10 V total, and the actual potential applied is the total potential required to achieve the desired potential at the working electrode given the internal uncompensated resistance of the cell. The bulk electrochemical cell has a lot of uncompensated resistance due to the glass frit that separates the counter electrode from the working electrode. By comparison, the typical set up for a three-electrode is one in which the working and counter electrodes are placed in relatively close proximity (often about 1 cm distance) in an electrolyte fluid, without any physical barriers between them. In the bulk electrochemical cell, not all potentials can be achieved at all sweep rates. If the current is too high relative to the resistance of the cell, the machine terminates the experiment.

Within the operational constraints of the bulk electrochemical cell, the bulk reduction of quinone using ferrocene as a sacrificial reagent was performed over two days. The potential of the working electrode was set to potentials in the range of -0.5 to -0.8 V, and the potential was increased to more negative potentials as the reduction proceeded. At the end of the bulk reduction process, integration of the current indicated that the electrolyte mixture should contain 1 mM dianion adduct, 49 mM quinone, and 100 mM $LiClO_4$ in DMSO solvent. This mixture was pumped out of the bulk electrochemical cell and in the bench scale test cell for the electrochemical flow system (Figure 5.2, Chapters 3and 5).

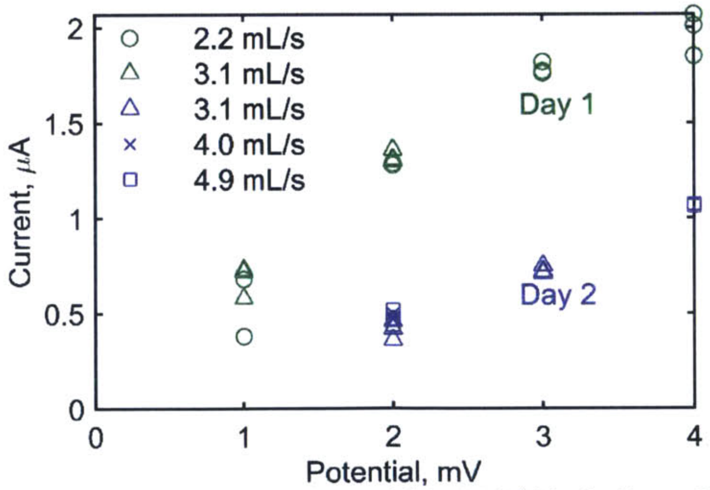

Figure 11.10 Current and potential for "Q/Q^{2-}" in the flow cell.

The results from the quinone-dianion adduct mixture in the electrochemical flow cell are presented in Figure 11.10. The potential was set to a fixed value (in the range of 1 to 4 mV), and the steady-state current was measured. The results are shown for several volumetric flow rates, and for data spanning two days. In between the experiments, the system was stored in an N_2/CO_2 environment. The results are discouraging. There is no observed difference between the data at difference flow rates. More importantly, there is no reason the measurements should change from one day to the next. Even if the pump calibration is inaccurate, the same experiment run on two different days should produce the same result. Higher flow rates should lead to higher currents, holding everything else equal. The fact that the observed currents are lower on the second day on the first indicate that there is a likelihood that something is reacting or degrading in the mixture. One hypothesis is that some ferrocenium from the counter electrode passed through the glass frit and slowly re-oxidized the dianion adduct. This hypothesis is consistent with the observation of a loss of current over time. In addition, the fact that several days of using the bulk electrochemical cell only produced a concentration of 1 mM dianion adduct is another experimental hurdle. There is a lot of "uncompensated resistance" in the electrochemical cell, which makes it impossible to run the system at higher currents (which would produce more dianion adduct faster). All in all, the idea of using the bulk electrochemical cell to make dianion adduct and then pumping the electrolyte from the bulk cell to an experimental device is not a practical solution.